

# BEAM EFFLUX MEASUREMENTS

## FINAL REPORT

G. K. KOMATSU AND J. M. SELLEN, JR.

Prepared for  
**NATIONAL AERONAUTICS AND SPACE ADMINISTRATION**  
Lewis Research Center  
Cleveland, Ohio

CONTRACT NAS 3-19537

1 JUNE 1976

(NASA-CR-135038) BEAM EFFLUX MEASUREMENTS  
FINAL REPORT (TRW, INC., REDONDO BEACH,  
CALIF.) 137 P. HC 16.00

716-25343

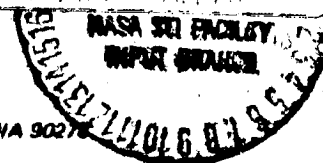
DUPLICATE

68173

**TRW**

DEFENSE AND SPACE SYSTEMS GROUP

ONE SPACE PARK • REDONDO BEACH, CALIFORNIA 90278



1. Report No. NASA-CR-135038		2. Government Accession No.		3. Recipient's Catalog No.	
4. Title and Subtitle BEAM EFFLUX MEASUREMENTS		5. Report Date June 1, 1976		6. Performing Organization Code	
		7. Author(s) G. K. Komatsu and J. M. Sellen, Jr.		8. Performing Organization Report No.	
9. Performing Organization Name and Address TRW Defense and Space Systems Group One Space Park Redondo Beach, California 90278		10. Work Unit No.		11. Contract or Grant No. NAS 3-19537	
		12. Sponsoring Agency Name and Address National Aeronautics and Space Administration Cleveland, Ohio 44135		13. Type of Report and Period Covered	
15. Supplementary Notes Project Monitor: Vincent K. Rawlin		14. Sponsoring Agency Code			
16. Abstract <p>Measurements have been made of the high energy thrust ions, (Group I), high angle/high energy ions (Group II), and high angle/low energy ions (Group IV) of a mercury electron bombardment thruster in the angular divergence range from <math>\theta = 0^\circ</math> to greater than <math>90^\circ</math>. The measurements have been made as a function of thrust ion current, propellant utilization efficiency, bombardment discharge voltage, screen and accelerator grid potential (accel-decel ratio) and neutralizer keeper potential. The shape of the Group IV (charge exchange) ion plume has remained essentially fixed within the range of variation of the engine operation parameters. The magnitude of the charge exchange ion flux scales with thrust ion current, for "good" propellant utilization conditions. For fixed thrust ion current, charge exchange ion flux increases for diminishing propellant utilization efficiency. Facility effects influence experimental accuracies within the range of propellant utilization efficiency used in the experiments. The flux of high angle/high energy Group II ions is significantly diminished by the use of minimum decel voltages on the accelerator grid.</p> <p>A computer model of charge exchange ion production and motion has been developed. The program allows computation of charge exchange ion volume production rate, total production rate, and charge exchange ion trajectories for both "genuine" and "facility effects" particles. In the computed flux deposition patterns, the Group I and Group IV ion plumes exhibit a counter motion.</p> <p>The location and requirements for on-board diagnosis of Group II and Group IV ion flux patterns have been examined and have determined appropriate probe size, configuration, and operation mode. Allowable surface placements on spacecraft to avoid thrust ion erosion have also been calculated for the various engine operation conditions used in the flux measurements.</p>					
17. Key Words (Suggested by Author(s)) Electric Propulsion Ion Propulsion 30-CM Ion Thruster Testing Beam Efflux Measurements Spacecraft/Thruster Interactive Effects			18. Distribution Statement Unclassified - Unlimited		
19. Security Classif. (of this report) Unclassified		20. Security Classif. (of this page) Unclassified		21. No. of Pages 137	22. Price*

For sale by the National Technical Information Service, Springfield, Virginia 22161

CR-135038

BEAM EFFLUX MEASUREMENTS

G. K. Komatsu and J. M. Sellen, Jr.

Prepared for

NATIONAL AERONAUTICS AND SPACE ADMINISTRATION  
Lewis Research Center  
Cleveland, Ohio 44135

CONTRACT NAS 3-19537

Contract Monitor: V. K. Rawlin

1 June 1976

**TRW**

Defense and Space Systems Group  
One Space Park  
Redondo Beach, California 90278

## TABLE OF CONTENTS

	<u>Page</u>
1.0 INTRODUCTION	1
2.0 EXPERIMENTAL FACILITIES	3
3.0 FACILITIES EFFECTS	14
3.1 General Considerations	14
3.2 Neutral Particle Species	15
3.3 Charged Particle Species	16
3.4 Facility Effects Reactions	16
3.5 Assessment of Facility Effect Current Magnitudes	18
4.0 LOW ENERGY ION MEASUREMENTS	19
4.1 General Considerations	19
4.2 Testing Chamber Ambient Pressure Effects	20
4.3 Characteristic Group IV Ion Flux Shape	25
4.4 Slow Ion Behavior as a Function of Thrust Ion Current	27
4.5 Slow Ion Behavior as a Function of Screen and Accelerator Potential	31
4.6 Slow Ion Behavior as a Function of Discharge Potential	33
4.7 Slow Ion Behavior as a Function of Neutralizer Operation Condition	43
4.8 Slow Ion Behavior as a Function of Collector Surface Material	43
4.9 Slow Ion Behavior as a Function of Propellant Utilization	45
5.0 LOW ENERGY ION FLUX MODELING	47
5.1 General Considerations	47
5.2 Calculated Group IV Ion Production and Comparison to Observed Ion Flux	48
5.2.1 Calculated Genuine Group IV Production	48
5.2.2 Calculated Facility Effect Group IV Production	52
5.2.3 Comparison of Observed Group IV Ions to Calculated Production Rates	57
5.3 Charge Exchange Ion Trajectories	59
5.3.1 Genuine Group IV Ion Trajectories	59
5.3.2 Facility Effect Charge Exchange Ion Trajectories	70
5.3.2.1 Thermal Atom/Charge Exchange Ions	70
5.3.2.2 Weakly Energetic Atom/Charge Exchange Ions	76

TABLE OF CONTENTS (continued)

	<u>Page</u>
5.3.3 Comparisons of Observed Group IV Plume Shape to Calculated Trajectories	80
5.3.3.1 Total Ion Flux as a Function of Axial Distance at Fixed $r = r_p$	80
5.3.3.2 Angular Dispersion Pattern of Group IV Ion Flux as a Function of Axial Distance at Fixed $r = r_p$	81
5.4 Limitations and Uncertainties in Group IV Ion Plume Modeling	83
5.4.1 Validity of Thrust Beam Internal Potential Model	83
5.4.2 Particle Coordinate Description Limitations	86
5.4.3 Neutral Plume Model Limitations	88
6.0 HIGH ENERGY ION FLUX MEASUREMENTS	89
6.1 General Considerations	89
6.2 Engine $J_+$ and 1-1/2" $J_+$ Measurements	90
6.3 High Angle High Energy Ion Measurements	95
6.3.1 4" $J_+$ Measurements	95
6.3.2 Swinging $J_+$ Measurements	96
6.4 Testing Chamber Ambient Pressure Effects	99
7.0 HIGH ENERGY HIGH ANGLE ION FLUX MODELING	106
7.1 General Considerations	106
7.2 Hard Ion High Angle Flux as a Function of Accel-Decel Ratio	106
7.3 Calculated Deposition Contours for Hard Ions	110
8.0 EVALUATION OF THRUSTER IN FLIGHT DIAGNOSIS FROM HIGH ANGLE ION MEASUREMENTS	117
8.1 General Considerations	117
8.2 Probe Placement	118
8.3 Probe Configuration	119
8.4 Multiple Thruster (Cluster) Effects	121
9.0 SUMMARY AND RECOMMENDATIONS	122
10.0 ACKNOWLEDGEMENTS	124
REFERENCES	125

LIST OF FIGURES

<u>Figure</u>		<u>Page</u>
1	Ion Thruster in 5' x 11' Vacuum Test Chamber with Liquid Nitrogen Cooled Upper and Lower Shrouds and Collector.	4
2	Isometric View of 30 CM Ion Thruster and Diagnostic Probe Array Used in Ion Flux Measurements.	5
3	View Along Thrust Beam (z) Axis Illustrating Radial Distance and Azimuthal Position of Diagnostic Probe Mounting Rods.	6
4	Outer Case, Grid, and Collector Configuration on Engine $J_+$ and 1-1/2" $J_+$ Probes.	7
5	Outer Case, Grids, and Collector Configuration of the Swinging $J_+$ Probe, and Probe Orientation and Motion.	8
6	4" $J_+$ Probe and Piggyback $J_+$ Probe Overall Layout and Orientation.	9
7	Outer Case, Grid, and Collector Configuration on 4" $J_+$ and Piggyback $J_+$ Probes.	10
8	Outer Case, Grid, and Collector Configuration on $J_+$ Weasel I and II Probes.	11
9	Low Energy $Hg^+$ Charge Exchange Ion Flux in the 4" $J_+$ Probe as a Function of Axial Distance, z, for Two Testing Chamber Pressure Conditions for a 0.5 Ampere Thrust Beam.	21
10	Low Energy $Hg^+$ Charge Exchange Ion Flux in the 4" $J_+$ Probe as a Function of Axial Distance z, for Two Testing Chamber Pressure Conditions for a 1.0 Ampere Thrust Beam.	22
11	Low Energy $Hg^+$ Charge Exchange Ion Flux in the Piggyback $J_+$ Probe as a Function of Axial Distance, z, for Two Testing Chamber Pressure Conditions for a 0.5 Ampere Thrust Beam. ---	23
12	Characteristic $Hg^+$ Charge Exchange Ion Signal in 4" $J_+$ Probe and Estimated Genuine Flux as a Function of Axial Distance, z.	26
13	$Hg^+$ Charge Exchange Ion Flux in the 4" $J_+$ Probe as a Function of Axial Distance, z, and Thrust Beam Current, $I_{+,t}$ , and Least Squares Fitted Linear Regression.	29

LIST OF FIGURES (continued)

<u>Figure</u>		<u>Page</u>
14	Total Ion Current, and Soft and Hard Ion Current Components in the 4" J <sub>+</sub> Probe as a Function of Axial Distance, z, for Engine Operation Data Point 16 (V <sub>s</sub> = 1.5 kV).	34
15	Total Ion Current, and Soft and Hard Ion Current Components in the 4" J <sub>+</sub> Probe as a Function of Axial Distance, z, for Engine Operation Data Point 18 (V <sub>s</sub> = 0.7 kV).	35
16	Total Ion Current, and Soft and Hard Ion Current Components in the 4" J <sub>+</sub> Probe as a Function of Axial Distance, z, for Engine Operation Data Point 2 (V <sub>g</sub> = -.5 kV).	36
17	Total Ion Current, and Soft and Hard Ion Current Components in the 4" J <sub>+</sub> Probe as a Function of Axial Distance, z, for Engine Operation Data Point 19 (V <sub>g</sub> = -.3 kV).	37
18	Total Ion Current, and Soft and Hard Ion Current Components in the 4" J <sub>+</sub> Probe as a Function of Axial Distance, z, for Engine Operation Data Point 22 (V <sub>g</sub> = -.1 kV).	38
19	Total Ion Current, and Soft and Hard Ion Current Components in the 4" J <sub>+</sub> Probe as a Function of Axial Distance, z, for Engine Operation Data Point 23 (V <sub>g</sub> = -.5 kV).	39
20	Total Ion Current, and Soft and Hard Ion Current Components in the 4" J <sub>+</sub> Probe as a Function of Axial Distance, z, for Engine Operation Data Point 24 (V <sub>g</sub> = -.7 kV).	40
21	Total Ion Current and Soft and Hard Ion Current Components in the 4" J <sub>+</sub> Probe as a Function of Axial Distance, z, for Engine Operation Data Point 28 (V <sub>ANODE</sub> = 43 V).	41
22	Total Ion Current and Soft and Hard Ion Current Components in the 4" J <sub>+</sub> Probe as a Function of Axial Distance, z, for Engine Operation Data Point 30 (V <sub>ANODE</sub> = 34 V).	42
23	Total Ion Current and Soft and Hard Ion Current Components in the 4" J <sub>+</sub> Probe as a Function of Axial Distance, z, for Two Conditions of Neutralizer Keeper Voltage.	44

LIST OF FIGURES (continued)

<u>Figure</u>		<u>Page</u>
24	Total Ion Current in the Piggyback $J_+$ Probe as a Function of Axial Distance, $z$ , for Two Conditions of Thrust Beam Collector Surface.	46
25	Computed Total $Hg^+$ Charge Exchange Current Formation as a Function of Thrust Beam Current and Propellant Utilization. Ion Beam is Parabolic Core/Exponential Wing and Neutral Emission is Uniform Over Thruster Face and $\cos \theta$ Angular Distribution.	53
26	Fraction of Charge Exchange Ion Formation in Axial Distance Interval from $z = 0$ to $z = \alpha b$ , Compared to Total $Hg^+$ Charge Exchange Ion Formation.	55
27	Computed Boundary for Which $Hg^0$ from Ion Thruster has Equal Density with $Hg^0$ in Testing Chamber, (for 280 Milliampere Equivalent $Hg^0$ Emission from Thruster, " $\cos \theta$ " Emission Uniform Over Thruster Face, Thruster Temperature of $500^\circ K$ and $1 \mu Torr$ $Hg^0$ Ambient Chamber Pressure).	56
28	Computed $Hg^+$ Charge Exchange Ion Trajectories for Engine Released Neutrals at Indicated Source Point and Charge Transfer Point.	61
29	Computed $Hg^+$ Charge Exchange Ion Trajectories for Engine Released Neutrals at Indicated Source Point and Charge Transfer Point.	62
30	Computed $Hg^+$ Charge Exchange Ion Trajectories for Engine Released Neutrals at Indicated Source Point and Charge Transfer Point.	63
31	Computed $Hg^+$ Charge Exchange Ion Trajectories for Engine Released Neutrals at Indicated Source Point and Charge Transfer Point.	64
32	Computed $Hg^+$ Charge Exchange Ion Trajectories for Engine Released Neutrals at Indicated Source Point and Charge Transfer Point.	65
33	Computed $Hg^+$ Charge Exchange Ion Trajectories for Engine Released Neutrals at Indicated Source Point and Charge Transfer Point.	66
34	Computed $Hg^+$ Charge Exchange Ion Trajectories for Engine Released Neutrals at Indicated Source Point and Charge Transfer Point.	67

LIST OF FIGURES (continued)

<u>Figure</u>		<u>Page</u>
35	Computed $\text{Hg}^+$ Charge Exchange Ion Trajectories for Engine Released Neutrals at Indicated Source Point and Charge Transfer Point.	68
36	Computed $\text{Hg}^+$ Charge Exchange Ion Trajectories for Engine Released Neutrals at Indicated Source Point and Charge Transfer Point.	69
37	Computed $\text{Hg}^+$ Charge Exchange Ion Trajectories for Engine Released Neutrals at Indicated Source Point and Charge Transfer Point.	71
38	Computed $\text{Hg}^+$ Charge Exchange Ion Trajectories for Engine Released Neutrals at Indicated Source Point and Charge Transfer Point.	72
39	Computed $\text{Hg}^+$ Charge Exchange Ion Trajectories for Engine Released Neutrals at Indicated Source Point and Charge Transfer Point.	73
40	Computed $\text{Hg}^+$ Charge Exchange Ion Trajectories for Engine Released Neutrals at Indicated Source Point and Charge Transfer Point.	74
41	Computed $\text{Hg}^+$ Charge Exchange Ion Trajectories for Engine Released Neutrals at Indicated Source Point and Charge Transfer Point.	75
42	Computed $\text{Hg}^+$ Charge Exchange Ion Trajectories for Ambient Chamber Neutrals at Indicated Charge Transfer Point and Initial Atom Direction.	77
43	Computed $\text{Hg}^+$ Charge Exchange Ion Trajectories for Ambient Chamber Neutrals at Indicated Charge Transfer Point and Initial Atom Direction.	78
44	Computed $\text{Hg}^+$ Charge Exchange Ion Trajectories for Ambient Chamber Neutrals at Indicated Charge Transfer Point and Initial Atom Direction.	79
45	Computed Ion Density Build-up in a Parabolic Core/ Exponential Wing Ion Beam from Thrust Ion Charge Transfer to Ambient $\text{Hg}^0$ as a Function of Ambient Pressure.	87
46	Engine J <sub>+</sub> Current and Floating Potential as a Function of r at $z = 4.7$ cm, with Computed Values of Density from Parabolic Core/Exponential Wing Thrust Beam Model.	91

LIST OF FIGURES (continued)

<u>Figure</u>		<u>Page</u>
47	Engine $J_+$ Current and Floating Potential as a Function of $r$ at $z = 10$ cm, with Computed Values of Density from Parabolic Core/Exponential Wing Thrust Beam Model.	92
48	Engine $J_+$ Current and Floating Potential as a Function of $r$ at $z = 15$ cm, with Computed Values of Density from Parabolic Core/Exponential Wing Thrust Beam Model.	93
49	Engine $J_+$ Current and Floating Potential as a Function of $r$ at $z = 20$ cm, with Computed Values of Density from Parabolic Core/Exponential Wing Thrust Beam Model.	94
50	Swinging $J_+$ Total Ion Current as a Function of $\theta$ for Engine Operation Data Point 4.-----	97
51	Swinging $J_+$ Total Ion Current as a Function of $\theta$ for Engine Operation Data Point 11.	98
52	Swinging $J_+$ Total Ion Current and Soft Ion Component as a Function of $\theta$ for Engine Operation Data Point 19 (Minimum Decel Condition).	100
53	Swinging $J_+$ Hard Ion Current as a Function of $\theta$ for Engine Operation Data Point 19 (Minimum Decel Condition, $V_g = -.3$ kV).	101
54	Swinging $J_+$ Hard Ion Current as a Function of $\theta$ for Engine Operation Data Point 22 (Minimum Decel Condition, $V_g = -.1$ kV).	102
55	Swinging $J_+$ Hard Ion Current as a Function of $\theta$ for Engine Operation Data Point 28 (Nominal Decel Condition, $V_g = -.5$ kV).	103
56	Energetic Ion Current in the 4" $J_+$ Probe as a Function of Axial Distance, $z$ , for Two Testing Chamber Conditions for a 1.0 Ampere Thrust Beam.	105
57	Computed Accel-Decel Ratio as a Function of Distance $x$ for Screen Grid to Accelerator Grid Spacing of $x_0$ and for Selected Values of Screen and Accelerator Grid Potentials.	109
58	Computed Hard Ion Deposition Contours for $r$ , $z$ , and $\theta$ from Swinging $J_+$ Data on Engine Operation Data Point 2 (Nominal Decel).-----	112
59	Computed Hard Ion Deposition Contours for $r$ , $z$ , and $\theta$ from Swinging $J_+$ Data on Engine Operation Data Point 19 (Minimum Decel).	113

LIST OF FIGURES (continued)

<u>Figure</u>		<u>Page</u>
60	Computed Hard Ion Deposition Contours for r, z, and $\theta$ from Swinging $J_+$ Data on Engine Operation Data Point 22 (Minimum <sup>+</sup> Decel).	114
61	Computed Hard Ion Deposition Contours for r, z, and $\theta$ from Swinging $J_+$ Data on Engine Operation Data Point 23 (Nominal <sup>+</sup> Decel).	115
62	Computed Hard Ion Deposition Contours for r, z, and $\theta$ from Swinging $J_+$ Data on Engine Operation Data Point 24 (Increased Decel).	116

LIST OF TABLES

<u>Table</u>		<u>Page</u>
1	Linear Regression of $J_+$ (Group IV) as a Function of Thrust Beam Current.	28
2	Linear Regression of Piggyback $J_+$ Signal as a Function of Thrust Beam Current.	31
3A	Engine Operation Data Points and Nominal Thruster Operational Parameters.	32
3B	Thruster Operating Parameters During Beam Efflux Measurements.	32
4A	Engine Operation Data Point with Thrust Ion Current, Propellant Utilization, and Calculated Total Genuine Charge Exchange Ion Current from Model.	58
4B	Engine Operation Data Point with Thrust Ion Current, Propellant Utilization, and Observed Soft Ion Current in 4" $J_+$ Cup at $z = 20$ cm.	58
5	Configuration Details, Size, and Placement of Ion Thruster Plume Diagnosis Probe.	120

## BEAM EFFLUX FROM A 30 CENTIMETER THRUSTER

### 1.0 INTRODUCTION

The operation of a mercury electron bombardment ion thruster results in the generation and acceleration of a beam of energetic thrust ions and accompanying neutralizing electrons moving along the thrusting axis in a generally well directed flow. The flux patterns of these thrust ions have been determined in a large number of experimental programs<sup>1-7</sup> during the development of the mercury bombardment thruster. In addition to the thrust ion currents, a series of particle effluxes from the thruster emerge with varying particle release rates, cones of divergence, and energies. The released species include both neutral and ionized mercury, and, in smaller amounts, both neutral and ionized metal atoms.

To distinguish the various mercury ion species, Staggs, et al<sup>8</sup> introduced the notation of Group I, Group II, Group III, and Group IV ions. Group I ions, described above, are energetic ions which have been accelerated by the total potential difference between the bombardment discharge and the neutralized thrust beam and have trajectories which are generally contained within a cone of divergence from the thrust axis with  $\sim 30^\circ$  half-angle. Smaller quantities of Group I ions occur at larger divergence angles. The large angular divergence regime also contains the ion species designated Group II and IV. Group II ions are the result of charge transfer processes between mercury atoms and ions in the region between the bombardment discharge and the accelerator grid and, further, in those portions of this interspace in which the potential is positive with respect to the neutralized thrust beam plasma potential. The ions formed in this charge transfer process, thus, are capable of acceleration and release into the thrust beam, although, as will be seen, their trajectories are more broadly distributed in space as a result of non-optimized ion optics and generally high decel-accel ratios. Group III ions are the result of ion-atom charge transfer reactions in the bombardment discharge-to-thrust beam interspace regions in which potential is negative with respect to the thrust beam potential. Since escape into the thrust beam is energetically forbidden, the ions are collected at the accelerator and are not observable to thrust beam diagnostic probes. The remaining

ion species, Group IV, results from charge transfer reactions between thrust ions and mercury atoms escaping from the bombardment discharge. The initial energy of these ions is, essentially, the thermal energy of the escaping neutral atom, and the resultant ion is subsequently acted on by the weak internal electric field structure in the neutralized plasma thrust beam. Because these electric fields are widely divergent, the Group IV ions emerge over a broad cone of directions.

The interest of this beam efflux measurements program is the quantity and angular divergence patterns of Groups I, II, and IV ions, for the divergence angle regime from  $0^\circ$  to greater than  $90^\circ$ . The program here continues and extends earlier measurements of these ion flux patterns with both  $20\text{ cm}^1$  and  $30\text{ cm}^{3,4}$  diameter mercury engines. The engine body utilized in this program is the same as that utilized earlier in the  $30\text{ cm}$  beam measurements<sup>3</sup>. The accelerator grids, however, have been changed to produce a more collimated thrust ion flow.

This report will describe the experimental facilities including the testing chamber, collectors, shrouds, and engine diagnostic array, and the thruster in Section 2.0. Section 3.0 will review "facility effects" which are present as a result of thruster operation in a bounded (laboratory) geometry and will include analyses of the form and possible extent of these facilities effects. Section 4.0 will present low energy (Group IV) ion flux measurements, while Section 5.0 will describe models and analyses of this low energy ion plume. Energetic ion measurements are described in Section 6.0, with a discussion of models and analyses of these ions given in Section 7.0. The possible use of low energy ion flux measurements as an in-flight diagnosis of thrust performance is discussed in Section 8.0. This assessment of Group IV ion flux density as a thruster diagnostic will also consider the effects of Group II ions whose presence at high angles creates a "noise" signal to the Group IV determination, and whose combined presence and energy creates potential problems in diagnostic probe erosion and secondary material transport and deposition.

## 2.0 EXPERIMENTAL FACILITIES

The testing chamber and diagnostic probes used in the thruster plume measurements are illustrated in Figures 1 through 8. Figure 1 shows thruster placement in the 5' x 11' chamber, and the location and size of the upper and lower shrouds and the beam collector. The shrouds and collector are electrically isolated from each other and from chamber ground. This separate electrical isolation results in a thrust beam neutralization condition in which overall electron flow from the neutralizer must equal overall ion current from the thruster and in which electron and ion currents must balance at each shroud and at the collector. The electric field pattern in the neutralized thrust beam plasma, thus, is an accurate simulation of engine operation conditions in space.

Chamber pressure in the 5' x 11' facility depends upon the level of thrust ion current and upon the level of refrigerations in the shrouds and collector. For maximum liquid nitrogen cooling of the shrouds and collectors, chamber pressure remains in the range from  $2 \times 10^{-6}$  Torr to  $5 \times 10^{-6}$  Torr. The effects of this ambient chamber pressure will be discussed more thoroughly in the sections dealing with facility effects and in the low energy ion plume measurements and modeling.

Figure 2 provides a view, in isometric, of the thruster, and the diagnostic probe array. As an additional aid in the visualization of the probe array, Figure 3 illustrates the location of the probe mounting shafts, viewed along the axis of the thruster and the test chamber. The probe mounting shaft location and the specific method of coupling of each probe to its mounting shaft will determine the available range of probe location relative to the thruster and principal directions in which the probe scans the thruster plume.

Figure 4 provides details of the Engine and 1-1/2"  $J_+$  probes. The Engine  $J_+$  is a two element Faraday cup. The outer case and grid are electrically connected and are biased, generally, at a potential negative with respect to the thrust beam plasma to prevent electrons from that plasma from moving to the collector and to suppress secondary electrons emitted from the collector by impact of the thrust ions. The rotation of the Engine  $J_+$  mounting shaft causes the Engine  $J_+$  probe to swing on

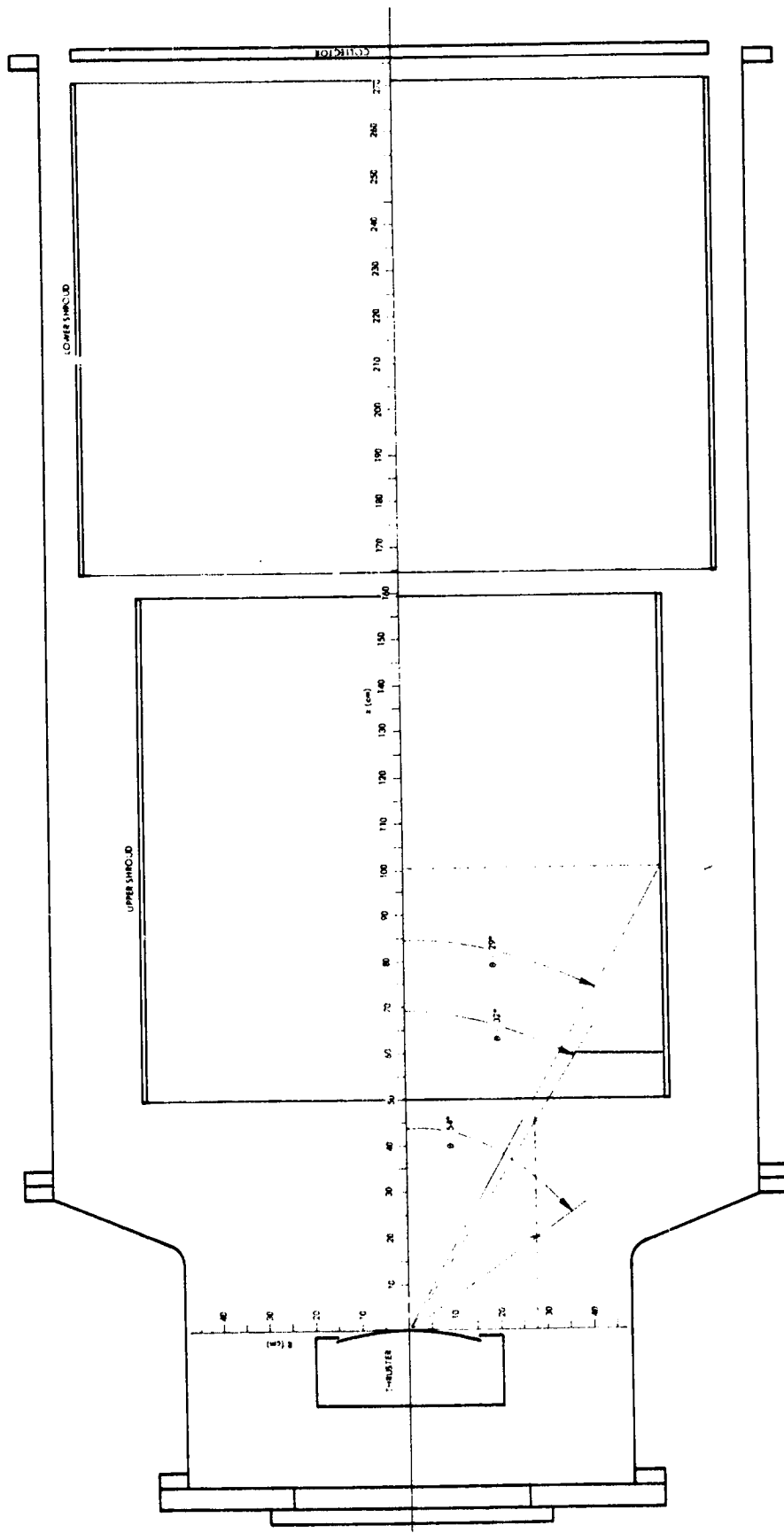


Figure 1. Ion Thruster in 5' x 11' Vacuum Test Chamber with Liquid Nitrogen Cooled Upper and Lower Shrouds and Collector.

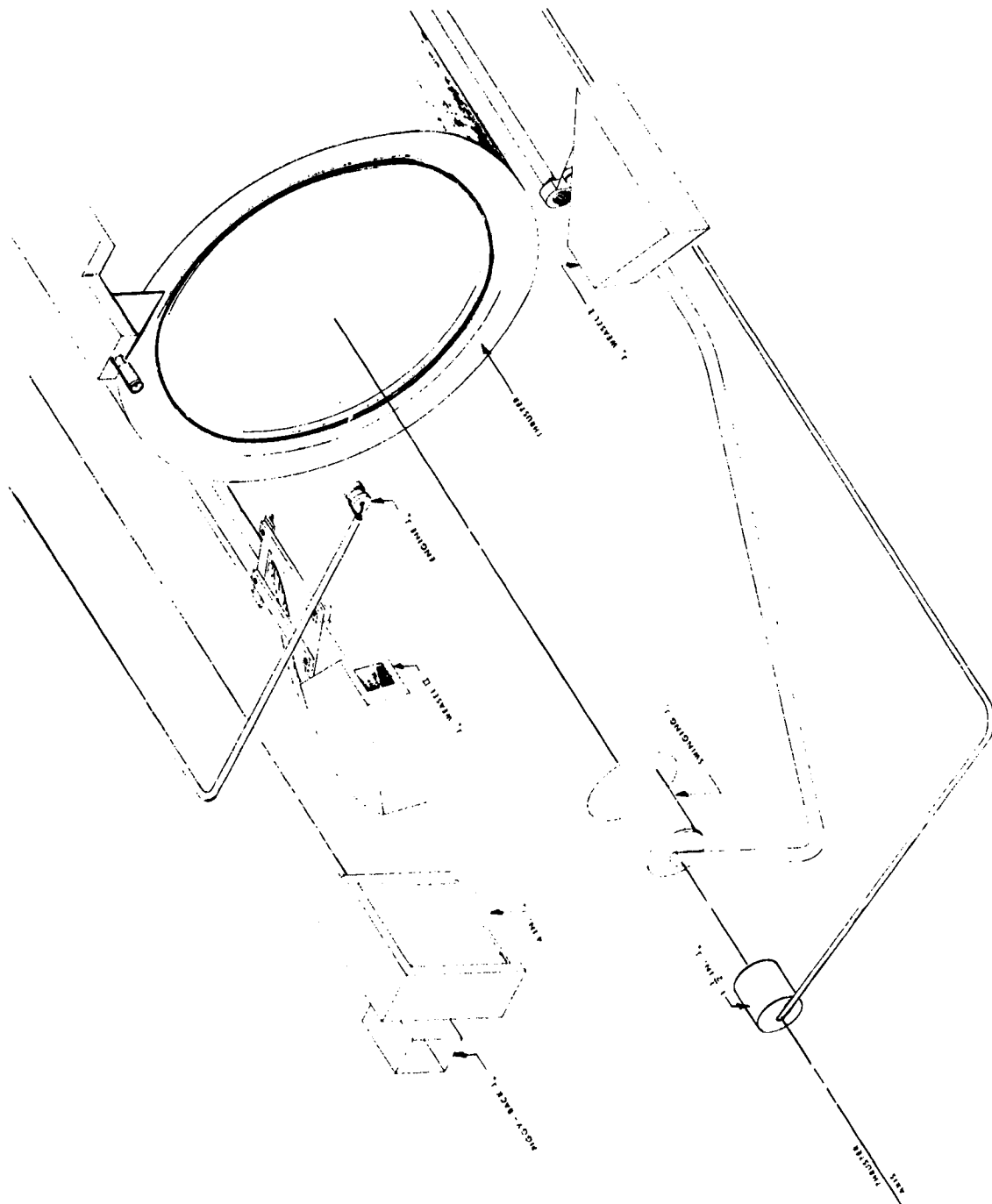


Figure 2. Isometric View of 30 cm Ion Thruster and Diagnostic Probe Array.

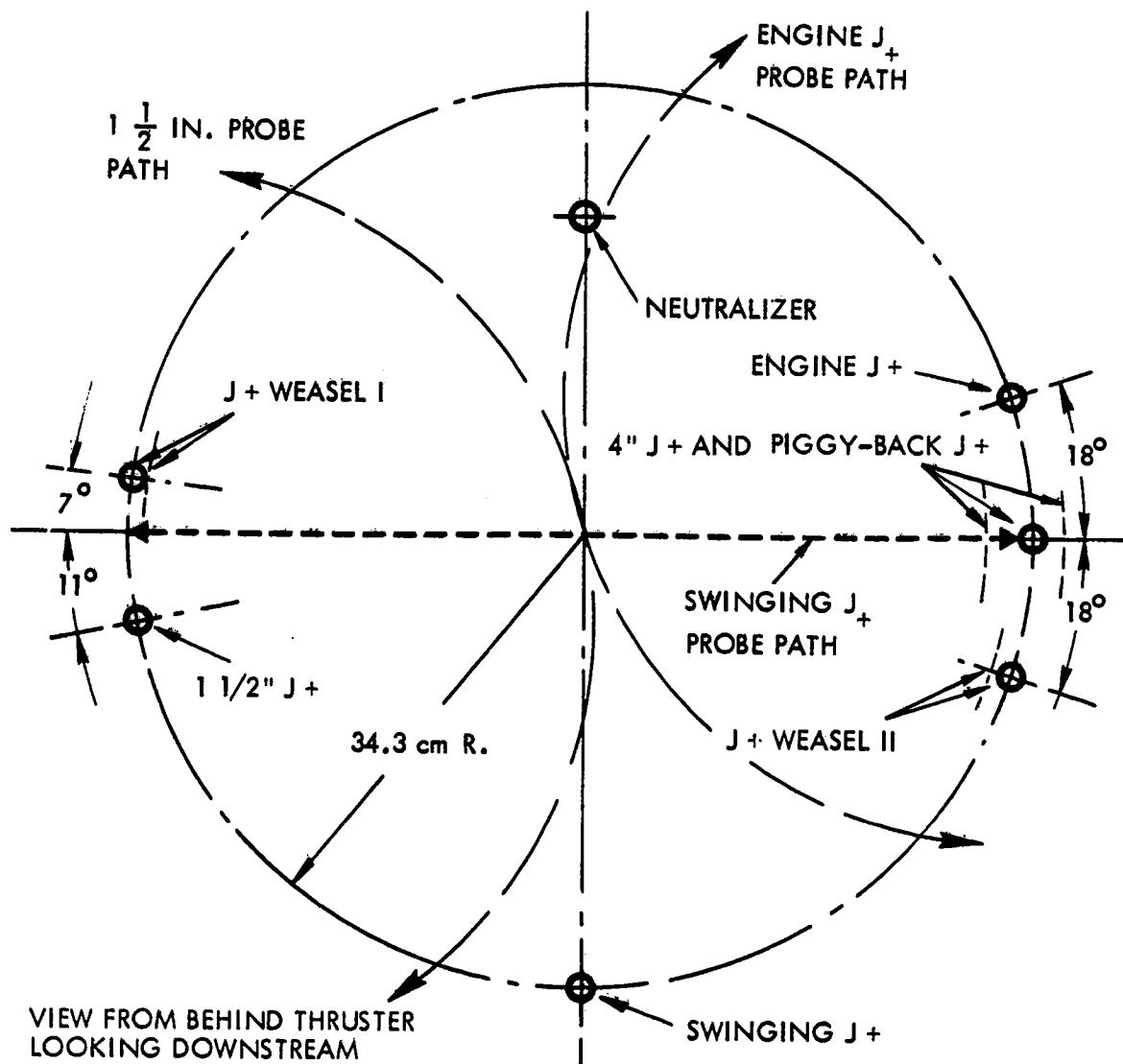
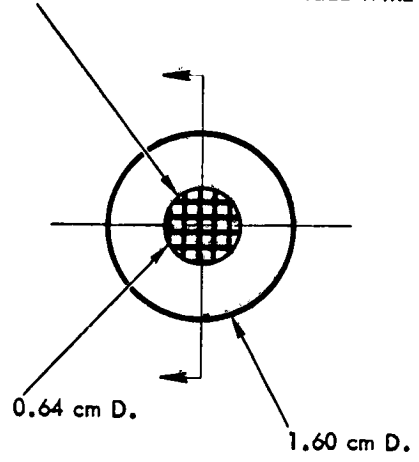
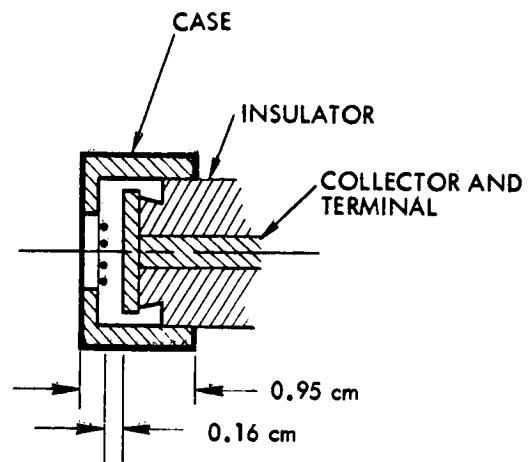


Figure 3. View Along Thrust Beam (z) Axis Illustrating Radial Distance and Azimuthal Position of Diagnostic Probe Mounting Rods. Probe Motion and Position Indicated for Engine J<sub>+</sub>, 1-1/2" J<sub>+</sub>, and Swinging J<sub>+</sub>. Probe Radial Position for 4" J<sub>+</sub>, Piggyback J<sub>+</sub>, and J<sub>+</sub> Weasel I and Weasel II also Indicated.

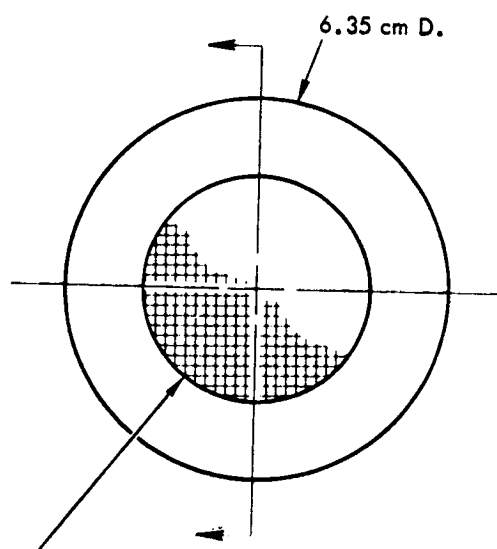
GRID: 22 X 22 PER INCH MESH,  
0.0075" D. STAINLESS STEEL WIRE



ENGINE J<sub>+</sub>  
EFFECTIVE COLLECTION AREA = 0.221 cm<sup>2</sup>

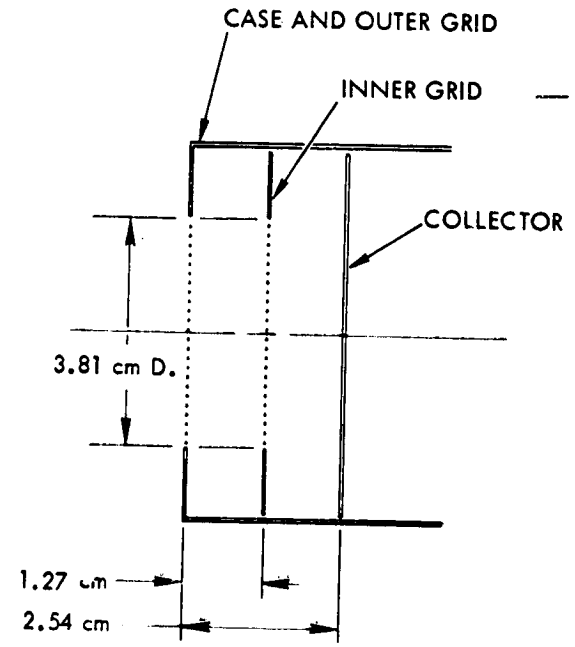


AXIAL RANGE FROM  
Z = 4.7 TO Z = 40 cm



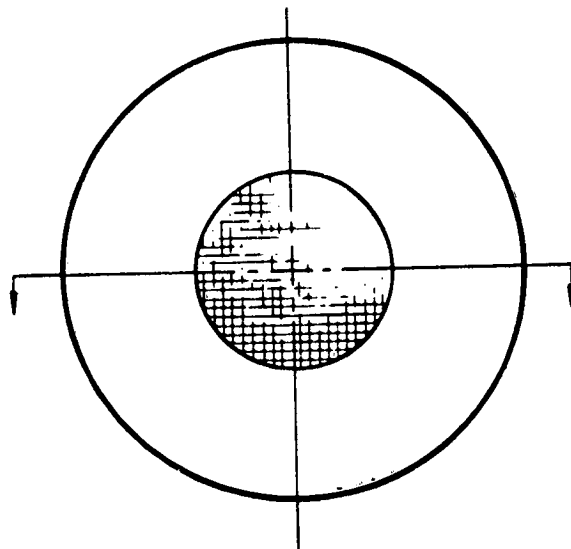
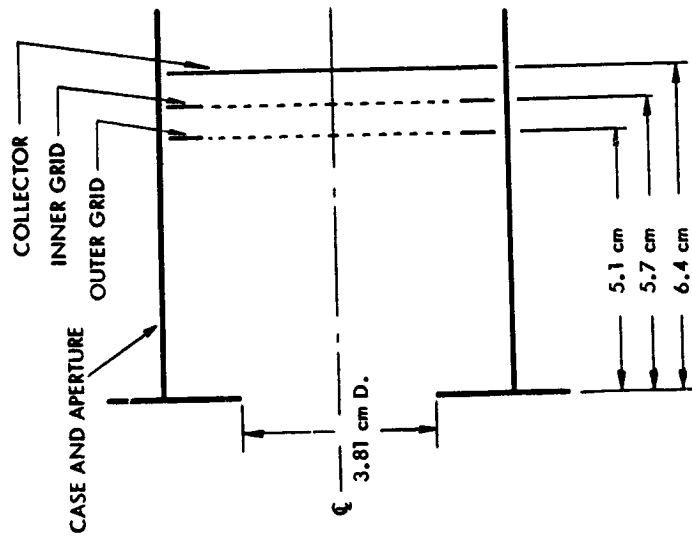
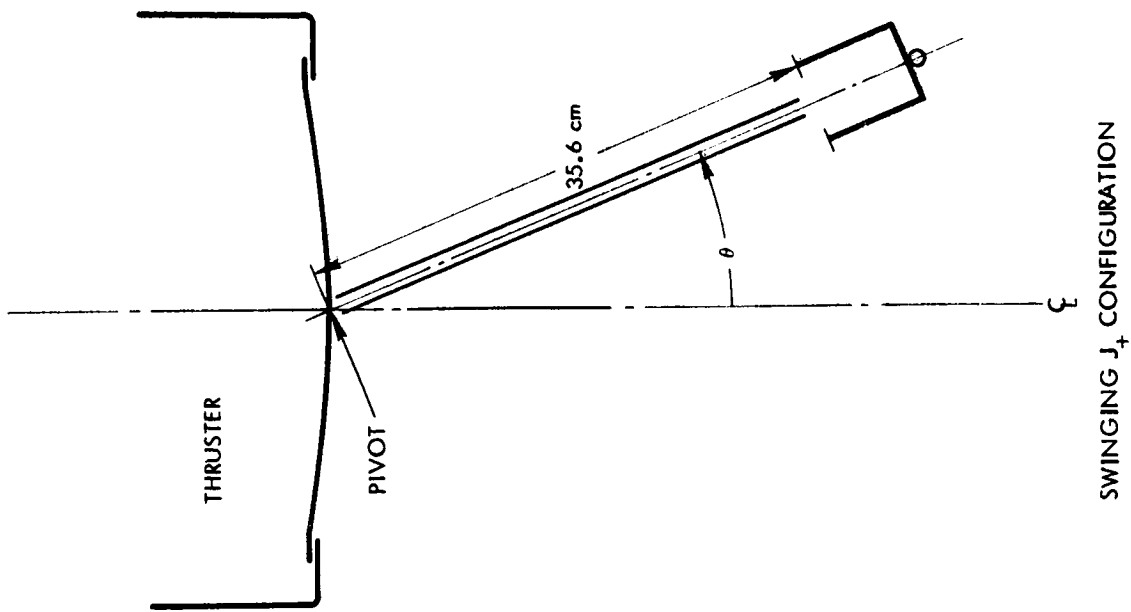
GRIDS: 16 X 16 PER INCH MESH,  
0.009" D. STAINLESS STEEL WIRE

1 1/2 IN. J<sub>+</sub>  
EFFECTIVE COLLECTION AREA = 6.12 cm<sup>2</sup>



AXIAL RANGE FROM  
Z = 35 TO Z = 100 cm

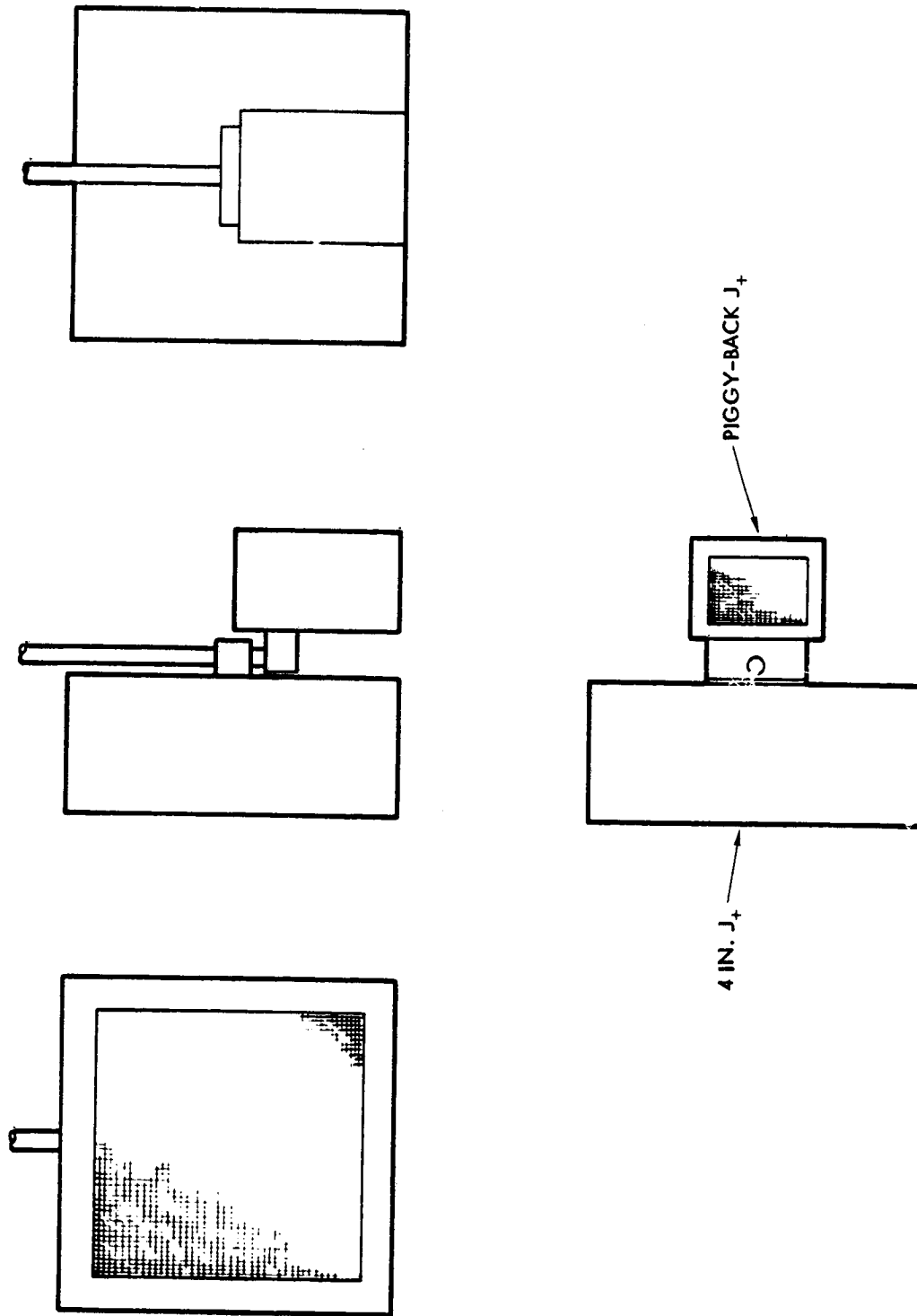
Figure 4. Outer Case, Grid, and Collector Configuration on Engine J<sub>+</sub> and 1-1/2" J<sub>+</sub> Probes.



GRIDS: 16 X 16 PER INCH MESH,  
0.009" D. STAINLESS STEEL WIRE

SWINGING  $J_+$  EFFECTIVE COLLECTION AREA = 6.12 cm<sup>2</sup>

Figure 5. Outer Case, Grids, and Collector Configuration of the Swinging  $J_+$  Probe, and Probe Orientation and Motion.



4 IN. J<sub>+</sub> AND PIGGY-BACK J<sub>+</sub> PROBE PACKAGE

Figure 6. 4" J<sub>+</sub> Probe and Piggyback J<sub>+</sub> Probe Overall Layout and Orientation.

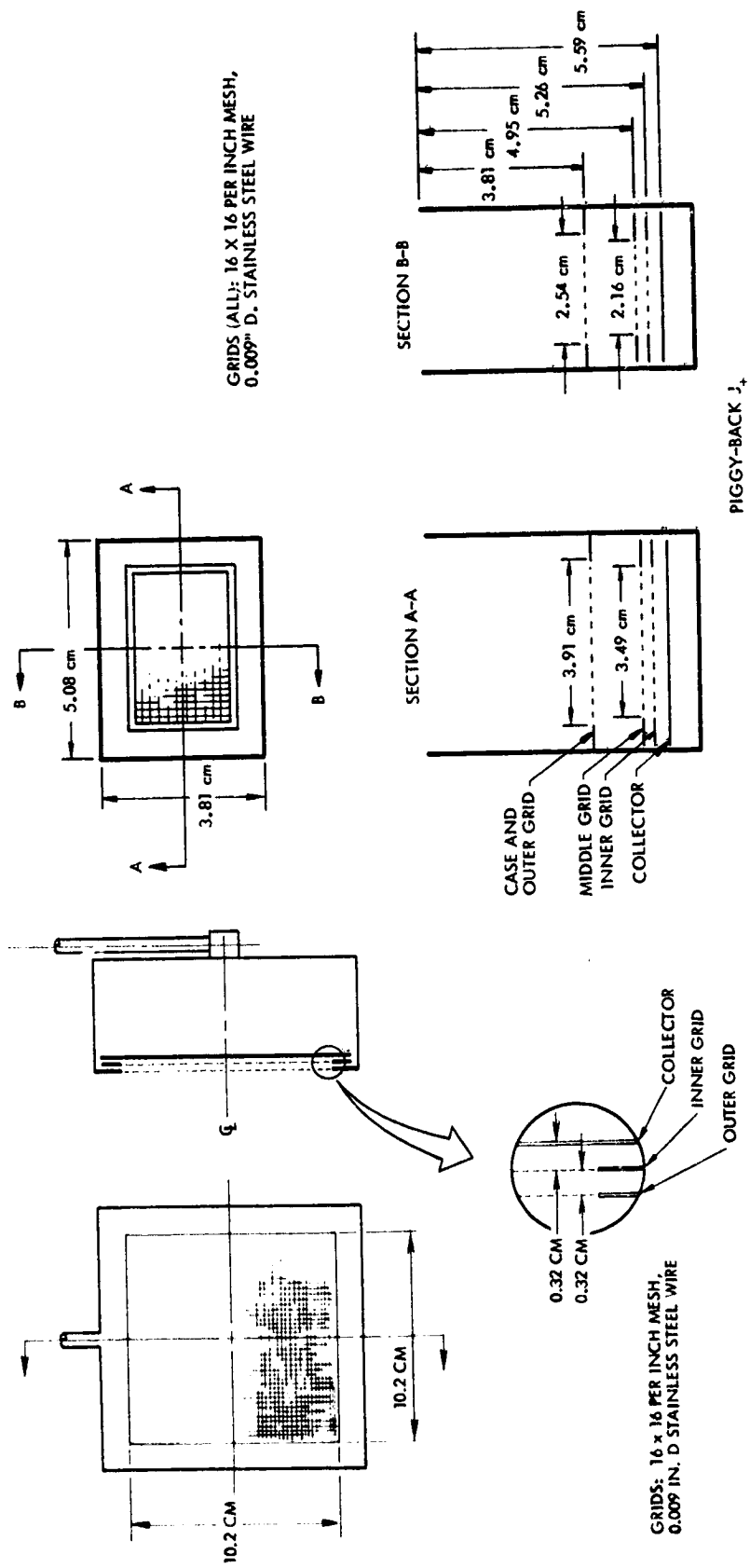
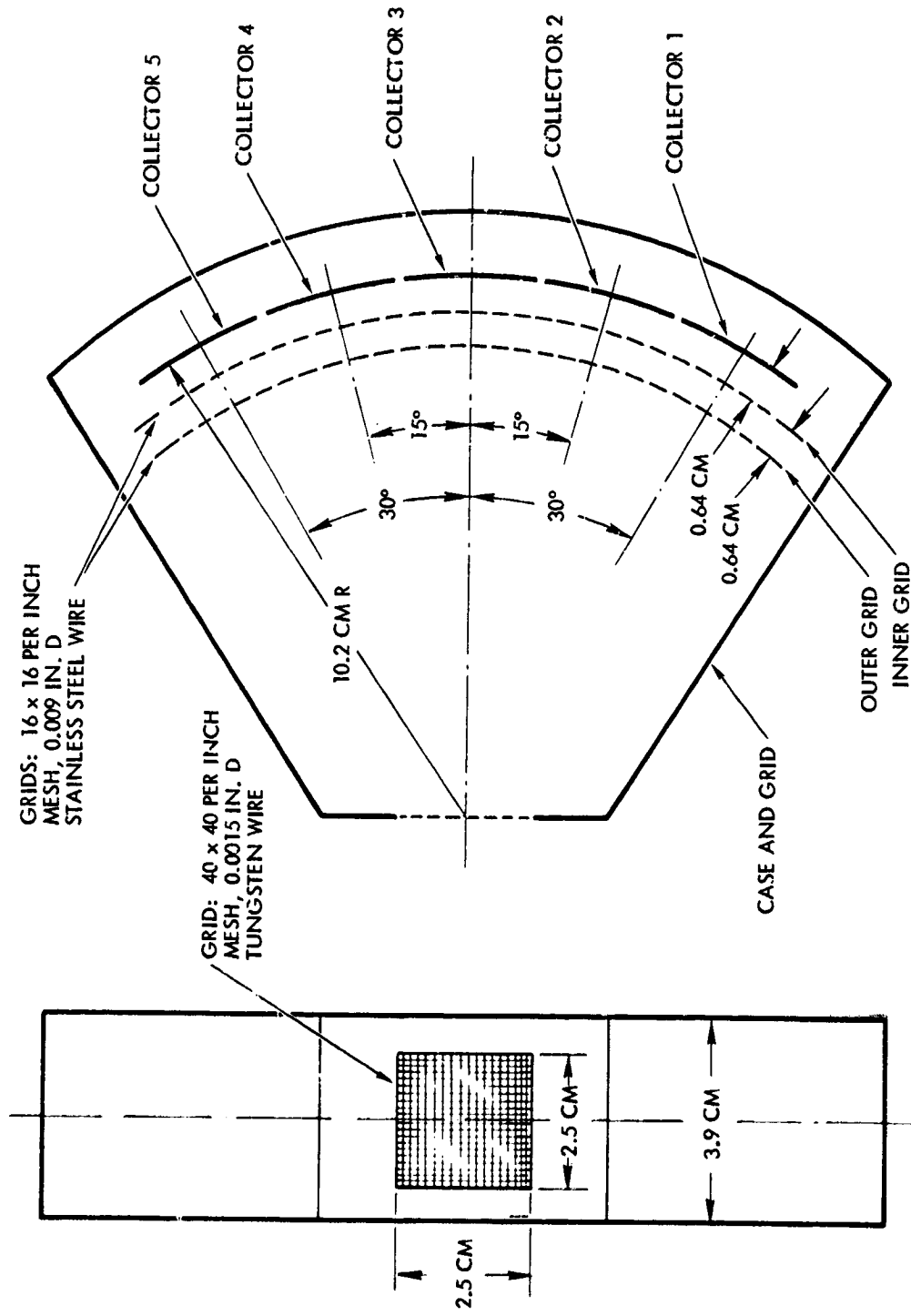


Figure 7. Outer Case, Grid, and Collector Configuration on 4" J<sub>+</sub> and Piggyback J<sub>+</sub> Probes.



J<sub>+</sub> WEASEL I AND II

Figure 8. Outer Case, Grid, and Collector Configuration on J<sub>+</sub> Weasel I and II Probes.

an arc which passes through the axis of the thrust beam, thus allowing the probe to determine thrust ion current density as a function of  $r$  and  $z$  in a cylindrical coordinate system,  $(r, z, \phi)$ , whose  $z$  axis is the beam axis. When the case and the collector are connected to each other and isolated from chamber ground by a high impedance (10 megohms), the probe acts as a floating probe to determine the floating potential in the neutralized thrust beam for the same  $r$  and  $z$  locations for which the probe, used as a Faraday cup, determined ion current density.

The 1-1/2"  $J_+$  probe is also illustrated in Figure 4. This three element probe consists of an outer grid and case, an inner grid, and a collector and, by setting a negative bias on the outer grid and varying the bias on the inner grid, permits the use of the probe as a retarding potential analyzer. The probe, thus, not only determines ion current density, but, through retarding potential analysis permits a determination of the energy spectrum of arriving ions. The mounting and motion of this probe is the same as that used in the Engine  $J_+$  except that a longer mounting shaft is used, thus permitting ion current density measurements to be carried out over a larger interval in axial distance,  $z$ , than is possible with Engine  $J_+$ .

Figure 5 illustrates the motion and construction details of the Swinging  $J_+$  probe. The axis of this four element probe (outer case and aperture, inner and outer grids, and collector) intersects the face of the thruster at the thruster axis ( $r = z = 0$ ) and remains fixed on that point as the probe is rotated. The probe motion, thus, is in  $\theta$ , where  $\theta$  is the angle of divergence from the thrust beam axis, and results from a drive shaft through the Swinging  $J_+$  probe mount and appropriate gears and coupling to cause the probe arm and probe motion. The function of the probe is ion current density as a function of divergence angle and ion energy.

Figures 6 and 7 provide views of the 4"  $J_+$  probe and Piggyback  $J_+$  probe package. Figure 6 (see also Figure 2) shows the probe package as viewed from various directions. Details of the collector, inner grid, and outer grid (and case) of the three element 4"  $J_+$  and the collector, inner grid, middle grid, outer grid (and aperture and case) of the four element Piggyback  $J_+$  are given in Figure 7. The probes,

used as retarding potential analyzers, provide a measure of ion current density as functions of probe position and ion energy. The 4"  $J_+$  has a comparatively broad acceptance cone of directions and in its usual orientation determines the totality of ion current impinging on a surface whose surface normal is in the radial direction (in the cylindrical coordinate system described earlier) and which intersects the thrust beam axis at location  $z$ . Through motion of the 4"  $J_+$  mounting shaft the location in  $z$  is varied. The face of the 4"  $J_+$  is at  $r \approx 28$  cm.

Because of the width of the collector plate relative to the spacing between grids and because of collector placement within the outer case, the 4"  $J_+$  determines the total current of ions moving in the  $\theta$  range from  $\sim 0^\circ$  to  $\sim 180^\circ$  and intercepting the cylindrical surface,  $r = r_{\text{probe}}$ , at  $z = z_{\text{probe}}$ . The angular range of the Piggyback  $J_+$  probe is more restricted, however, and it serves primarily to measure ion currents in the "backward" ( $\theta \sim 180^\circ$ ) direction, again, as a function of probe location  $z$ . The principal interest in these backward streaming ions is in terms of facilities effects, since operation of the thruster in space does not, in general, lead to any significant levels of ion current in this reverse direction.

A final figure illustrating probes in the array is Figure 8, which shows details of the  $J_+$  Weasel I and II probes. The  $J_+$  Weasel contains 5 separate collectors. The collectors lie behind an inner and outer grid, each of which is separately biasable, and inside an outer case and grid which is also separately biasable. The probe moves in the  $z$  direction through the motion of the mounting shaft. In common usage the axes of the various collectors intersect the thruster axis. In this orientation the probe determines ion current density as a function of ion direction of travel in  $\theta$ . The angular width of each collector (in conjunction with the aperture in the case) is  $\sim 30^\circ$ . By exercising probe motion and bias it is possible, in principle, to determine ion current density as a function of  $\theta$  and ion energy at position  $z$  for  $z$  along a cylinder of radius  $r_{\text{probe}}$ .

### 3.0 FACILITIES EFFECTS

#### 3.1 General Considerations

The operation of an ion thruster results in the release of several forms of particles, including both charged and neutral species with energies varying over a broad range for both forms of particles, and a variety of RF and optical emissions. The measurement of these wave and particle fluxes constitutes the principal tasks in determining interactive effects between the thruster, the ambient space, and a spacecraft. For laboratory determinations of interactive effects, measurements (of necessity) are conducted in the bounded geometry of the laboratory test chamber, and the term "facilities effects" can be interpreted to mean any alteration of a measurement of thruster wave and particle release resulting from the presence of the testing chamber. In this program report, the concern of facilities effects will be more narrowly limited to measurements of the charged species.

In principle it should be possible, by increases in chamber size or by reductions in chamber background pressure, to lower the level of facility effect particle fluxes below the levels of "genuine" particle emissions from the thruster. In practice, and depending upon the specific details of a given measurement, the reduction of facilities effects to negligible levels may not be easy, and, in some instances, may not be possible in any real and practical sense. Key elements in assessing possible influences of facility effects is the spatial location of a field point in question, the direction of arrival of particles examined by a probe, and the energies of the particles examined. Measurements of thrust ions for probes situated on or near the thruster axis should not be influenced significantly by facility presence. Measurements of very dilute fluxes of charged particles at either large spatial separation from the primary beam or at very high angles of divergence from the thrust beam axis may be significantly influenced or even dominated by facilities effects. The discussion in this and the following sections will attempt to identify some of the reactions and locations for which facility effects are of concern.

### 3.2 Neutral Particle Species

In the period before onset of thruster operation, neutral particle species include the common gases for laboratory chambers ( $N_2$ ,  $O_2$ ,  $H_2O$ , and hydrocarbons (these last from diffusion pump backstreaming, vacuum grease coverings of seals) and unpumped mercury atoms). Even with the complete activation of the cold walls,  $Hg^0$  will continue to persist at some level, as sources of previously accumulated mercury from previous thruster operation periods release  $Hg^0$  which is, in turn, cryopumped on the baffles. Under maximum  $LN_2$  cooling of the shrouds and collector in the 5' x 11' chamber, total pressure (all gases) is  $\sim 2 \times 10^{-6}$  Torr, with principal fractions (assumed) of  $Hg^0$ ,  $H_2O$ ,  $N_2$  and  $O_2$ .

The operation of the ion thruster will raise the measured chamber pressure somewhat and also creates some neutral species that are not determined accurately by ion gauges (which, of necessity, must be somewhat removed from the path of the thrust beam). A principal increase in ion gauge reading of chamber pressure due to thruster operation will be in  $Hg^0$ , the bulk of which is probably at low energies ( $\sim kT_{wall}$  for those portions of the chamber walls not refrigerated). In addition, the impact of energetic thrust ions on the collector and the shrouds creates the following groups of neutral particles:

- 1) sputtered  $Hg^0$  (previously cryopumped on locations impacted by thrust ions),
- 2) sputtered metal atoms from the collector and shrouds,
- 3) sputtered  $H_2O$  (previously cryopumped on locations impacted by thrust ions) and
- 4) bouncing, neutralized, energetic  $Hg^0$  (from  $Hg^+$  impact on the collector with charge neutralization following, but not sticking).

Of the species identified above, all may be expected to have energies significantly above wall temperatures during their initial flight (following sputtering and until an encounter with another wall). After the initial flight, sputtered metal atoms will probably stick to any of the chamber walls and will remain accommodated there unless the area is subject to continued thrust ion bombardment. Groups 1, 3, and 4 above

may or may not stick to the first wall encountered after the initial flight. If the first wall encounter is an LN<sub>2</sub> cooled surface, sticking is expected. Accommodation and subsequent release at relevant vapor pressure rates would be expected for non-cooled portions of the chamber boundaries.

The density of "hot" (of the order of several eV for sputtered particles) neutrals in testing chambers is non-trivial, considering here that sputtering ratios of Hg<sup>+</sup> thrust ions may range well above unity and that the streaming velocity of sputtered neutrals is significantly less than Hg<sup>+</sup> thrust ion velocity. In various regions of the chamber, then, weakly energetic neutral atom densities exceed the densities of Hg<sup>+</sup> thrust ions. As will be discussed in Section 3.4, these weakly energetic neutrals can react in specific forms to produce observable facility effect fluxes, principally in the backward moving ions.

While weakly energetic neutrals are the principal cause of some facility effects, the major facility effect is that produced by thermal (wall temperature) mercury atoms acting in charge transfer reactions with Hg<sup>+</sup> thrust ions. Section 3.4 will discuss this reaction in further detail, and Section 5 will model expected fluxes of these charge transfer facility effect ions.

### 3.3 Charged Particle Species

Section 3.2 has noted charge transfer reactions between Hg<sup>+</sup> and various neutral species in the testing chamber as a source of facility effects ions. In addition to these reaction produced ions, there will be small quantities of Hg<sup>+</sup> resulting from primary Hg<sup>+</sup> thrust ion bounce from the collector, without neutralization during the contact period. These backward moving (and probably weakly energetic) ions would not be distinguishable from weakly energetic (bouncing) Hg<sup>0</sup> which charge transfers against an Hg<sup>+</sup> thrust ion to produce backward traveling ions.

### 3.4 Facility Effects Reactions

The measurements program reported here has been specifically directed to ion flux measurements, so that the facilities effects reactions of interest here are those which result in charged particles. As discussed

above, facilities effects ions can result from thrust ion bounce, without neutralization, upon impact with the collector. The expected flux of bouncing ions is, however, small, and the major concern for facilities effects ions will be from charge transfer reactions between thruster ions and facility neutrals. In the charge transfer reaction,



an initial ion,  $A^+$ , and neutral,  $B^0$ , exchange charge state through electron transfer. In assessing relative magnitudes to facilities effects, the created charge species will depend upon the combined densities of  $A^+$  and  $B^0$  and the charge transfer cross section,  $\sigma_{cx}$ . The charge exchange cross sections attain largest values for "resonant" charge transfer. For example, the reaction



is resonant ( $\Delta E = 0$ ) and has a cross section of  $\sim 5 \times 10^{-15}$  square centimeters, for relevant values of intraparticle collision energies.

Of the several facility neutral particle species and thruster ion species, the two largest facility effects reactions both involve resonant charge transfer between  $Hg^+$  and  $Hg^0$ . In the first, the transfer occurs between  $Hg^+$  thrust ions (Group I) and ambient chamber  $Hg^0$ , largely at wall temperatures. This reaction perturbs measurements of "genuine" Group IV ions ( $Hg^+$ ,  $Hg^0$  charge transfer downstream of the accelerator grid for ions and atoms leaving the thruster). The second major facility effect reaction involves sputtered (weakly energetic)  $Hg^0$  charge transfer with  $Hg^+$  thrust ions and causes backwards moving ( $\theta \rightarrow 180^\circ$ ) facility effect ions. A final facility effect of interest involves charge transfer between ambient chamber  $Hg^0$  back diffusing into the ion acceleration space and producing a facility generated Group II ion which perturbs measurements of "genuine" Group II ion fluxes.

While other forms of ( $A^+$ ,  $B^0$ ) charge transfer occur in the test chamber (for example, sputtered metal atom,  $Hg^+$  charge exchange), the relatively reduced magnitudes of non-resonant charge transfer cross sections indicates that these are not significant contributors to observed facility effects currents.

### 3.5 Assessment of Facility Effect Current Magnitudes

Since facility effect ion currents will be measured with and will perturb genuine ion fluxes, it is desirable to assess the magnitudes of these spurious ions. In this program two approaches have been used, and each approach has limitations in the accuracy of assessment. The first approach, to be discussed in greater detail in Section 5.0, is analytical and involves calculations of ion generation between known thrust ion beams and modeled  $\text{Hg}^\circ$  ambient densities. Uncertainties in this approach result from uncertainties in the ultimate deposition patterns of these calculated facility effects currents. A second, experimental, approach involves deliberate variation of ambient chamber pressure (for example, by controlling the temperatures of the  $\text{LN}_2$  cooled shrouds), observing ion currents as a function of measured chamber pressure and extrapolating observed ion fluxes to zero chamber pressure. The uncertainty in this approach results from possible variations in the partial pressures of the various chamber gases as total chamber pressure is varied. It should be emphasized, furthermore, that various gas species do not have identical ion gauge constants. An increase in ion gauge indicated chamber pressure by a factor of two, (for example, by allowing shroud temperature to rise) does not mean that ambient  $\text{Hg}^\circ$  pressure increased by a factor of two. Instead, a relatively higher fraction of the chamber pressure gain could have been obtained by increases in background water vapor than from  $\text{Hg}^\circ$ , since cryopumping of  $\text{H}_2\text{O}$  at the baffles loses effectiveness before a loss of cryopumping of  $\text{Hg}^\circ$ . Thus, while chamber pressure variation measurements are interesting, there are possible inaccuracies, and, to reduce the perturbation of genuine ion flux measurements by facility generated effects currents, the best procedure is to have the maximum possible pumping of ambient  $\text{Hg}^\circ$ . In the measurements to be discussed in the sections following, facility generated "noise" is, generally speaking, below the genuine ion "signal". As noted earlier in Section 3.1, however, for increasing physical separation and increasing angular divergence, spurious effects increase in magnitude relative to genuine currents, and, for certain energy, angular, and spatial regimes, become the dominant terms.

#### 4.0 LOW ENERGY ION MEASUREMENTS

##### 4.1 General Considerations

Low energy ion measurements were obtained from retarding potential analyses of the probe signals of the 4"  $J_+$ , Swinging  $J_+$ , and the Piggyback  $J_+$ . Low energy ion measurements were also obtained by the Weasel  $J_+$  probes. While the probe data from the multi-collector Weasel probes is included in the Engine Operation Data volume, they will not be treated further in this report because of undetermined (and, perhaps, undeterminable) low energy ion trajectory refraction effects which may be present in the collection and analysis of these particles.

The low energy ions to be treated in this section are primarily Group IV  $Hg^+$  ions created by charge transfer reactions between  $Hg^+$  thrust ions and  $Hg^0$  atoms. If the  $Hg^0$  atom in the reaction is in its initial passage through the test chamber (having emerged from the thruster and before the first encounter with a chamber boundary), the ion formed is a genuine Group IV and would be present for thruster operation in space. If the  $Hg^0$  atom is an ambient chamber particle, the Group IV ion formed is a facility effect ion.

The trajectories and velocities of Group IV ions (both genuine and facility generated) have been examined in References 3 and 4 and will be described further in Section 5.0 of this report. In brief, the energy of the ion immediately after the charge transfer is essentially the energy of the atom ( $\sim kT$  where  $T$  is either the thruster wall temperature or chamber wall temperature). The ion is then acted on by the electric field structure in the plasma formed by thrust ions and neutralizing electrons. Potential variations in this thrust ion plasma are of the order of a few  $kT_e$  where  $k$  is Boltzmann's constant and  $T_e$  is thrust beam electron temperature. For typical neutralization conditions,  $kT_e$  is approximately a few tenths of an electron volt, so that Group IV ions, moving in these electric fields, acquire energies which are only of the order of electron volts and, hence, are easily altered in trajectory by electric fields in the sheath regions between the plasma beam and the surfaces of probes measuring these ions. These refracting electric fields can severely perturb measurements of ion directionality

at the probe location. The deposition patterns of the Group IV ions are not severely perturbed by the presence of probes, however, and, for this reason, data from the 4"  $J_+$  probe (a wide acceptance angle, total ion diffusion current measuring probe) can be utilized. (Deposition pattern measurements are not affected because ion deposition points are determined by the integral of  $\vec{E}$  along the path, and these integrals and path lengths are substantially larger, in general, than for the integral and path length of perturbation fields in regions surrounding the probe).

One further consideration in the usability of  $J_+$  probe signals for Group IV ion measurements is the extent of other, and competing, ion flux signals. For probe locations in increasingly dense portions of the thrust beam, the currents of Group I and Group II ions into a cup can be significantly larger than the low energy Group IV ions. Under these conditions the method of retarding potential analysis becomes increasingly subject to error from spurious effects arising from energetic ion currents. For this reason, Group IV measurements for large and increasing axial distance  $z$  are increasingly subject to error. A mitigating circumstance, however, is that these are not the regions of principal concern for Group IV deposition effects.

#### 4.2 Testing Chamber Ambient Pressure Effects

Section 3.0 has discussed facilities effects and has noted the production of spurious Group IV ions by charge transfer between  $Hg^+$  thrust ions and ambient  $Hg^0$ . Such effects can be examined by deliberate variations in the density of ambient  $Hg^0$ , although (as noted in Section 3.4) this procedure is imprecise because of possible variations in the relative partial pressures of ambient neutrals as overall chamber pressure is varied.

To produce variations in ambient neutral density, the rate of liquid nitrogen feed to the upper shroud in the test chamber was varied. Under maximum  $LN_2$  cooling, chamber pressure readings from the ion gauge are in the range from 2 to  $4 \times 10^{-6}$  Torr. Reducing the  $LN_2$  feed to the upper shroud increases chamber pressure to values of  $\sim 8 \times 10^{-6}$  Torr. These chamber pressure variations caused the variations in Group IV ion flux illustrated in Figures 9, 10 and 11. The probe in use for

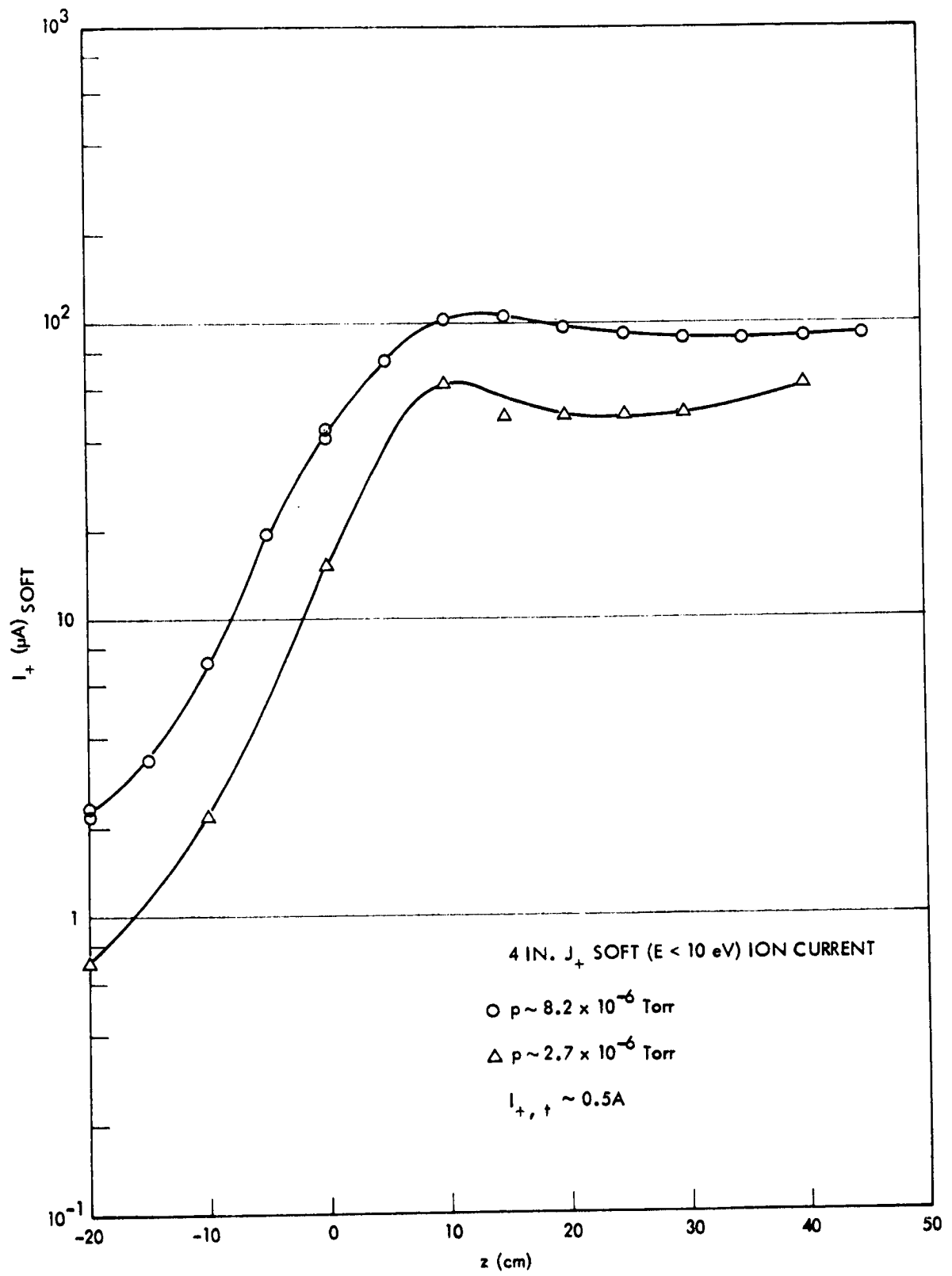


Figure 9. Low Energy  $Hg^+$  Charge Exchange Ion Flux in the 4"  $J_+$  Probe as a Function of Axial Distance,  $z$ , for Two Testing Chamber Pressure Conditions for a 0.5 Ampere Thrust Beam.

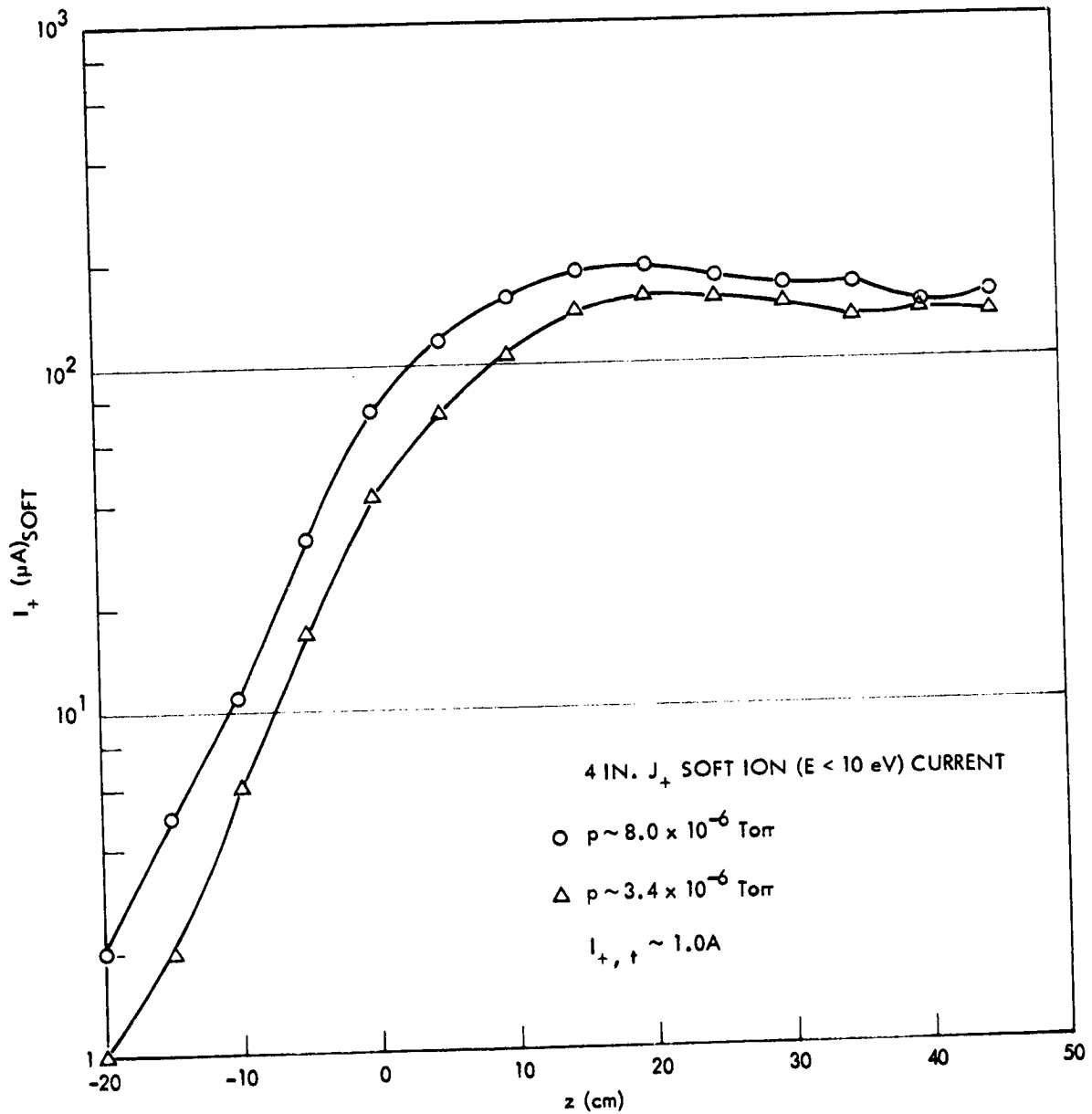


Figure 10. Low Energy  $Hg^+$  Charge Exchange Ion Flux in the 4"  $J_+$  Probe as a Function of Axial Distance  $z$ , for Two Testing Chamber Pressure Conditions for a 1.0 Ampere Thrust Beam.

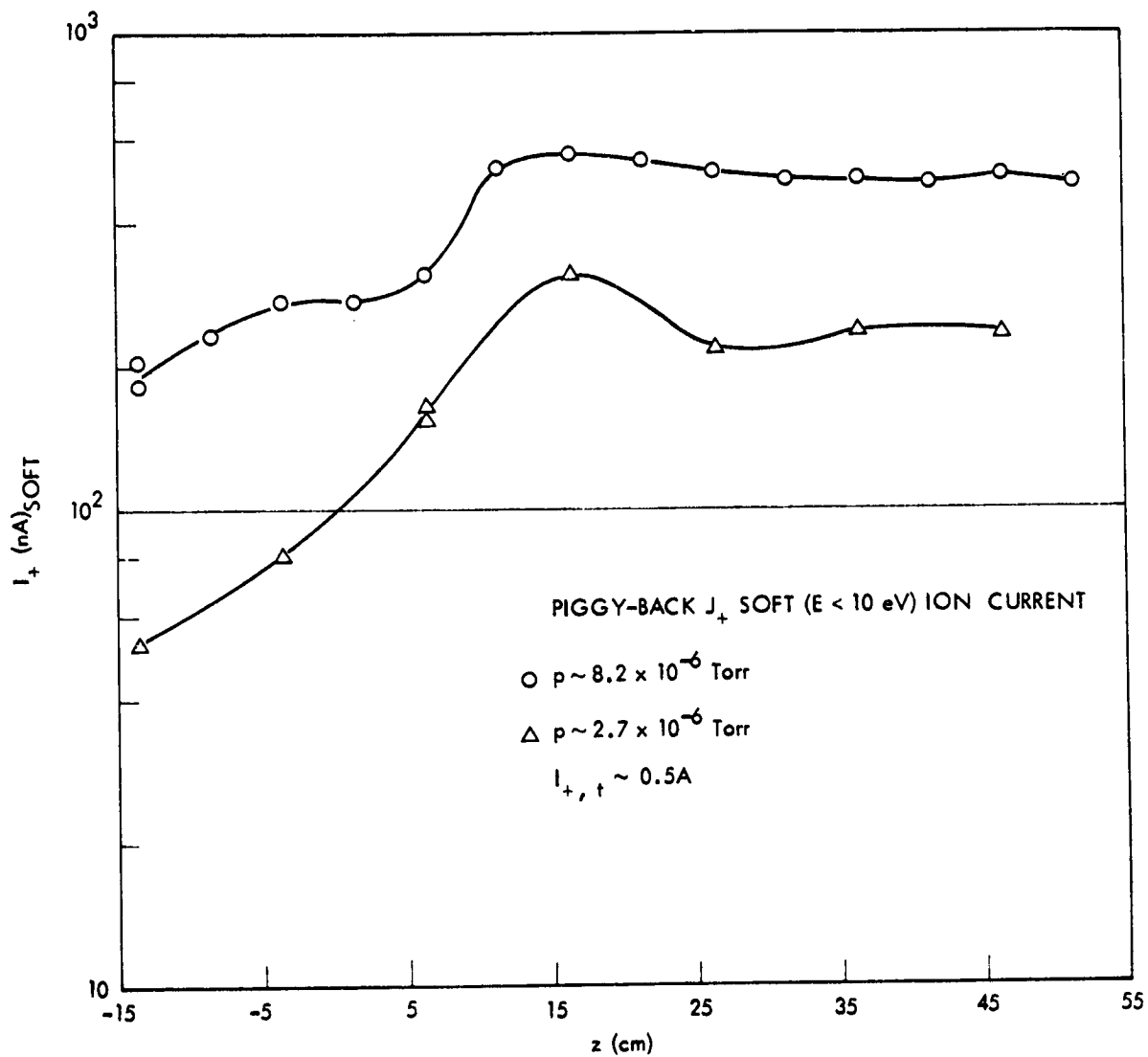


Figure 11. Low Energy  $Hg^+$  Charge Exchange Ion Flux in the Piggyback  $J_+$  Probe as a Function of Axial Distance,  $z$ , for Two Testing Chamber Pressure Conditions for a 0.5 Ampere Thrust Beam.

Figures 9 and 10 was the 4"  $J_+$ , used as a retarding potential analyzer to selectively record the low energy ion flux while the Piggyback  $J_+$ , also used as an RPA, was employed for the data in Figure 11.

From the data in Figures 9, 10, and 11 three conclusions may be drawn. The first of these is that facility effects are present in Group IV ion measurements. The second conclusion is that the effects of ambient  $Hg^0$  in producing low energy  $Hg^+$  are not everywhere equal and that certain regions and certain directions of probe orientation are more affected than others. The final conclusion is that, within selected regions and probe orientations, and for reduction of chamber pressure into the  $2$  to  $4 \times 10^{-6}$  Torr range, the bulk of the observed Group IV ion flux is genuine, that is, has resulted from a charge transfer between an  $Hg^+$  thrust ion and an  $Hg^0$  escaping from the thruster. Measurements of Group IV fluxes under these conditions, then, is a representative measurement of conditions that would occur for a thruster on a spacecraft.

By extrapolating the data of Figures 9 and 10 to zero pressure, it may be seen that for regions near  $z \sim 0$  for the 4"  $J_+$  probe, most of the observed signal is due to facility presence. In the region from  $z \sim 10$  centimeters to  $z \sim 25$  centimeters, and for the best pumping conditions, the 4"  $J_+$  probe signal is predominantly genuine Group IV. The evidence from the Piggyback  $J_+$  is somewhat more complex. In order to enter this probe, an ion trajectory must be at divergence angles in excess of  $\sim 135^\circ$  and, as will be seen later in the modeled ion trajectory calculations, it is difficult for genuine Group IV ions to attain these high backward angles. The bulk of the Piggyback  $J_+$ , then, is probably a facility generated Group IV flux, for all  $z$  and even under the best of pumping conditions. It does appear, however, for  $z$  in the range of  $\sim 10$  to  $\sim 25$  centimeters that a fraction of the observed signal is the result of genuine Group IV production. It should be noted here, however, that cup currents to the Piggyback are substantially lower than the currents to the 4"  $J_+$ . A part of this reduction may be attributed to reduced cup size and solid angle of acceptance for Piggyback  $J_+$  compared to 4"  $J_+$ , but, since the total cup currents have relative values separated by

$\sim 10^3$ , at least a portion of this reduction must be due to absolute reduction in low energy ion flux magnitudes at high angles ( $\sim 135^\circ$  to  $\sim 180^\circ$ ) compared to their magnitudes in the  $90^\circ \pm 45^\circ$  range. Thus, while some genuine Group IV flux may be present in the backward hemisphere, the magnitude is significantly lower than Group IV fluxes in the forward hemisphere.

#### 4.3 Characteristic Group IV Ion Flux Shape

In examining the 4"  $J_+$  determinations of Group IV ion flux in Figures 9 and 10 (and in the figures in the Engine Operation Data), a characteristic shape in the ion current pattern is apparent. The solid curve in Figure 12 illustrates this characteristic shape, identifies specific regions in the flow, and estimates the relative flux that would be obtained under space conditions where facility created ambient  $Hg^0$  has been eliminated.

In the regions of  $z < \sim 5$  cm (for the radial value of 28 cm of the 4"  $J_+$  probe, at angles of divergence,  $\theta$ , greater than  $\sim 80^\circ$ ) the probe current has an exponential behavior in  $z$ . In the range from  $z \sim 5$  cm to  $z \sim 20$  cm, the exponential rise gradually lessens to a plateau at  $\sim 20$  cm. For  $z > 20$  cm, the observed flux generally diminishes slowly before reaching a lower, almost steady, level.

The dashed curve in Figure 12 is an estimate of the genuine level of Group IV  $Hg^+$ . In Region I, genuine  $Hg^+$  is dominated by facility effect ions. A similar situation arises in Region III, in which a second problem of high "noise" levels of  $Hg^+$  thrust ions complicates the retarding potential analysis process out of which the low energy Group IV ions are identified. Only in Region II is the signal-to-noise ratio acceptable.

Probe location in Region II for determinations of Group IV  $Hg^+$  as a diagnostic of thruster operation is appealing not only because of improved signal-to-noise ratios, but also because of the more gradual variance of ion flux as a function of  $z$ . (Location of diagnostic probes in high gradient locations is potentially troublesome in that only minor changes in plume "shape" can cause major flux changes at a given location. In the plateau portions of Region II, such effects may be expected to be considerably reduced).

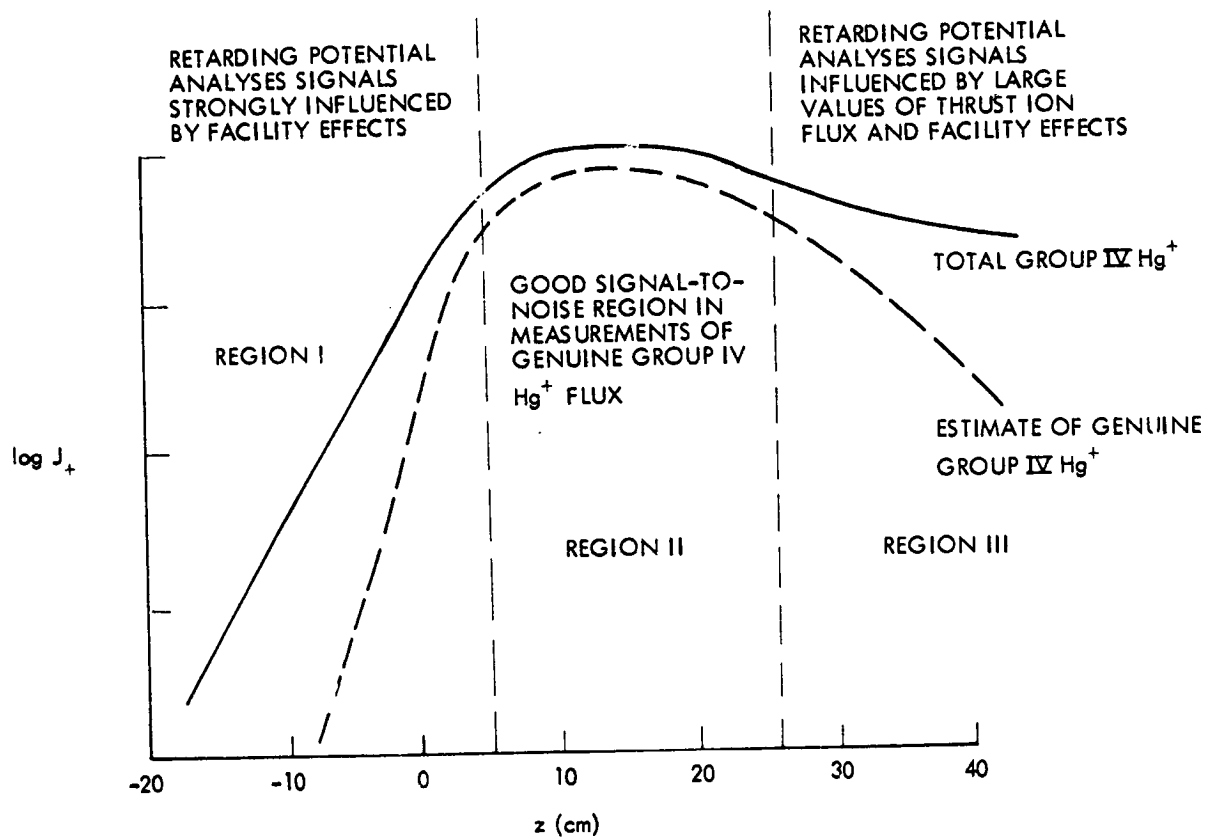


Figure 12. Characteristic  $Hg^+$  Charge Exchange Ion Signal in 4"  $J_+$  Probe and Estimated Genuine Flux as a Function of Axial Distance,  $z$ .

Figure 12's characteristic shape curves have been observed many times for the condition of both genuine and facility effect ions being measured. The estimated "true" flux (dashed curve) is subject to uncertainty. To fully remove uncertainty at  $z \sim 0$  by experimental measurements would require reduction in ambient chamber pressure to  $\sim 10^{-7}$  Torr, requiring, thus, the largest available test facilities and a high level of cold wall activation. Eliminating facility effects in Region III also will require  $\sim 10^{-7}$  Torr chamber pressure, noting, of course, that genuine  $\text{Hg}^+$  signals fall off for increasing  $z$  in this region and that, ultimately, measurements for increasing  $z$  will become measurements of facility generated particles.

It is also possible to reduce the uncertainty in the estimates of genuine flux by computing the expected genuine Group IV total production and comparing this value with  $\int J_+ dA$  along the cylinder on which the 4"  $J_+$  probe moves. Section 5 will discuss these computations further. For the present discussion it will be noted that  $\int J_+ dA$  from negative  $z$  values to  $z \sim 30$  cm provides a total measured current which is in close general agreement with modeled total Group IV ion production. In Region II, then, and for chamber pressures remaining within the  $4 \times 10^{-6}$  Torr range, the signal-to-noise ratio probably remains above 1, so that a firm lower bound estimate of genuine Group IV  $\text{Hg}^+$  in this region can be obtained by dividing the measured flux density by 2. Averaging measured and lower bound flux estimates leads to

$$\text{Group IV } J_+ \Big|_{\text{genuine, Region II}} \sim (.75 \pm .25) J_+ \Big|_{\text{measured}} \quad (3)$$

#### 4.4 Slow Ion Behavior as a Function of Thrust Ion Current

The 4"  $J_+$  probe was utilized in a series of beam scans in which thrust ion current was varied. The Group IV ion current density was then examined as a function of  $z$  as a function of  $I_{+,t}$ , using, as a first method of characterization the linear regression

$$J_{+IV}(z) = a_{IV}(z) + b_{IV}(z) I_{+,t} \quad (4)$$

For most  $z$  the intercept term  $a(z)$  was generally small, leading to a conclusion that, under proper engine operation, the Group IV ion current

density scales, generally, as thrust beam current. Table I lists the least squares fitted  $a_{IV}(z)$  and  $\epsilon_{IV}(z)$  for  $z$  from -20 cm to +40 cm at  $r = 28$  centimeters. Figure 13 illustrates values of 4"  $J_+$  cup current at various  $z$  values and as  $I_+$  is varied and the least squares fitted linear regression of this data.

Table 1. Linear Regression of  $J_+$  (Group IV) as a Function of Thrust Beam Current.

$z$ (cm)	$a_{IV}(z)$ ( $\mu\text{A}/\text{cm}^2$ )	$\epsilon_{IV}(z)$ ( $10^{-6} \text{cm}^{-2}$ )
-20	-.002	.029
-10	-.009	.095
-5	-.022	.312
0	-.054	.794
5	-.036	1.462
10	.054	2.184
15	.144	<u>2.527</u>
20	.054	2.383
25	.686	1.624
30	.360	1.877
35	.902	1.588
40	.415	2.166

The approximately linear behavior of  $J_+ IV$  with  $I_+$ , appears at first to violate reasonable assumptions of this dependence. Genuine Group IV ion production rate is clearly proportional to the product of the ion thrust current and the neutral atom current released by the thruster. If the thruster tended to operate at constant propellant utilization as  $I_+$  varied, then  $I_0$  (equivalent  $\text{Hg}^0$  release current) would be proportional to  $I_+$ , and the  $I_+ I_0$  product would be proportional to  $I_+^2$ . Some evidence of this  $I_+^2$  dependence in Group IV ions had been previously observed with a 20 centimeter thruster (Reference 1). The 30 centimeter diameter LeRC thruster, however, has been characterized as operating at increased

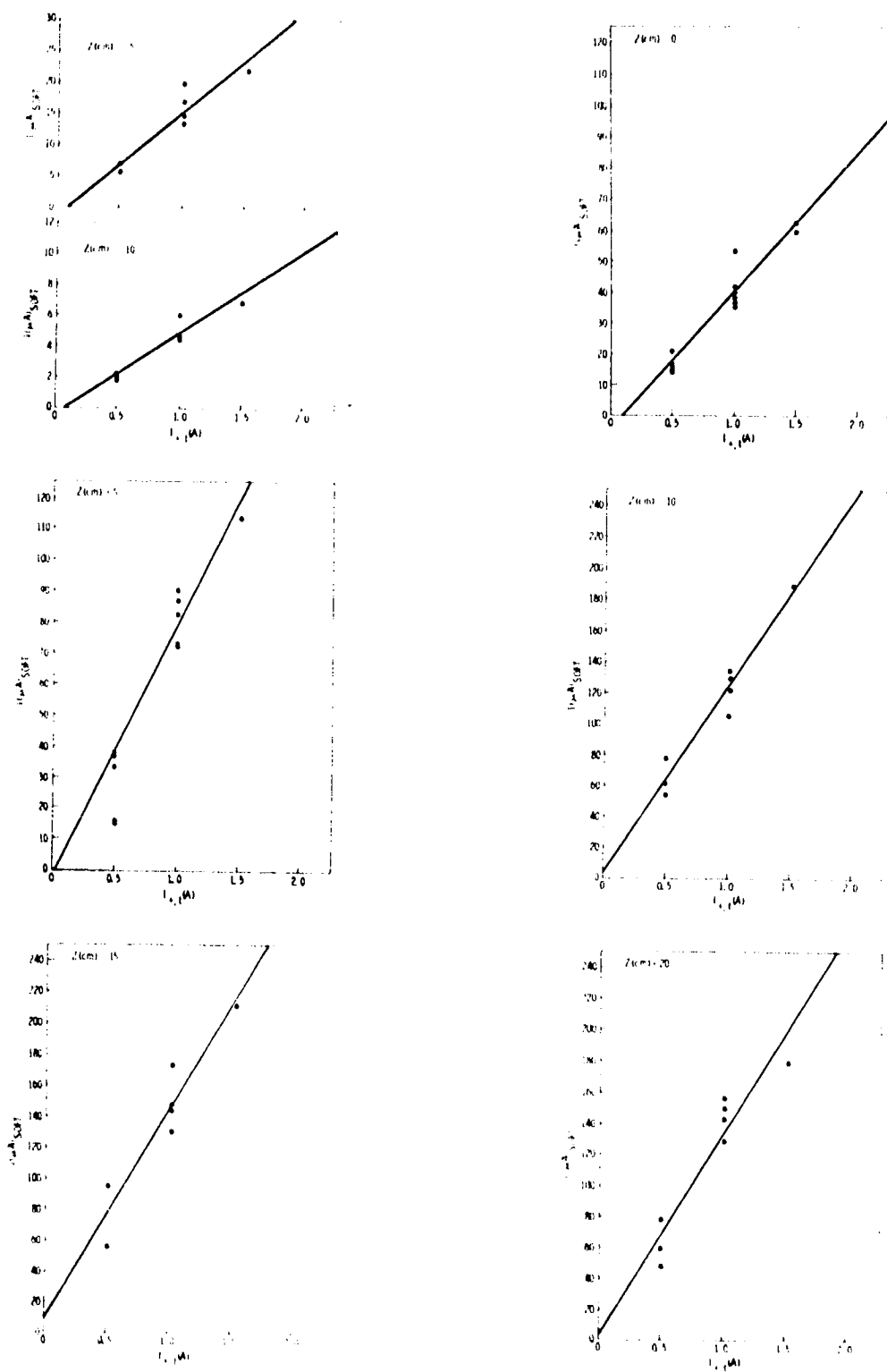


Figure 13. Hg<sup>+</sup> Charge Exchange Ion Flux in the 4" J<sub>+</sub> Probe as a Function of Axial Distance, z, and Thrust Beam Current, I<sub>+,t</sub>, and Least Squares Fitted Linear Regression.

propellant utilization for increasing thrust ion current, and Kaufman<sup>9</sup> has observed mercury bombardment discharges in which  $I_0$  remains essentially constant as  $I_+$  varies, for optimized discharge operation. Accepting  $I_0$  as fixed for  $I_+$  varying would lead to the approximately linear behavior of Group IV ion current with  $I_+$ , as given in Table I and Figure 13.

A remaining question in these Group IV ion measurements is the dependence of facility generated  $Hg^+$  charge exchange as  $I_+$  is varied. For facility effect ions, total production rate will be proportional to the product of the beam current  $I_{+,t}$  and the ambient chamber density in  $Hg^0$ . It would appear reasonable to assume that  $Hg^0$  ambient density is proportional to  $Hg^+$  beam current. For a purely cryopumped system, ultimate chamber pressure should be proportional to the rate of  $Hg^+$  inlet. The observed chamber behavior, however, is that pressure does increase with increasing beam current, but the relationship is more of the form  $k_1 + k_2 I_{+,t}$  where  $k_1 \sim k_2 I_{+,t}$  (for  $I_{+,t} \sim 2$  amperes). From this observed chamber behavior, the rate of facility effect Group IV ion production should be proportional to  $k_1 I_{+,t} + k_2 I_{+,t}^2$ , and the relevant question then becomes the magnitudes of  $k_1$  and  $k_2$  to each other and to  $\epsilon(z)$  in Equation 4. An examination of the linear regressions of Table I in the range  $-20 < z < +5$  centimeters shows strong linearity. Since this range in  $z$  is expected to be significantly influenced by facility effect charge exchange ions, it would appear that these ions are also almost linearly dependent on  $I_{+,t}$ , and that the  $k_1 I_{+,t}$  term generally dominates.

A final treatment of slow ion behavior has examined the Piggyback  $J_+$  signals as functions of  $z$  and  $I_+$ , again using linear regression. For a representation

$$I_+(\text{Piggyback}) = a_p(z) + k_p(z)I_{+,t} \quad (5)$$

the linear regression values given in Table 2 are obtained. In general, the probe signals were approximately linear in  $I_{+,t}$  although more scatter in the data was experienced for this probe than in the 4"  $J_+$  data given before.

The examination of the Piggyback  $J_+$  data was not specifically to gain further insight into the behavior of genuine Group IV ions since, as discussed earlier, the principal signals at these high divergence angles

will not be genuine but will, instead, result from the ambient chamber gas. The Piggyback data does, however, tend to confirm notions from the 4"  $J_+$  data that facility effect ions also scale linearly in  $I_{+,t}$ .

Table 2. Linear Regression of Piggyback  $J_+$  Signal as a Function of Thrust Beam Current.

<u>z (cm)</u>	<u><math>a_p(z)</math> (nA)</u>	<u><math>k_p(z)</math> (units of <math>10^{-9}</math>)</u>
-13.5	-6	80
-8.5	-6	101
-3.5	2	110
1.5	18	121
6.5	2	203
11.5	-108	546
16.5	22	432
21.5	-160	570
26.5	-30	380
31.5	-36	366
36.5	-28	356
41.5	-120	425
46.5	-60	380

#### 4.5 Slow Ion Behavior as a Function of Screen and Accelerator Potential

The Group IV ion flux was also examined as a function of net ion energy (screen potential varied for all other thruster potentials fixed) and as a function of accelerator voltage (for other thruster potentials fixed). Both of these variations lead to changes in the accel-decel ratio,  $R$ , where  $R = V_s / (V_s + |V_g|) = \frac{1}{\Gamma}$ , where  $\Gamma$  is the decel-accel ratio used in later sections.

For convenience here and for its use in later sections, Table 3A lists nominal thruster operation parameters at the various data points. In the data discussed in this section, thruster operation will be at points 16 and 18, 2 and 19, and 22, 23, 24. Table 3B lists actual engine operation conditions.

Table 3A. Engine Operation Data Points  
and Nominal Thruster Operational Parameters.

Data Points	Screen voltage (kV)	Beam currents (A)	Accel voltage (kV)	Emission current (A)	Discharge voltage (V)	Neut. flow rate	Neut. keeper current (A)	
	±.02	±.1	±.01	±.1	±.5	-	±.1	
1	1.1	2.0	0.5	12	37	Nom.	2.0	Beam current and propellant utilization efficiency
2	↓	↓	↓	10	↓	↓	↓	
3	↓	↓	↓	9	↓	↓	↓	
4	↓	1.5	↓	9	↓	↓	↓	
5	↓	↓	↓	7.5	↓	↓	↓	
6	↓	↓	↓	7	↓	↓	↓	
7	↓	1.0	↓	6	↓	↓	↓	
8	↓	↓	↓	5	↓	↓	↓	
9	↓	↓	↓	4.5	↓	↓	↓	
10	↓	0.5	↓	3	↓	↓	↓	
11	↓	↓	↓	2.5	↓	↓	↓	
12	↓	↓	↓	2.0	↓	↓	↓	
13	1.5	2.0	0.5	10	37	Nom.	2.0	Net ion energy
14	1.1	↓	↓	↓	↓	↓	↓	
15	0.7	↓	↓	↓	↓	↓	↓	
16	1.5	1.0	↓	5	↓	↓	↓	
17	1.1	↓	↓	↓	↓	↓	↓	
18	0.7	↓	↓	↓	↓	↓	↓	
19	1.1	2.0	Min +.03	10	37	Nom.	2.0	Accelerator voltage
20	↓	↓	0.5	↓	↓	↓	↓	
21	↓	↓	0.7	↓	↓	↓	↓	
22	↓	1.0	Min +.03	5	↓	↓	↓	
23	↓	↓	0.5	↓	↓	↓	↓	
24	↓	↓	0.7	↓	↓	↓	↓	
25	1.1	2.0	0.5	8.6	43	Nom.	2.0	Discharge voltage
26	↓	↓	↓	10	37	↓	↓	
27	↓	↓	↓	11.2	33	↓	↓	
28	↓	1.0	↓	4.3	43	↓	↓	
29	↓	↓	↓	5	37	↓	↓	
30	↓	↓	↓	5.6	33	↓	↓	
31	1.1	2.0	0.5	10	37	Nom.	3.0	Neutralizer keeper current
32	↓	↓	↓	↓	↓	↓	2.0	
33	↓	↓	↓	↓	↓	↓	1.0	
34	↓	1.0	↓	5	37	↓	3.0	
35	↓	↓	↓	↓	↓	↓	2.0	
36	1.1	2.0	0.5	10	37	Min.	2.0	Neutralizer flow rate
37	↓	↓	↓	↓	↓	Nom.	↓	
38	↓	↓	↓	↓	↓	>>Nom.	↓	
39	↓	1.0	↓	↓	↓	Min.	↓	
40	↓	↓	↓	↓	↓	Nom.	↓	
41	↓	↓	↓	↓	↓	>>Nom.	↓	

FOLDED FRAME /

Table 3B. Thruster Operating Parameters During  
Beam Efflux Measurements.

	Data Points	Screen voltage (kV)	Beam current (A)	Accel voltage (kV)	Emission current (A)	Discharge voltage (V)	Date	Tank pressure ( $\mu$ Torr)	Prop. utiliz. eff.
	1	1.1	1.94	0.55	12.0	37	10/29	4.5	102
	2	1.1	1.90	0.55	10.0	39	10/30	5.0	90
	3								
Beam current	4	1.1	1.5	0.55	9.0	37	9/15,9/25	3.8,5.7	94,96
and propellant	5	1.1	1.46	0.50,0.55	7.5	38	10/30,11/21	3.5,3.9	74,78
utilization	6	1.1	1.40	0.55	7.0	39	10/28	4.8	82
efficiency	7	1.1	1.0	0.55	6.0	39	9/10,9/11	3.6,6.3	84,86
	8	1.1	0.95	0.55	5.0	37	9/17	3.4	80
	9	1.1	0.91,0.94	0.55	4.5	37,39	9/17,11/21	2.6,5.8	62,79
	10	1.1	0.52	0.55	3.0	37	9/18	3.0	80
	11	1.1	0.50	0.55	2.5	39	10/1	4.2	66
	12	1.1	0.45	0.55	2.0	39	10/27	3.7	54
	13								
at ion	14	1.1	1.90	0.55	10.0	39	10/30	5.0	90
energy	15	0.7	1.72	0.50	10.0	39	11/19	3.0	84
	16	1.5	0.97	0.50	5.0	39	11/4	3.0	84
	17	1.1	0.95	0.55	5.0	37	9/17	3.4	80
	18	0.7	0.95	0.50	5.0	40	11/5	2.8	76
	19	1.1	1.78	0.30	10.0	38	11/20	3.6	79
Accelerator	20	1.1	1.90	0.55	10.0	39	10/30	5.0	90
voltage	21								
	22	1.1	0.94,0.97	0.10	5.0	39,40	11/5,11/12	1.8,3.4	74
	23	1.1	0.96	0.50	5.0	39	11/11	4.8	84
	24	1.1	0.97	0.70	5.0	39	11/13	3.2	87
	25								
Discharge	26	1.1	1.90	0.55	10.0	39	10/30	5.0	90
voltage	27								
	28	1.1	0.95	0.50	4.3	43	11/13,11/17	2.8	72,100
	29	1.1	0.95	0.55	5.0	37	9/17	3.4	80
	30	1.1	0.96	0.50	5.6	34	11/18	2.8	81
	31								
Neutralizer	32	1.1	1.90	0.55	10.0	39	10/30	5.0	90
oper	33								
current	34								
	35	1.1	0.95	0.55	5.0	37	9/17	3.4	80
	36								
Neutralizer	37	1.1	1.90	0.55	10.0	39	10/30	5.0	90
flow rate	38								
	39	1.1	1.0	0.550	6.0	37	8/14	3.8	*V <sub>k</sub> =17.0V
	40	1.1	1.0	0.550	6.0	37	8/14	3.5	*V <sub>k</sub> =13.6V
	41								

\*(neutralizer operation condition altered via tip heater)

FOLDOUT FRAME

Figures 14 and 15 illustrate 4"  $J_+$  current as a function of  $z$  for all ions, for soft ions (energy less than 25 eV) and for hard ions (energy greater than 95 eV) as thruster screen potential is varied from 1.5 kV to 0.7 kV, all other thruster voltages held fixed. Three features in the data given there are of interest. The first of these is that the Group IV ion flux is virtually unaffected for this screen voltage variation (and consequent decel-accel variation). This non-sensitivity of the Group IV flux will be shown (in Section 5) to be a reasonable consequence of expected trajectories for these slow ions. The second feature of interest is the observed increase in high energy, high angle of divergence ions as the decel-accel ratio is increased. This feature will be examined further in Section 6. The third feature of (general) interest is the relative magnitudes of hard and soft ion fluxes for  $z > \sim 10$  centimeters. Sections 4.1 and 4.3 have discussed the problems of retarding potential analyses to determine low energy ion flux in the presence of large quantities of high energy flux (see also Figure 12) and Figures 14 and 15 illustrate the regions for which these low signal-to-noise conditions are obtained.

Figures 16 and 17 illustrate 4"  $J_+$  data, separated into low and high energy ions, for engine operation points 2 and 19, for which the accelerator grid potential is set at -550 volts and at  $\sim -300$  volts (a minimum value required to prevent electron backstreaming). The slow ion Group IV flux again demonstrates its lack of sensitivity to changes in thruster operation. A major change is experienced, however, in the high energy high angle flux which has significant implications in terms of the use of Group IV as a thruster diagnostic (see also Section 8.0). In Figures 18, 19, 20, these data runs are repeated, except for a now lowered (1 ampere) thruster current. Again, slow ion flux is relatively invariant to changes in the decel-accel ratio, and, for minimum decel, there are significant diminutions in the high energy high angle flux. (Figure 18, Engine Operation Point 22).

#### 4.6 Slow Ion Behavior as a Function of Discharge Potential

The Group IV flux was also examined as a function of discharge chamber potential. Figures 21 and 22 illustrate the data for a 1 ampere

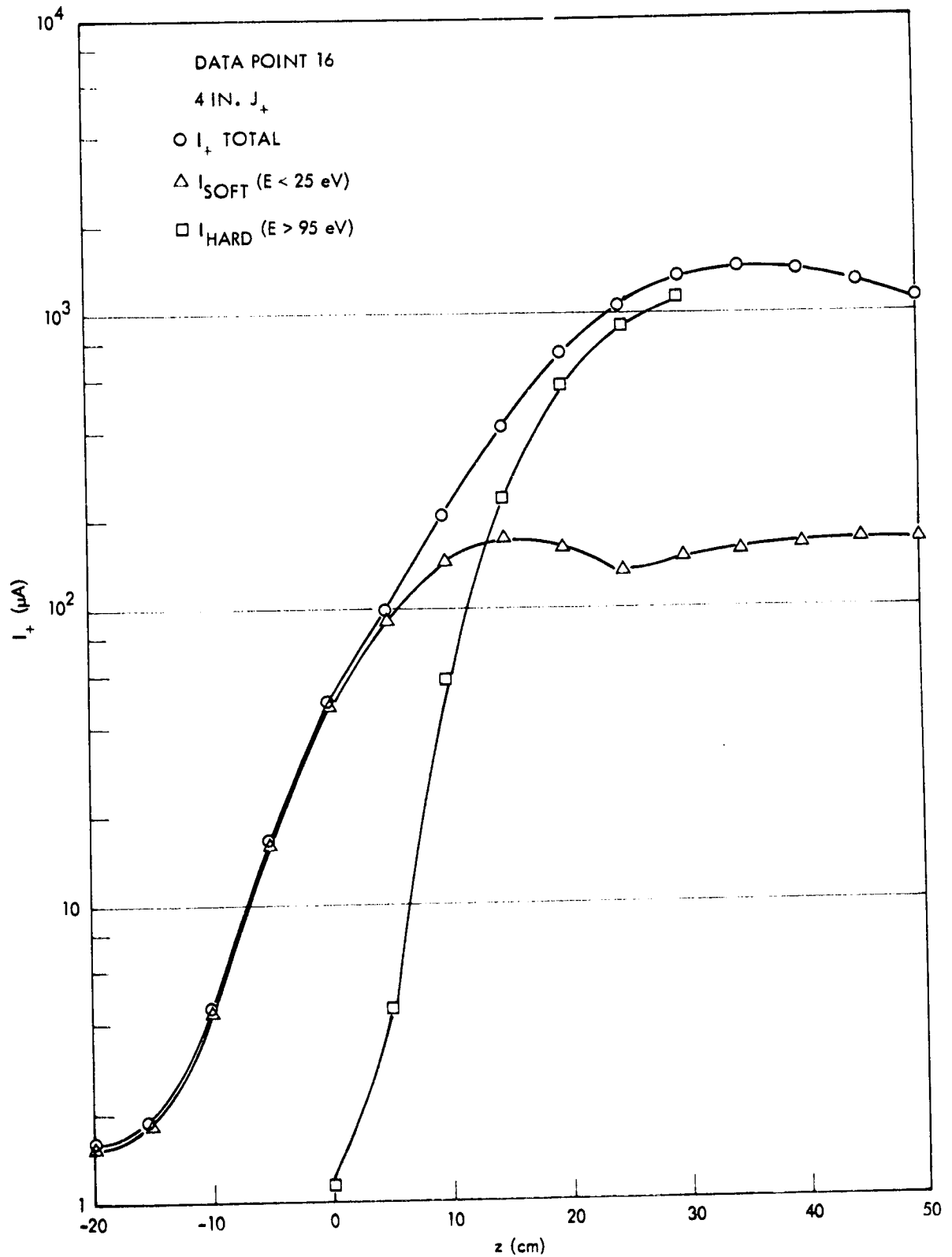


Figure 14. Total Ion Current, and Soft and Hard Ion Current Components in the 4"  $J_+$  Probe as a Function of Axial Distance,  $z$ , for Engine Operation Data Point 16 ( $V_s = 1.5$  kV).

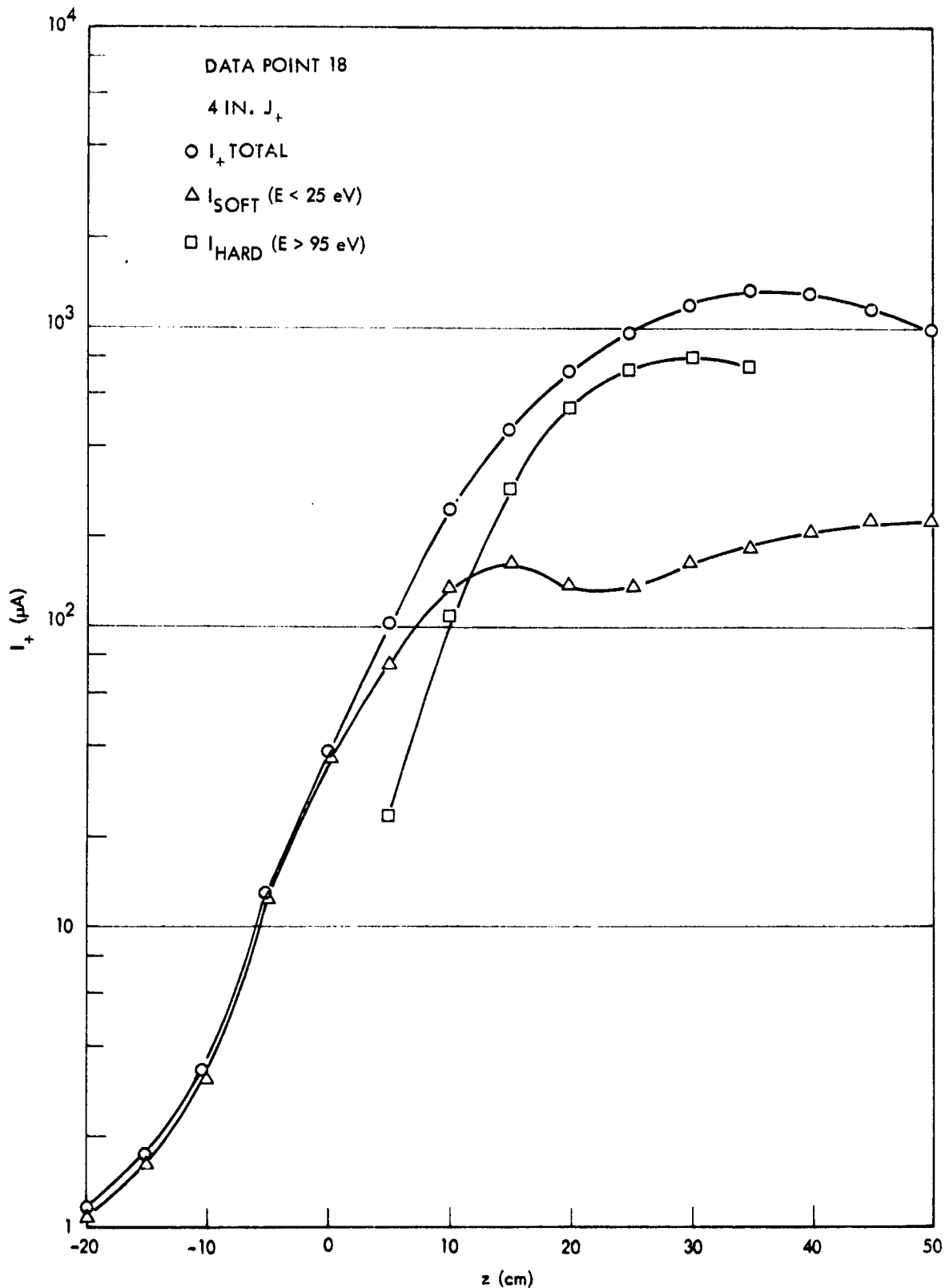


Figure 15. Total Ion Current, and Soft and Hard Ion Current Components in the 4"  $J_+$  Probe as a Function of Axial Distance,  $z$ , for Engine Operation Data Point 18 ( $V_s = 0.7$  kV).

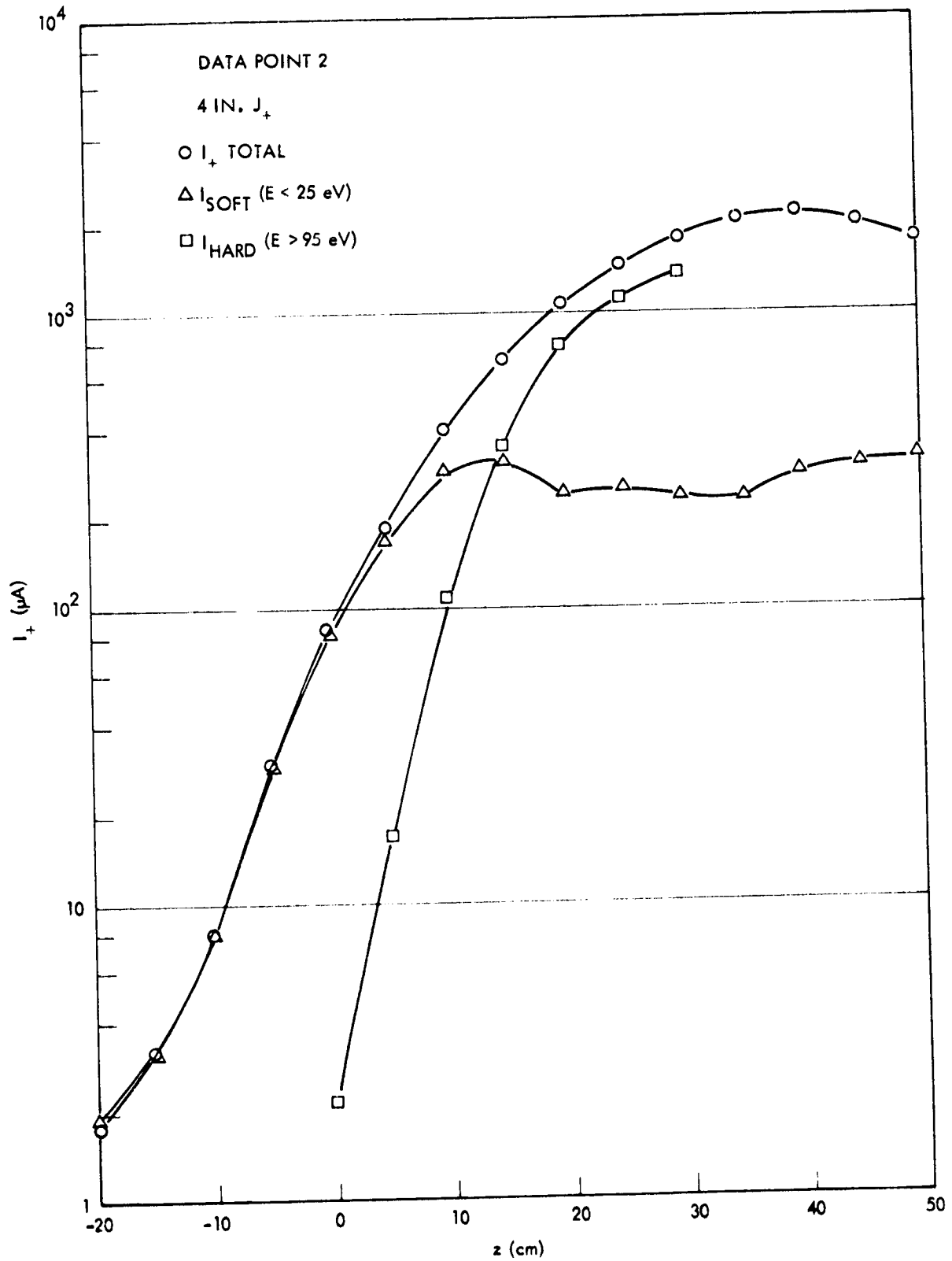


Figure 16. Total Ion Current, and Soft and Hard Ion Current Components in the 4"  $J_+$  Probe as a Function of Axial Distance,  $z$ , for Engine Operation Data Point 2 ( $V_g = -.55$  kV).

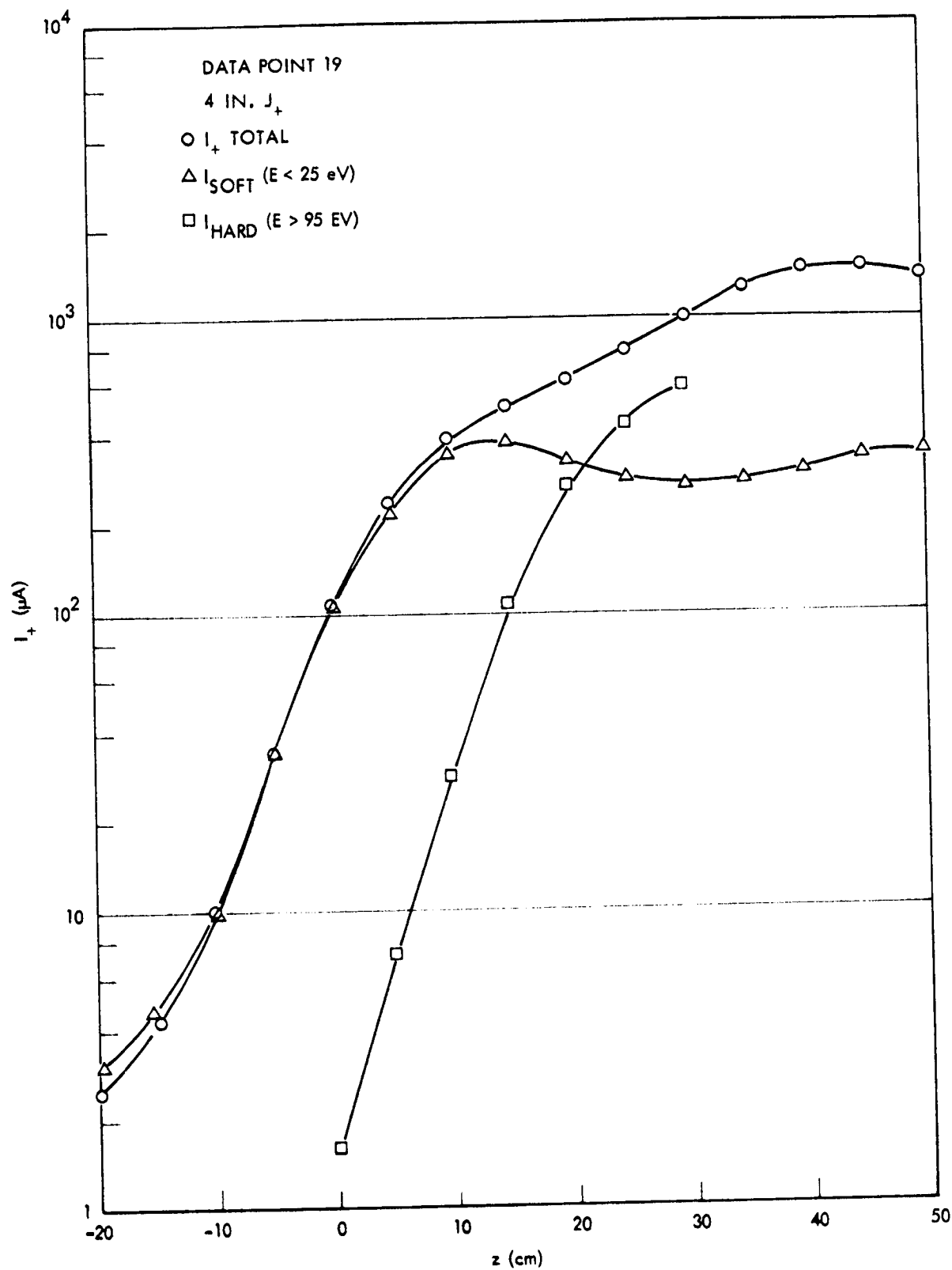


Figure 17. Total Ion Current, and Soft and Hard Ion Current Components in the 4"  $J_+$  Probe as a Function of Axial Distance,  $z$ , for Engine Operation Data Point 19 ( $V_g = -.3$  kV).

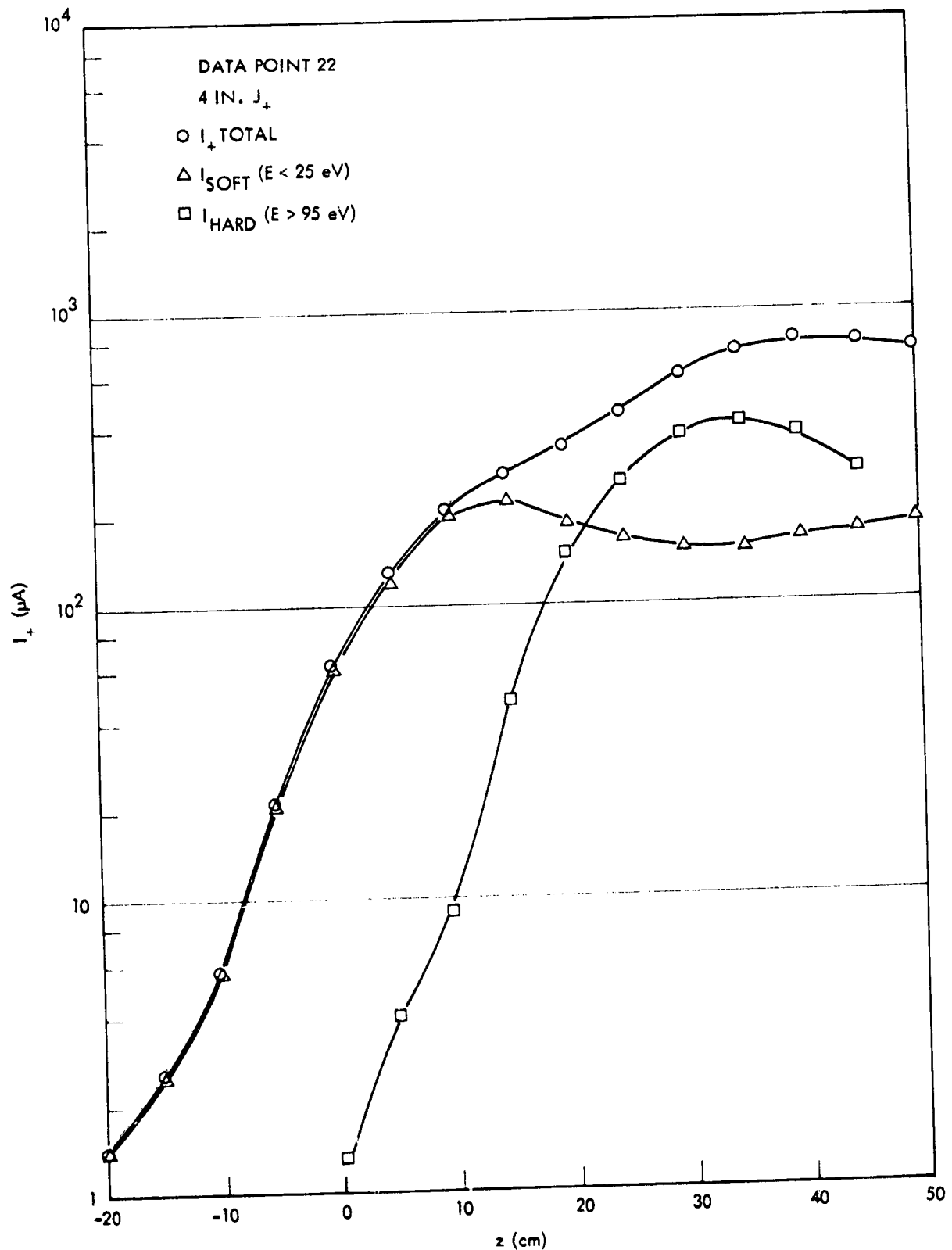


Figure 18. Total Ion Current, and Soft and Hard Ion Current Components in the 4"  $J_+$  Probe as a Function of Axial Distance,  $z$ , for Engine Operation Data Point 22 ( $V_g = -.1$  kV).

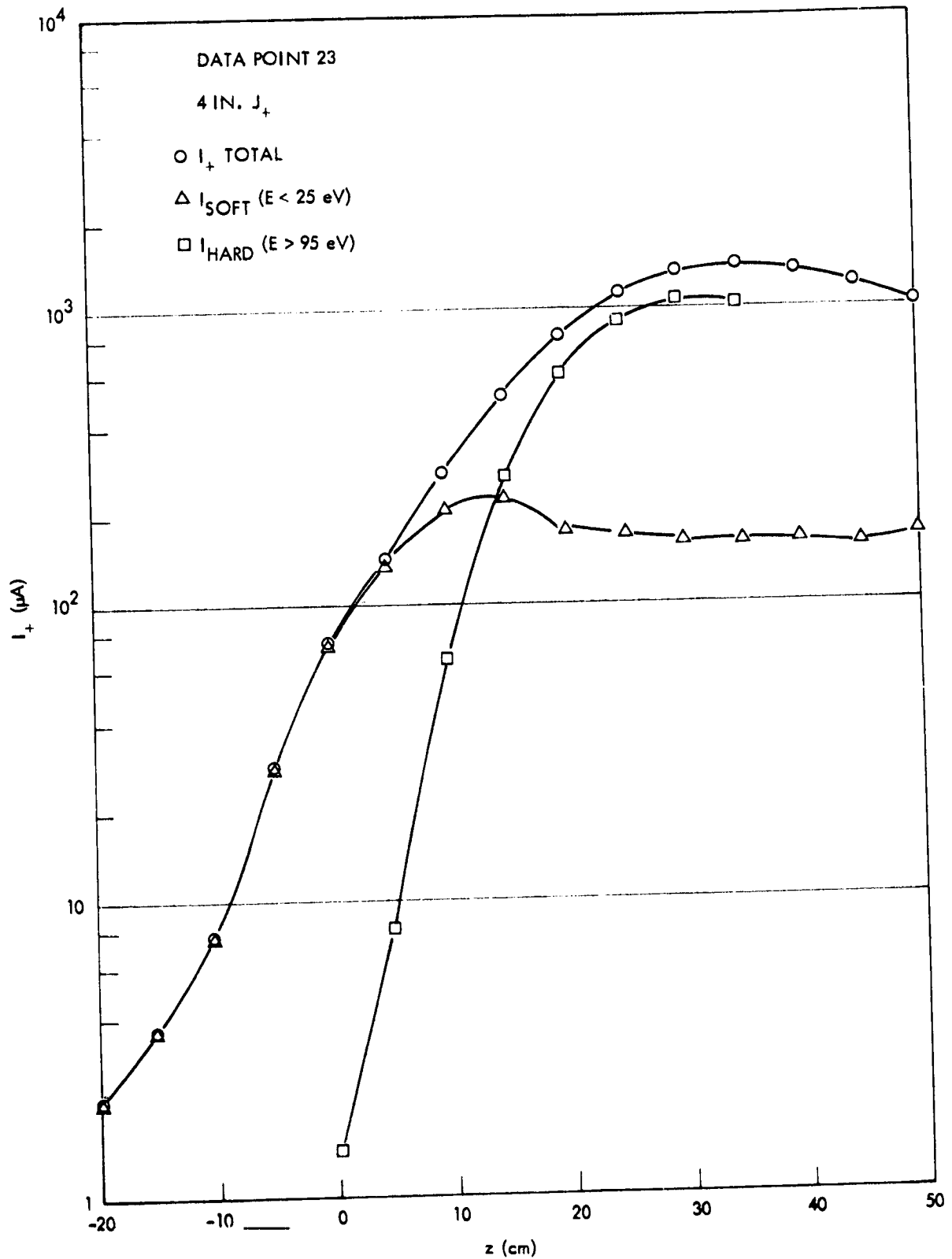


Figure 19. Total Ion Current, and Soft and Hard Ion Current Components in the 4"  $J_+$  Probe as a Function of Axial Distance,  $z$ , for Engine Operation Data Point 23 ( $V_g = -0.5$  kV).

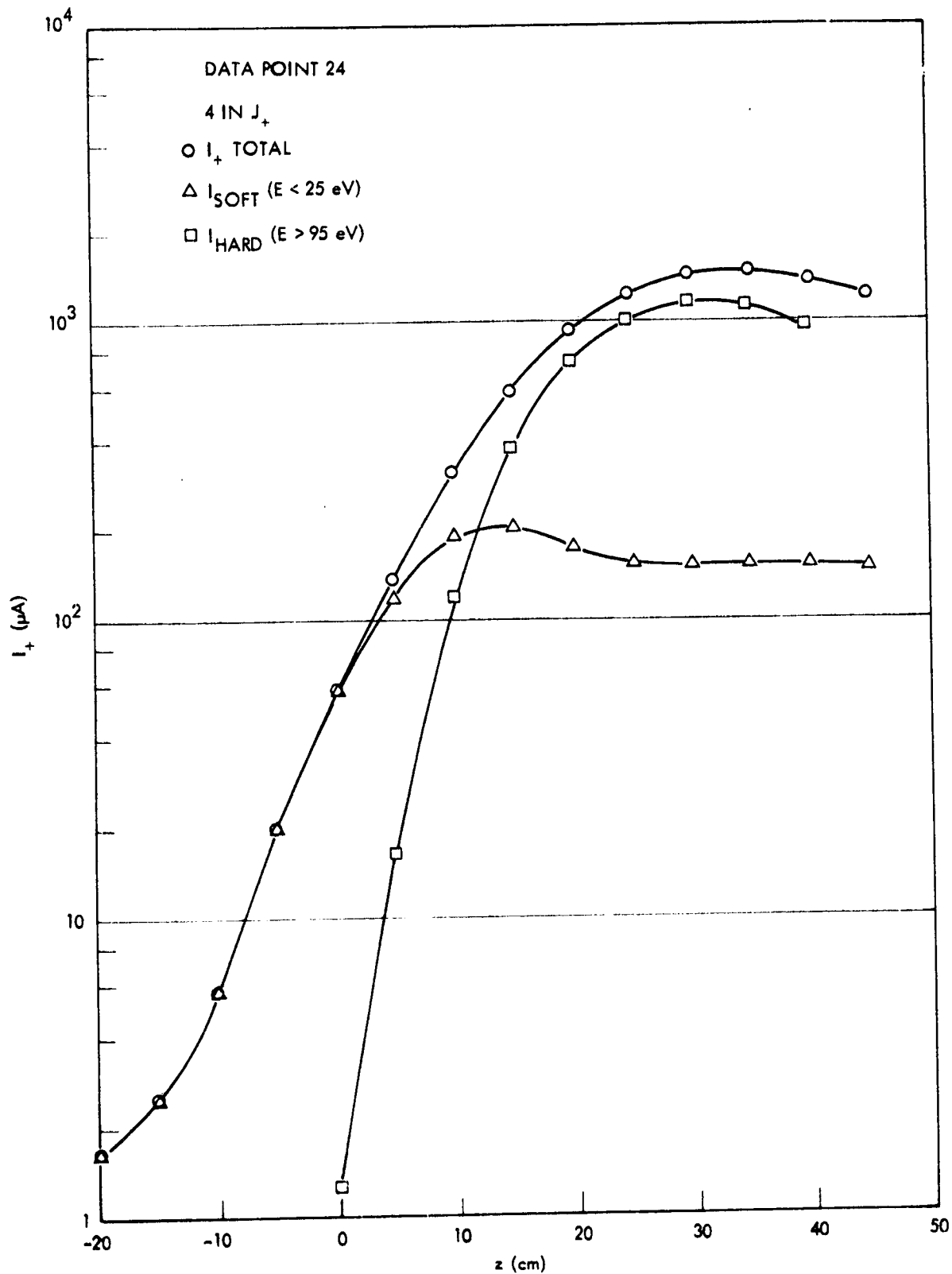


Figure 20. Total Ion Current, and Soft and Hard Ion Current Components in the 4" J<sub>+</sub> Probe as a Function of Axial Distance, z, for Engine Operation Data Point 24 (V<sub>g</sub> = -.7 kV).

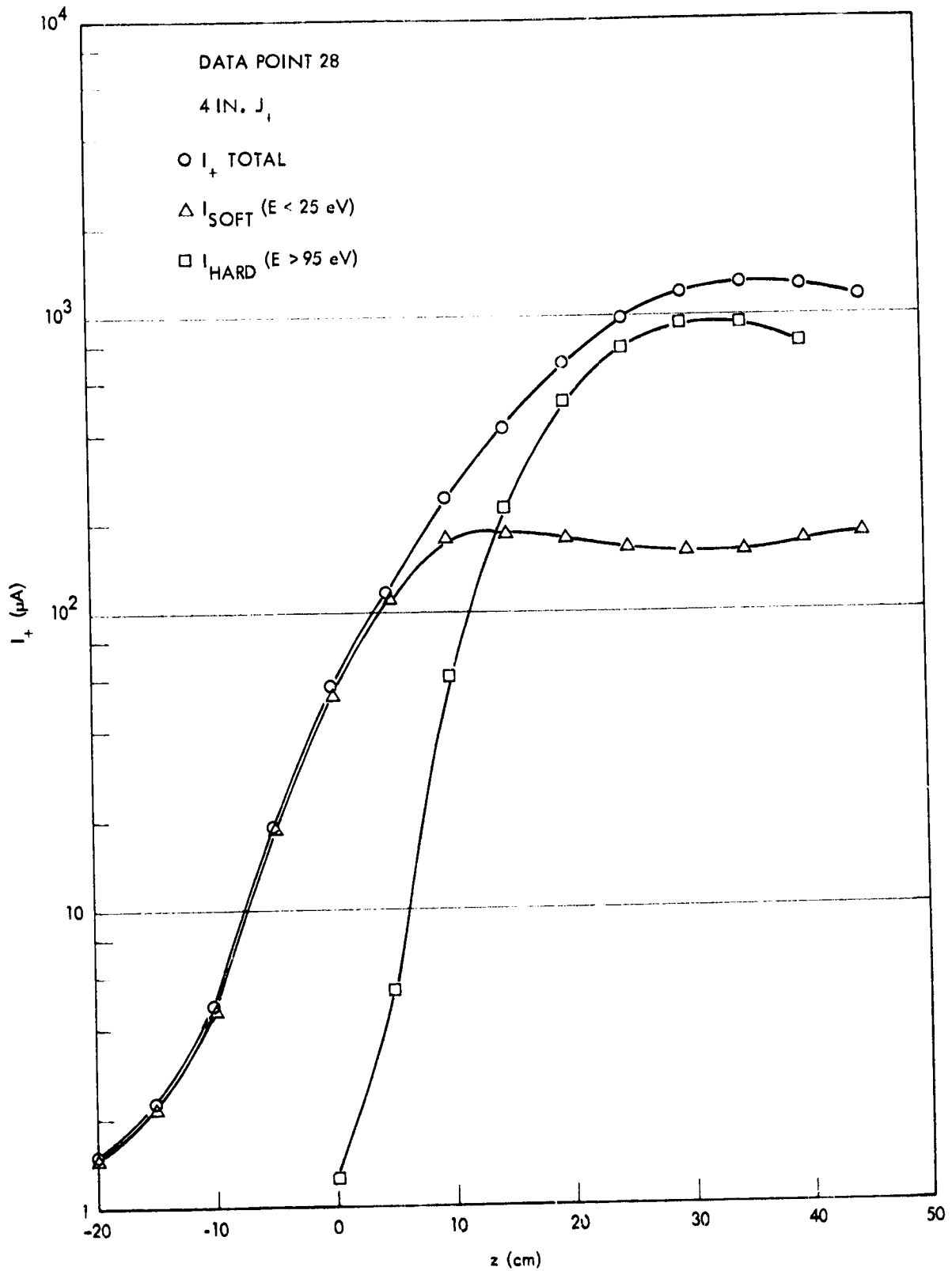


Figure 21. Total Ion Current and Soft and Hard Ion Current Components in the 4"  $J_+$  Probe as a Function of Axial Distance,  $z$ , for Engine Operation Data Point 28 ( $V_{ANODE} = 43$  V).

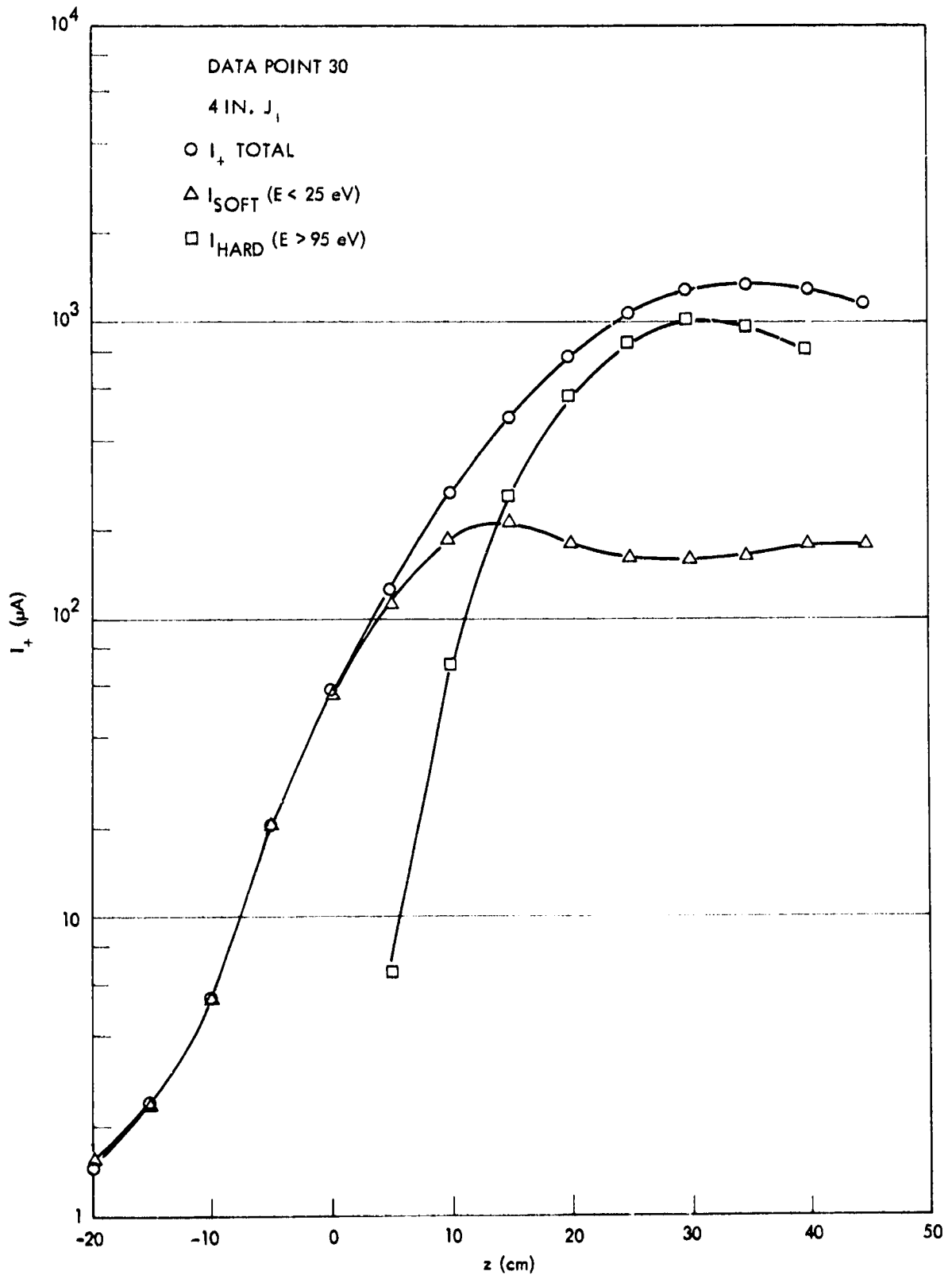


Figure 22. Total Ion Current and Soft and Hard Ion Current Components in the 4"  $J_+$  Probe as a Function of Axial Distance,  $z$ , for Engine Operation Data Point 30 ( $V_{ANODE} = 34$  V).

thrust beam as discharge potential was varied from 43 to 34 volts (engine operation points 28 and 30 in Table 3) at constant discharge power. The results in Figures 21 and 22 demonstrate that the hard ion flux is essentially invariant to these thruster changes, and, that the low-energy ion flux is similarly unchanged. This behavior will be considered as logical in view of expected slow ion trajectory modeling (Section 5).

#### 4.7 Slow Ion Behavior as a Function of Neutralizer Operation Condition

The engine operation point data in Table 3 indicate variations in neutralizer conditions and the thruster plume was examined for two conditions of neutralizer keeper potential. In the first condition, neutralizer keeper was held at 13.6 volts. In the second condition the neutralizer tip heater power was reduced somewhat leading to a keeper potential of 17.0 volts. The 4"  $J_+$  probe data for all ions and for hard and soft ion currents is given in Figure 23 for the two keeper potential conditions. As shown there, neither the hard nor the soft ion flux patterns are significantly affected by this variation in neutralizer operation condition.

In separate experiments and using the Engine  $J_+$  as a floating probe, evidence was obtained that, although the potential in the thrust beam did move upward as neutralizer heat rate was decreased, this potential increase did not lead to an observable increase in thrust beam neutralizing electron temperature. Since  $T_e$  did not vary significantly and since the thrust beam plasma density and density gradients were not affected by this variation in neutralizer operation, there is no expected basis for soft ion trajectory variation, and the data in Figure 23 confirms these expectations. This insensitivity in the Group IV flux to neutralizer operation is not expected to continue to be obtained, however, if severe cutback of neutralizer heat occurs leading to a modal change in neutralizer operation and significant increases in thrust beam neutralizing electron temperature.

#### 4.8 Slow Ion Behavior as a Function of Collector Surface Material

The discussion in Section 3 considered several forms of ambient chamber particles and it could be considered possible that the species and fluxes of these ambient gases would vary as the collector surface

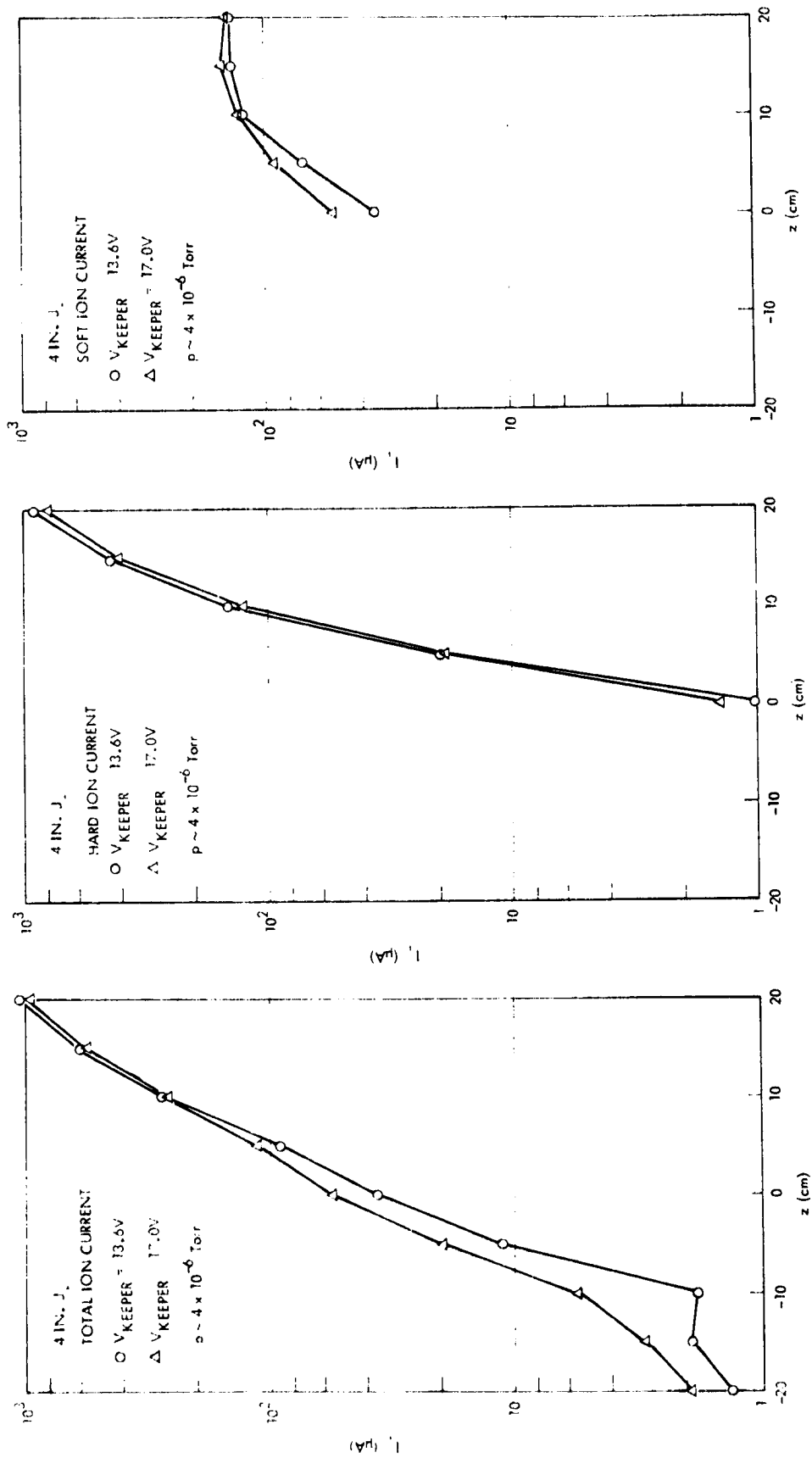


Figure 23. Total Ion Current and Soft and Hard Ion Current Components in the 4" J<sub>+</sub> Probe as a Function of Axial Distance, z, for Two Neutralizer Keeper Voltages.

material is varied. Although these possibilities were not pursued in detail, two conditions of collector surface were used in the beam measurements program. The first of these was a bare titanium collector (used here and in all other data points with the single exception of these experiments) and a low sputter yield graphite sprayed collector.

The probe used in the ion flux measurements here was the Piggyback  $J_+$ , since this probe looks directly at the collector surface and could be expected to respond more sensitively than any other probe to changes in the collector surface. Figure 24 illustrates Piggyback  $J_+$  current for the two surface conditions. Although the ion gauge readings of chamber pressure were essentially the same for the two collector conditions, a significantly higher ion flux in the backward direction was obtained with the low sputter yield surface, compared to bare titanium. There is no immediate explanation for this observed behavior. As noted earlier, all other data runs were obtained with the bare titanium collector, whose use considerably simplified chamber operation during the thruster measurements (no required insertion and refurbishment of special collector surfaces).

#### 4.9 Slow Ion Behavior as a Function of Propellant Utilization

Section 4.4 has discussed slow ion behavior as a function of thrust ion current and has noted that propellant utilization varies as thrust ion current varies, with more efficient utilization of propellant as beam current increases. A statement of slow ion behavior as  $I_{+,t}$  varies, then, may be that the Group IV production has  $I_{+,t}$  as an explicit variable, and propellant utilization as an implicit variable.

It is also of interest to consider Group IV production with propellant utilization as an explicit variable. Such experiments are carried out by holding  $I_{+,t}$  fixed and varying propellant utilization by alterations in the bombardment discharge. In Section 5.2.3, total (measured) Group IV production is examined, and, within a given  $I_{+,t}$  condition, various propellant utilizations were maintained in the various engine runs. A qualitative observation is that Group IV production increases (generally) with diminutions in propellant utilization.

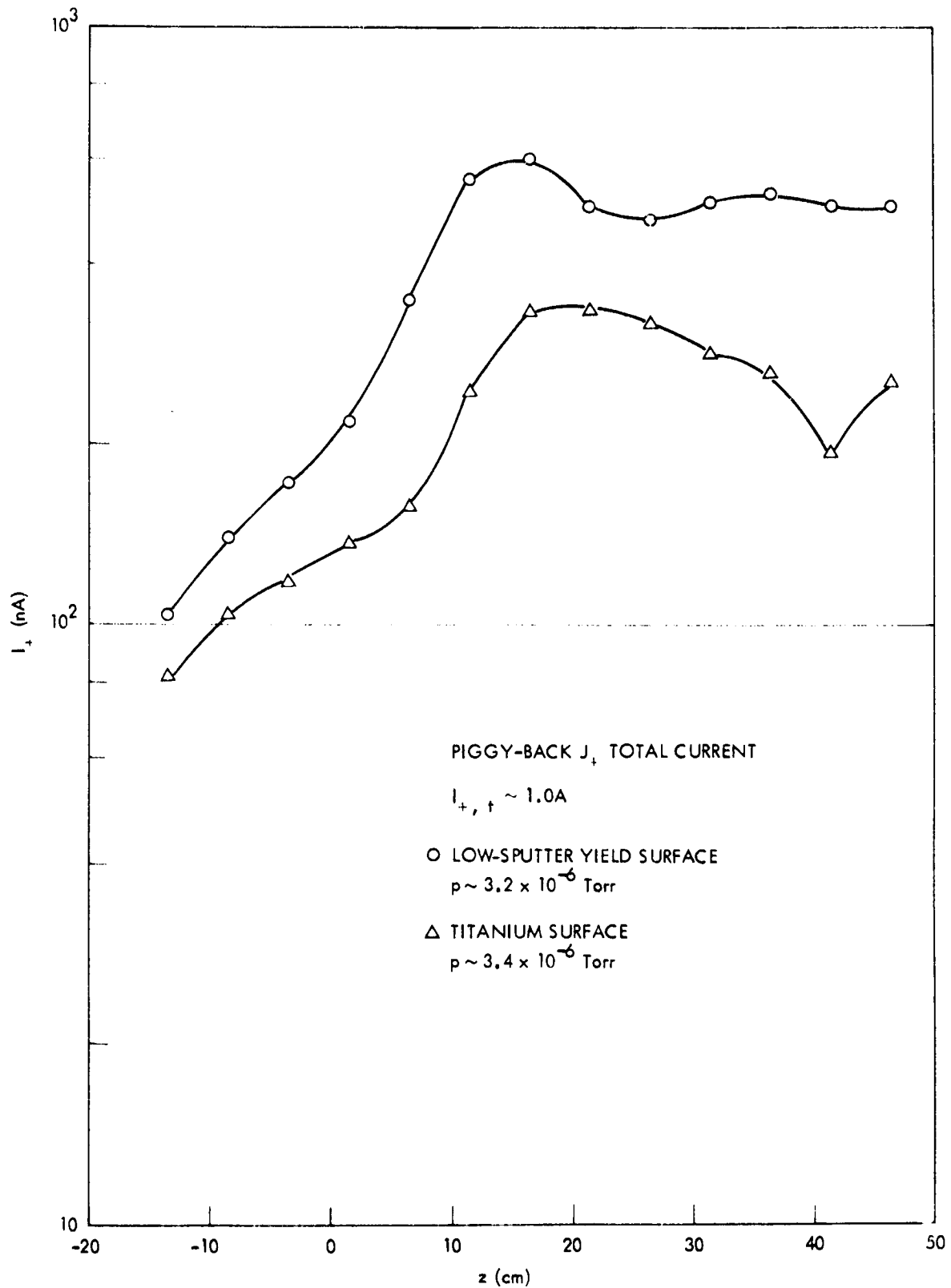


Figure 24. Total Ion Current in the Piggyback  $J_+$  Probe as a Function of Axial Distance,  $z$ , for Two Conditions of Thrust Beam Collector Surface.

## 5.0 LOW ENERGY ION FLUX MODELING

### 5.1 General Considerations

The modeling of the low energy Group IV ion flux in the thruster plume can be carried out, for total charge exchange ion production, for the trajectories of specific ions (following the charge transfer process) and for the flux deposition patterns of all ions. The analyses in this program have emphasized the first two areas above (total production and selected individual trajectories) but have not attempted to derive total flux deposition patterns. Discussion in subsequent sections will detail the reasons (increasing numerical complexity and diminishing levels of certainty in the analytical model for these calculations) that total flux deposition patterns have not been computed. The necessary steps leading to a total flux deposition computation will, however, be discussed.

In addition to computations of genuine Group IV ion production and trajectory, the flux modeling has examined facility effect charge exchange ion production and trajectories for facility effect charge transfer involving either thermal (wall) neutrals or weakly energetic (sputtered) neutrals in the charge exchange.

Some simplifications have been introduced in the model and in the calculations, of necessity. For example, neutral atom emission density from the thruster has been assumed to be uniform over the face of the thruster. Also  $Hg^0$  emission from the neutralizer has been included (in terms of overall neutral release) but, rather than have this release emitted asymmetrically, the emission has been considered as a portion of the total release from the thruster discharge.

A final point of emphasis here is in the complications caused by multiple thruster beams. These "cluster effects" will include an increased total production (since neutrals escaping from one beam without charge transfer may, in traversing the now adjoining ion beams, engage in such a transfer) and asymmetries in the total Group IV plume (at least within distances comparable to the thruster-to-thruster separation). Section 5.4 which discusses uncertainties in the modeling will also

examine the effects of increased Group IV production, including "pile-up" of these slow ions in the interspace between beams and possible broadening of the divergence cones of these slow ions as a result of slow ion accumulation.

## 5.2 Calculated Group IV Ion Production and Comparison to Observed Ion Flux

### 5.2.1 Calculated Genuine Group IV Production

In this section the total charge exchange ion rate of creation will be determined between a total thrust ion current of  $I_{+,t}$ , in coulombs per second, and a thruster total neutral release,  $F_0$ , in atoms per second. It will be assumed that all ions are  $Hg^+$  and all neutrals are  $Hg^0$ . The volume rate of genuine Group IV ion production, in coulombs per second per cubic centimeter is given by

$$\frac{dn_{+cx}}{dt} = J_{+,t} \sigma_{cx} n_{ne} \quad (6)$$

where  $J_{+,t}$  is thrust ion current density in amperes per square centimeter,  $\sigma_{cx}$  is the ( $Hg^+$ ,  $Hg^0$ ) charge exchange cross section in square centimeters, and  $n_{ne}$  is the density of  $Hg^0$  in atoms per cubic centimeter for  $Hg^0$  released by the ion engine. The total charge exchange creation rate is then given by the integral of Eq. (6) over all space.

In setting the volume integral up for machine integration it has been useful to state the thrust ion and mercury atom density distributions in terms of normalized coordinate distances and certain functional plume shapes. Using a cylindrical coordinate system in which the  $z$  axis is the thrust beam axis and  $r = z = 0$  is the center of the thruster face, the volume integral in Eq. (6) becomes

$$I_{+cx} = \int_0^1 \int_0^{\infty} 2\pi r dr dz (J_{+,t}(r,z) n_{ne}(r,z) \sigma_{cx}) \quad (7)$$

where azimuthal symmetry has been assumed in both the thrust ion plume and in the thruster neutral plume. The coordinates  $r$  and  $z$  will be normalized to the thruster radius,  $b$ , by

$$z = \eta b \quad (8)$$

and

$$r = \eta b \quad (9)$$

For this present experiment, the thruster radius,  $b$ , is 15 centimeters. This radius  $b$  must be distinguished from a second radius term,  $r_{ob}$ , which will be used to denote the "core" radius of the thrust ion plume for the "parabolic core-exponential wing" thrust ion density model to be used here. In general,  $b \neq r_{ob}$ .

The thrust ion density distribution to be used has two principal regions. The first of these is a "parabolic core", and in this region

$$J_{+,t}(r,z) = \frac{2I_+}{3\pi(r_{ob} + k_1 z)^2} \left( 1 - \frac{r^2}{2(r_{ob} + k_1 z)^2} \right) \quad (10)$$

core  
( $r \leq r_{ob} + k_1 z$ )

while in the exponential "wing"

$$J_{+,t}(r,z) = \frac{I_+}{3\pi(r_{ob} + k_1 z)^2} \exp \left\{ -\frac{r - (r_{ob} + k_1 z)}{a_{ob} \left( \frac{r_{ob} + k_1 z}{r_{ob}} \right)} \right\} \quad (11)$$

wing  
( $r \geq r_{ob} + k_1 z$ )

The boundary to the core region at axial distance  $z$  is given by  $r = r_{ob} + k_1 z$  where  $k_1$  is a term used to denote the rapidity of growth in  $r$  of this core region for increasing  $z$ . Another term above,  $a_{ob}$ , is used to match the exponential drop-off density in the wing region. In the modeled calculations of the beam from the 30 cm thruster, the values  $r_{ob} = 10$  cm,  $a_{ob} = 5$  cm and  $k_1 = 0.2$  have been used. This modeled plume has generally good agreement with the observed ion beam from this thruster and grid set. Both  $r_{ob}$  and  $a_{ob}$  are also normalized to thruster radius using

$$r_{ob} = \eta b \quad (12)$$

and

$$a_{ob} = \eta b \quad (13)$$

The final computer model of  $J_{+,t}$  is given by

$$J_{+,t}(r,z) = \frac{2I_+}{3\pi r_{ob}^2} \left\{ \rho(\alpha, \eta, \beta, r, k_1) \right\} \quad (14)$$

where  $\rho$  is a function which produces the core and wing regions of Eqs. (10) and (11).

The neutral plume density is given by

$$n_{ne}(r,z) = \frac{F_o}{\pi b^2 v_{o,th}} \left\{ \gamma(\alpha, \eta) \right\} \quad (15)$$

where  $\gamma(\alpha, \eta)$  is a plume function for neutral release and  $v_{o,th}$  is a thermal atom release velocity. In the neutral plume used for the computer, atom emission density is assumed to be uniform over the thruster face. The emission of a single source point into solid angle  $d\Omega$  at divergence angle  $\theta$  is given by

$$\frac{dn_{ne}}{dt} = k_1 \cos^i \theta \quad (16)$$

In the calculations, three distribution forms ( $\cos \theta$ ,  $\cos^2 \theta$ , and  $\cos^3 \theta$ ) were examined. The bulk of the computations were carried out for the  $\cos \theta$  release above, and the results reviewed here will be for that comparatively "broad" release pattern only. In principle, a more accurate fit to the neutral release might be possible by an expansion in terms of  $\cos \theta$ ,  $\cos^2 \theta$ , and  $\cos^3 \theta$  forms of release but, for present purposes, the simplified neutral plume appears to be adequate. Values of  $k_1$  in Eq. (16) are such that one integral of neutral release over the face of the thruster and over  $2\pi$  solid angle of release directions yields the total neutral release,  $F_o$ , (in atoms per second).

When Eq. (7) is transformed, using Eqs. (8), (9), (14), and (15) the total charge exchange ion formation rate is given by

$$I_{+cx} = \left( \frac{4I_+ F_o b^2}{3\pi r_{ob}^2 v_{o,th}} \right) \int_0^{\pi} \int_0^{2\pi} \sin \theta d\theta d\phi \rho(\alpha, \eta) \gamma(\alpha, \eta) \quad (17)$$

or

$$I_{+cx} = \frac{4I_+ F_o b^2 G}{3\pi r_{ob}^2 v_{o,th}} \quad (18)$$

where  $G$  denotes the total integral in  $n$  and  $\alpha$  of the ion and neutral universal plume shapes.

Values of  $I_{+cx}$  have been computed as functions of the various parameters in Eq. (18). For convenience, the display of these calculations is in terms of propellant utilization rather than  $F_o$ , since the usual description of thruster operation will be in terms of thrust beam current and propellant utilization efficiency. Figure 25 illustrates the expected total charge exchange ion production for  $I_{+,t}$  in the range from 0 to 2 amperes and propellant utilization in the range from 70% to 90%. Other parameters used in the calculations given there are:  $b = 15$  cm,  $r_{ob} = 10$  cm,  $a_{ob} = 5$  cm,  $k_1 = 0.2$ , "cos  $\theta$ " neutrals,  $\sigma_{cx} = 5 \times 10^{-15}$  cm<sup>2</sup>, and  $v_{o,th} = 2 \times 10^4$  cm/sec.

For an ion thruster operating in the .5 to 2 ampere and 70% to 90% propellant utilization range, total charge exchange ion production may vary from  $\sim 1$  to  $\sim 70$  milliamperes. Section 5.2.3 will compare this calculated production rate with observed production rates derived by suitable integrals of the 4"  $J_+$  slow ion signal.

A final aspect of the computations to be considered here is the sensitivity of the integral in Eq. (17) to the form of the neutral distribution. The integral  $G$  has been evaluated for  $\cos \theta$ ,  $\cos^2 \theta$ , and  $\cos^3 \theta$  release models for neutrals at fixed total neutral release with the parabolic core/exponential wing ion beam plume ( $r_{ob} = 10$  cm,  $a_{ob} = 5$  cm,  $k_1 = .2$ ) with the following results:

$\frac{f(\theta)_{ne}}{}$	$G$
$\cos \theta$	0.41
$\cos^2 \theta$	0.46
$\cos^3 \theta$	0.50

As may be seen, the more narrowly distributed distributions lead to somewhat larger charge exchange ion production rates. The variances here, however, are not considered significant in view of other and more basic limitations in the model (specifically in the uniform neutral release flux assumption at the thruster face).

### 5.2.2 Calculated Facility Effect Group IV Production

Calculation of the charge exchange ion production rate between the thrust beam and ambient  $\text{Hg}^{\circ}$  is simplified if the comparatively reasonable assumption is made of a uniform ambient neutral density,  $n_{na}$ . For this condition, the traversal of each axial distance increment,  $dz$ , by a thrust ion beam  $I_{+,t}$  creates

$$\frac{dI_{+cx}}{dz} = I_{+,t} \sigma_{cx} n_{na} \quad (19)$$

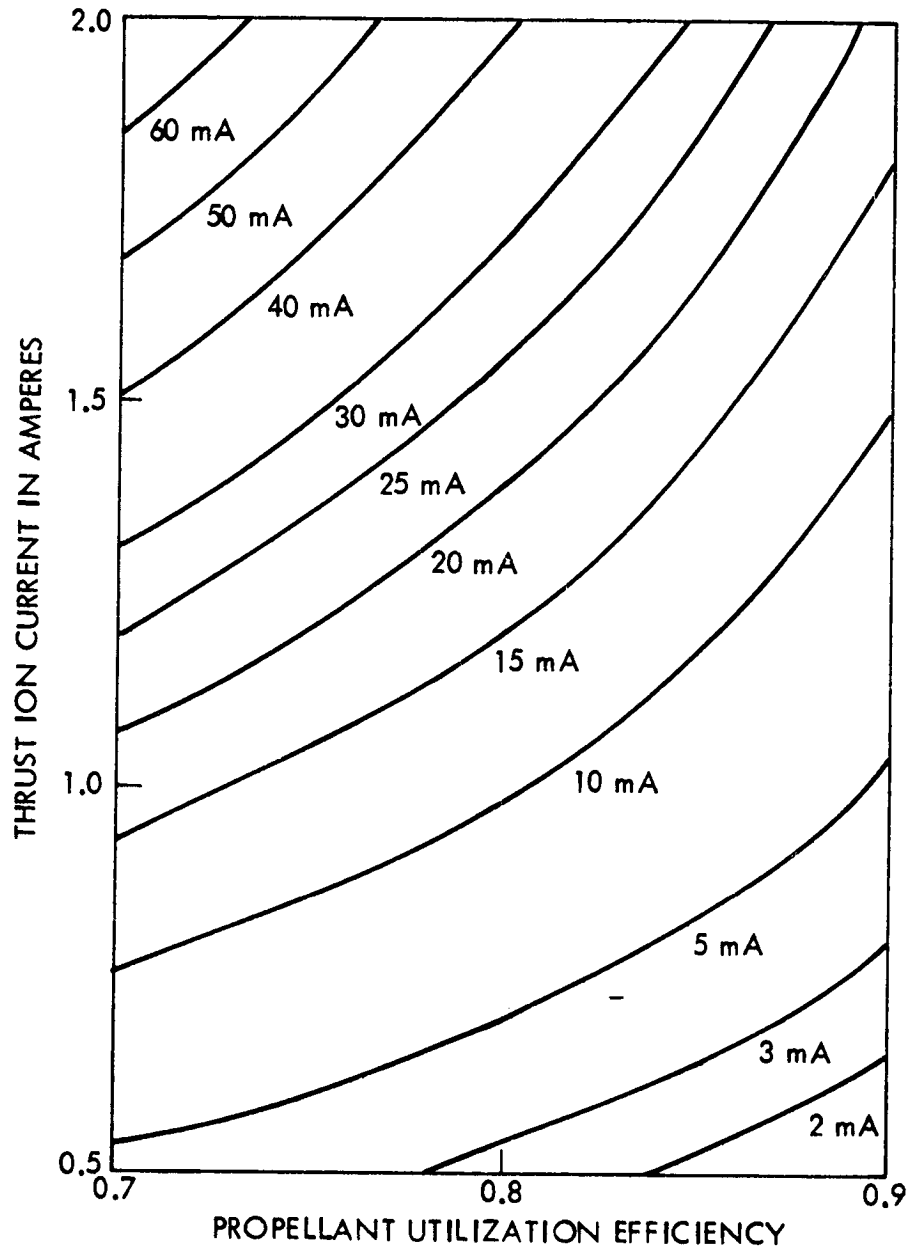
For an ambient  $\text{Hg}^{\circ}$  density in thermal equilibrium with the upstream end of the testing chamber ( $T_{wall} \approx 20^{\circ}\text{C}$ ), an ion gauge reading of  $10^{-6}$  Torr will correspond approximately to an ambient neutral density of  $\approx 3 \times 10^{10}$  atoms per cubic centimeter. Using  $\sigma_{cx} = 5 \times 10^{-15} \text{ cm}^2$  leads to

$$\frac{dI_{+cx}}{dz} \approx 1.5 \times 10^{-4} I_{+,t} / \mu\text{Torr Hg}^{\circ} \quad (20)$$

where, it should be emphasized, the only neutral density of significance is that of  $\text{Hg}^{\circ}$  (because of reduced charge exchange cross sections for other, non-resonant, transfers). It should also be emphasized, again, that the ion gauge responds to all chamber gases and that the partial pressure of mercury in these experiments is not known.

From Eq. (20) it may be seen that  $\text{Hg}^+$  charge exchange ions are produced at  $\approx 150$  nampères per centimeter per ampère of  $\text{Hg}^+$  thrust ion current per  $\mu\text{Torr}$  of  $\text{Hg}^{\circ}$  ambient density. For the region from  $z = 0$  to  $z = 50$  centimeters this would yield  $\approx 7.5$  milliamperes of  $\text{Hg}^+$  charge exchange per ampère of  $\text{Hg}^+$  thrust ion current per  $\mu\text{Torr}$  of  $\text{Hg}^{\circ}$  ambient density. The ion gauge readings during the beam measurements were in the range from 2.5 to 5 Torr, some fraction of which is not  $\text{Hg}^{\circ}$ . For  $\text{Hg}^{\circ}$  densities ranging from 1 to 3  $\mu\text{Torr}$ , the expected production of  $\text{Hg}^+$  charge exchange current in the  $0 \leq z \leq 50$  cm interval would range from 7 to 23 milliamperes for each ampère of  $\text{Hg}^+$  thrust ion current.

The facility effect  $\text{Hg}^+$  charge exchange ions may be compared to the calculated genuine Group IV in Figure 25, and may be seen to be



(PARABOLIC CORE - EXPONENTIAL WING IONS;  
 $r_{ob} = 10 \text{ cm}$ ;  $a_{ob} = 5 \text{ cm}$ ;  $k_1 = .2$ )

Figure 25. Computed Total  $\text{Hg}^+$  Charge Exchange Current Formation as a Function of Thrust Beam Current and Propellant Utilization. Ion Beam is Parabolic Core/Exponential Wing and Neutral Emission is Uniform Over Thruster Face and  $\cos \theta$  Angular Distribution.

comparable in magnitude. This would tend to indicate, in turn, a comparatively low signal-to-noise ratio in the determination of the genuine charge exchange ions. There is, however, some expected relief through concentration on measurements of Group IV ions in specific axial intervals. Section 4.3 in discussing the characteristic shape of the charge exchange current as seen by the 4"  $J_+$  identified three regions (see also Figure 12) with Regions I and III having a greater dependence on ambient effects while Region II is comparatively well determined by the presence of genuine charge exchange ions.

As another aid to assessing comparative magnitudes of facility effect and genuine charge exchange currents, the fraction of all genuine Group IV ions created in the axial distance interval from 0 to  $z$  has been calculated. Figure 26 illustrates the value of the volume integral in Eq. (17) from 0 to  $\alpha$  ( $z = \alpha b$ , where  $b$  is thruster radius) compared to the volume integral from 0 to  $\infty$ . It may be seen that 60% of the genuine charge exchange production occurs within the interval from  $z = 0$  to  $z = b$  (= 15 centimeters) and that some 78% of the genuine production occurs in the interval from  $z = 0$  to  $z = 2b$  (30 cm). By concentrating the measurements on axial regions near the thruster, good signal to noise conditions can be obtained. For measurements away from these regions (and as discussed in Section 3.1) the effects of facility presence are more dominant.

Another means of viewing the importance of various regions in the chamber is the calculation of the boundary along which the density of ambient  $Hg^\circ$  is equal to the density of  $Hg^\circ$  escaping from the thruster. Figure 27 illustrates the boundary in  $z/b$  and  $r/b$  for which  $n_{ne} = n_{na}$  for an ambient density of  $3 \times 10^{10}$   $Hg^\circ$  per cubic centimeter and for an equivalent  $Hg^\circ$  release of  $\sim 280$  milliamperes (a propellant utilization of 0.78 at 1 ampere of  $Hg^+$  thrust current, and 0.88 at 2 amperes of thrust ion current) of "cos  $\theta$ " neutrals at 500°K. Along the indicated boundary the production rates of genuine charge exchange and facility effect charge exchange are equal, and, within the boundary, genuine effects predominate, increasingly so for regions nearer and nearer the thruster face.

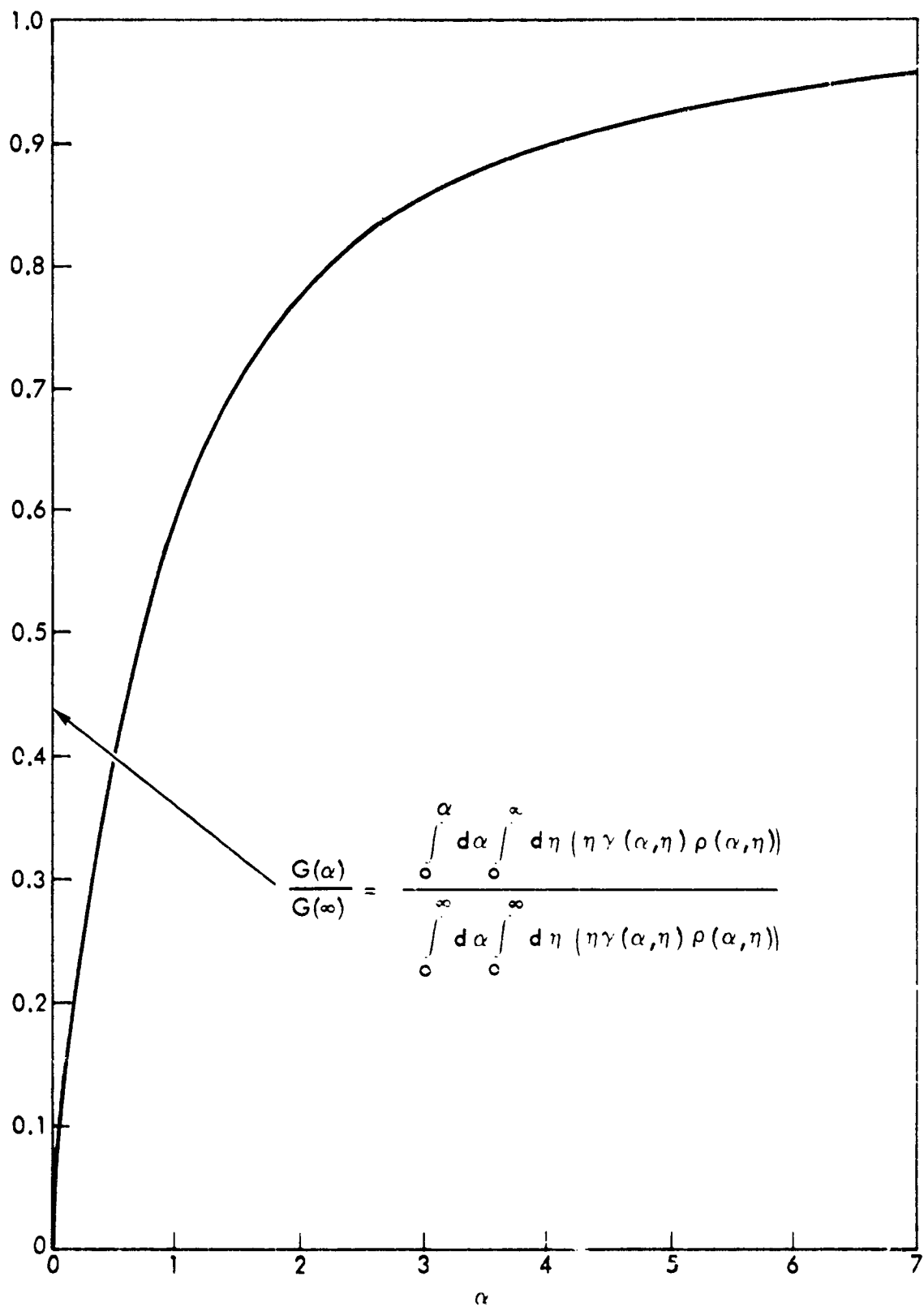


Figure 26. Fraction of Charge Exchange Ion Formation in Axial Distance Interval from  $z = 0$  to  $z = ab$ , Compared to Total  $Hg^+$  Charge Exchange Ion Formation.

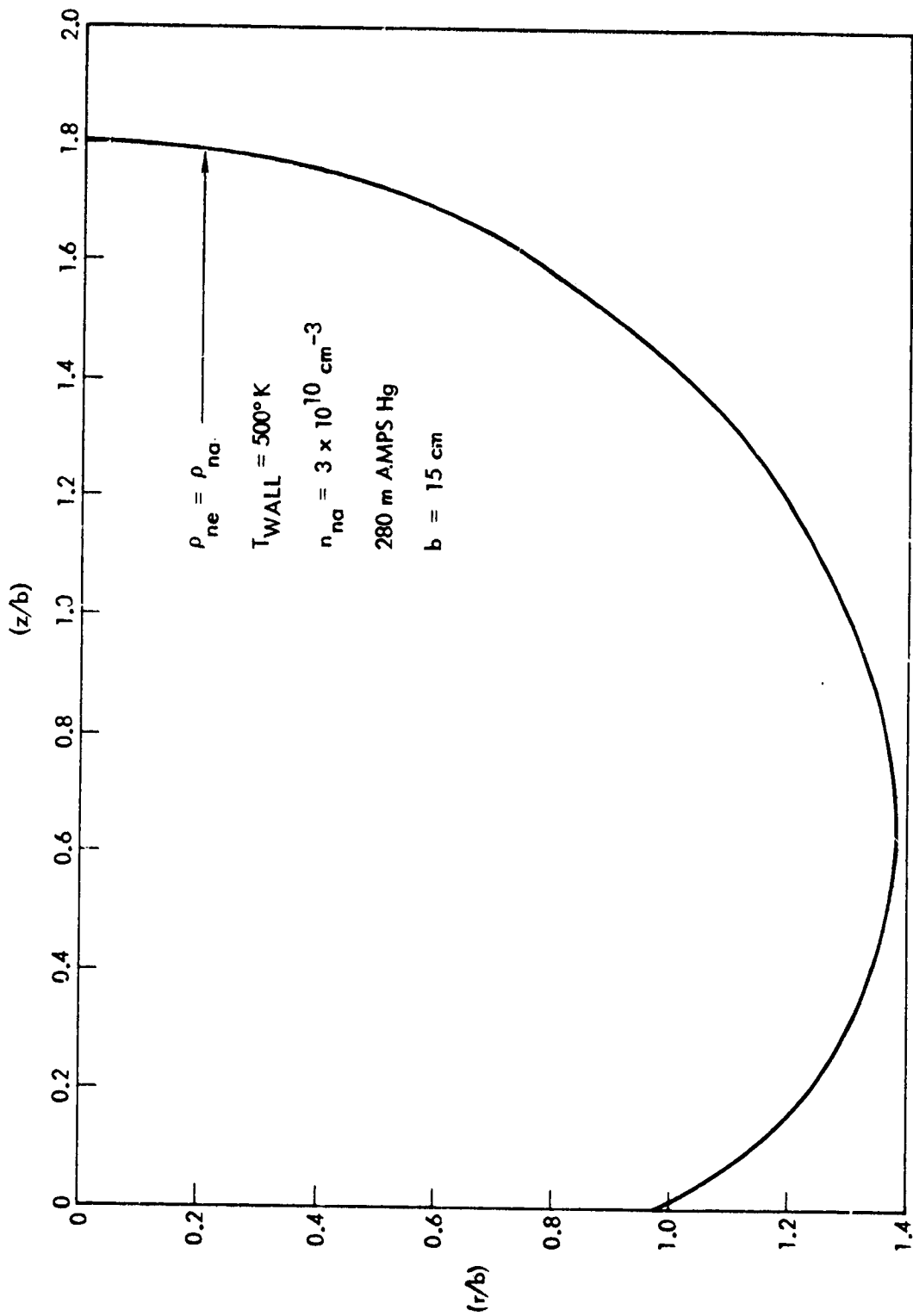


Figure 27. Computed Boundary for Which  $Hg^\circ$  from Ion Thruster has Equal Density with  $Hg^\circ$  in Testing Chamber, (for 280 Milliamperes Equivalent  $Hg^\circ$  Emission from Thruster, "Cos  $\theta$ " Emission Uniform over Thruster Face, Thruster Temperature of  $500^\circ K$  and  $1 \mu\text{Torr } Hg^\circ$  Ambient Chamber Pressure).

A final aspect in the comparison of genuine to facility effect ions to be noted here is that volume rates of production and deposition patterns of these ions are linked by comparatively complicated ion trajectory factors which are not the same for the two forms of production. These trajectories will be discussed further in Section 5.3. The use of the variances in trajectories can improve signal-to-noise ratios in the measurements by selecting certain positions for measurement, as in Region II of the 4"  $J_+$  probe movement.

### 5.2.3 Comparison of Observed Group IV Ions to Calculated Production Rates

The charge exchange ions produced by ( $Hg^+$ ,  $Hg^0$ ) charge transfer will move both radially and axially. If their movement is predominantly radial (and Section 5.3 will demonstrate this predominant direction of motion), the ions should be capable of a straightforward measurement by the 4"  $J_+$  probe. The integral of the current density of Group IV ions seen by the 4"  $J_+$  probe over an appropriate range in  $z$  (and assuming azimuthal symmetry in the Group IV flux) would then provide a measurement of both genuine and facility effect Group IV ions. Table 4 contains values of  $\int_0^{50} 2\pi r_p dz J_+$  for a series of measurement conditions. The measured production given there may be compared to calculated production (Figure 25) and estimated facility effect production (Eq. 20). Consider, for example, the data obtained at Engine Operation Point 12, an ion thrust beam of 0.5 ampere. From Table 4, the value of  $\int 2\pi r_p dz J_+$  from 0 to 50 cm in  $z$  is 14.1 milliamperes. From Eq. (20) and for an assumed level of 2  $\mu$ Torr of  $Hg^0$  ambient pressure, the expected facility production of  $Hg^+$  charge exchange is  $\sim 7.5$  milliamperes in the range from 0 to 50 cm in  $z$ . This would tend to indicate a genuine production of  $Hg^+$  of  $\sim 6.6$  milliamperes. From the relationships in Figure 25 it may be seen that an 0.43 ampere thrust beam from a thruster operating at  $\sim 52\%$  propellant utilization efficiency could produce this indicated level of genuine charge exchange ions. There is, thus, a qualitative agreement between observed charge exchange production (from all sources) and expected production from genuine causes and from facility effects.

While the above comparisons are comforting in terms of signal-to-noise ratios for ions over the total  $0 < z < 50$  cm interval, it should

Table 4A. Engine Operation Data Point with Thrust Ion Current, Propellant Utilization, and Calculated Total Genuine Charge Exchange Ion Current from Model.

Engine Operation Data Point	Thrust Ion Current, $I_{+,t}$ (A)	Propellant Utilization	Genuine Charge Exchange Current (in Milliampères) Computed from Model	Total Charge Exchange Current (in Milliampères) Computed from $4'' J_+$ Signal and $\int_0^{50} 2\pi r dz J_{+,soft}$	Inferred Charge Exchange Ion Current (in Milliampères) from Facility $Hg^\circ$	Inferred Facility Partial Pressure of $Hg^\circ$ ( $\mu$ Torr)	Ion Gauge Reading of Facility Total Pressure ( $\mu$ Torr)	Inferred Fractional Partial Pressure of $Hg^\circ$
12	.43	.52	6.6	14.1	7.5	2.3	2.7	.86
9	.94	.64	19.2	33.5	14.3	2.0	2.9	.70
16	.97	.83	7.4	23.3	15.8	2.2	3.0	.73
18	.96	.75	11.8	25.5	13.7	1.9	2.4	.80
22	.99	.81	8.9	27.3	18.4	2.5	2.8	.89
23	.99	.79	10.0	28.0	17.9	2.4	4.1	.59
24	.97	.82	8.0	25.1	17.1	2.4	2.7	.87
28	.96	.97	1.1	26.1	25.0	3.5	2.8	>1
30	.96	.79	9.4	26.8	17.3	2.4	2.4	1.0
5	1.45	.78	23.0	41.3	18.3	1.7	3.5	.48
6	1.42	.82	17.1	39.6	22.5	2.1	4.6	.46
1	1.92	>1	--	35.4	--			
2	1.90	.88	19.0	41.4	22.4	1.6	4.4	.36
15	1.74	.88	15.9	50.9	34.9	2.7	2.8	.96
19	1.80	.77	37.3	48.7	11.3	.8	3.4	.25

Also given above is calculated total genuine plus facility measured ion current from  $4'' J_+$  signal and integral 0 to 50 cm in z. Measured total production and calculated genuine production infers the facility effect generation and infers a facility partial pressure of  $Hg^\circ$ . For internal consistency, the  $Hg^\circ$  pressure may be compared to ion gauge reading of total pressure. Internal consistency good on lower range (.5A to 1A) of thrust ion current.

HOLDOUT FRAME

Thrust  
 Calculated  
 Model.

Table 4B. Engine Operation Data Point with Thrust  
 Ion Current Propellant Utilization, and Observed  
 Soft Ion Current in 4" J<sub>+</sub> Cup at z = 20 cm.

Ion Gauge Reading of Facility Total Pressure (μTorr)	Inferred Fractional Partial Pressure of Hg°
2.7	.86
2.9	.70
3.0	.73
2.4	.80
2.8	.89
4.1	.59
2.7	.87
2.8	>1
2.4	1.0
3.5	.48
4.6	.46
4.4	.36
2.8	.96
3.4	.25

Engine Operation Data Point	Facility Total Pressure (μTorr)	Maximum Permissible Soft Ion Energy in 4" J <sub>+</sub> Cup (eV)	Thrust Ion Current, I <sub>+,t</sub> (A)	Bombardment Discharge Emission Current (A)	Propellant Utilization	Soft Ion Current (in μA) in 4" J <sub>+</sub> Cup at z = 20 cm
1	4.5	25	1.94	12.0	>1	200
2	5.0	25	1.90	10.0	.90	250
3						
4	5.7	20	1.50	9.0	.94	180
5	3.9	25	1.46	7.5	.78	270
6	4.8	25	1.40	7.0	.82	260
7	6.3	9	1.00	6.0	.86	150
8						
9	5.8	25	0.94	4.5	.79	240
10	3.0	10	0.52	3.0	.80	46
11	4.2	10	0.50	2.5	.66	78
12	3.7	25	0.45	2.0	.54	86

Measured ion  
 Measured total  
 facility effect  
 For internal  
 reading of  
 (.5A to 1A)

For fixed thrust ion current and varying propellant utilization, genuine charge exchange ion signal should vary as  $n^{-1}(1-n)$  where  $n$  is propellant utilization fraction. Observed results indicate rising production rates for diminishing propellant utilization. Three factors restrict these conclusions to a qualitative statement: 1) the range of propellant utilization variation, within a set  $I_{+,t}$ , is generally not large, 2) inaccuracies exist in propellant utilization measurements (reduced throughput measurement times and (possible) inventory fluctuations), and 3) facility effect variations also occur from one engine run to another. It should be noted, also, that engine operation throughout the experiments maintained generally good utilization (for a given  $I_{+,t}$ ) and that deliberately "spoiled" (greatly lowered) utilization did not occur.

be emphasized again, that certain regions are expected to have a predominance in facility effect currents. Figure 12 has given these regions, and Region III is an expected facility dominated zone. The integral of fluxes in Region III for the Data Point 12 example above also shows a comparatively large fraction of the integral (50%) occurs in the range  $30 < z < 50$  cm. In this region, the observed signal is certainly facility dominated with a low signal-to-noise ratio. In the region from 10 to 25 cm in  $z$ , however, the observed currents are probably genuine for the most part, confirming the earlier estimate that the use of observed  $J_+$  in this range is probably an over estimate of the genuine charge exchange flux by only about 30%.

### 5.3 Charge Exchange Ion Trajectories

#### 5.3.1 Genuine Group IV Ion Trajectories

The procedure for the calculation of charge exchange ion trajectories in the plasma thrust beam internal electric field structure was developed in Reference 3 and Reference 4. In this calculation the potential in the thrust beam is assigned the form

$$V(r,z) = \frac{kT_e}{e} \ln \frac{\rho(r,z)}{\rho_0(0,0)} \quad (21)$$

where  $T_e$  is thrust beam neutralizing electron temperature,  $k$  is Boltzman's constant, and  $e$  is electron charge. For  $kT_e$  expressed in electron volts,  $e$  is assigned the value of unity, and  $V$  is in volts. The plasma density is  $\rho$  (ions/cm<sup>3</sup>) and  $\rho_0$  is thrust beam density at  $r = z = 0$ , which is the maximum density in the parabolic core/exponential wing density model given in Eq. (10) and (11) and the potential at  $r = z = 0$  is assigned the value 0. This "electrostatic" barometric equation has been determined in Reference 10 for plasma thrust beams and found to be generally adequate in radial scans of the potential. There are questions on the adequacy of Eq. (21) for variations in the position of a field point in the axial direction and these will be discussed further in Section 5.4.

From Eq. (21) and the density model in Eq. (10) and (11), variations in potential for movement  $\Delta r$  at  $(r,z)$  and  $\Delta z$  at  $(r,z)$  have been calculated by a computer program. The value of  $\vec{E}_r(r,z)$  and  $\vec{E}_z(r,z)$  are, thus, known at all  $(r,z)$ .

The remaining element in the calculation of charge exchange ion trajectory is a specification of the initial charge exchange speed and direction. For genuine charge exchange ion production, initial ion velocity is the atom velocity prior to charge exchange and is determined by the thruster "wall" temperature, the point of exit of an atom from the thruster and the point  $(r,z)$  at which charge exchange occurs. These three quantities are programmed into the calculation which derives the initial  $\dot{r}$  and  $\dot{z}$  of the charge exchange ion.

The motion of the charge exchange ion is determined by a "marching" method in which particle acceleration from  $\vec{E}_r$  and  $\vec{E}_z$ , and known  $\dot{r}$  and  $\dot{z}$  at the point  $(r,z)$  is used to calculate the  $(r',z')$  and  $(\dot{r}',\dot{z}')$  of the ion after a passage of  $\delta t$  in time. The electric fields at  $(r',z')$  are then calculated and the process iterated, with an accompanying trajectory printout.

Figures 28 through 36 illustrate a series of trajectory plots of these charge exchange ions. Assumptions of thruster wall temperature ( $500^\circ\text{K}$ ) and thrust beam neutralizing electron temperature ( $5000^\circ\text{K}$ ) are stated on the figures. A particular simplifying limitation in these calculated trajectories is that the atom exit point and the charge exchange point occur in the same plane as the thrust beam axis, so that there is no  $\phi$  term and the calculations are only in two dimensions,  $r$  and  $z$ . The neglect of angular momentum is deliberate, and Section 5.4 will discuss the limitations which this restricted case places on total flux deposition patterns.

The results of the trajectory calculations are not easily characterized. Trajectory can be seen to depend sensitively on the point of the charge transfer and on the direction of motion of the atom at the instant of transfer. Ions created in one side of a beam can cross the axis, in some cases, and emerge on the opposite side. Undoubtedly there are even more complications when angular momentum is admitted and the particle then has motion in  $r$ ,  $z$ , and  $\phi$ .

In spite of the complexity, however, some general observations may be made. The first of these is that genuine charge exchange ions do not emerge in backwards directions for angles significantly over  $90^\circ$ .

CONDITION I ION BEAM

$$(r_{ob} = .67b, a_{ob} = .33b, k_1 = .2)$$

$$T_e/T_w = 10$$

ENGINE NEUTRALS (● = SOURCE POINT)

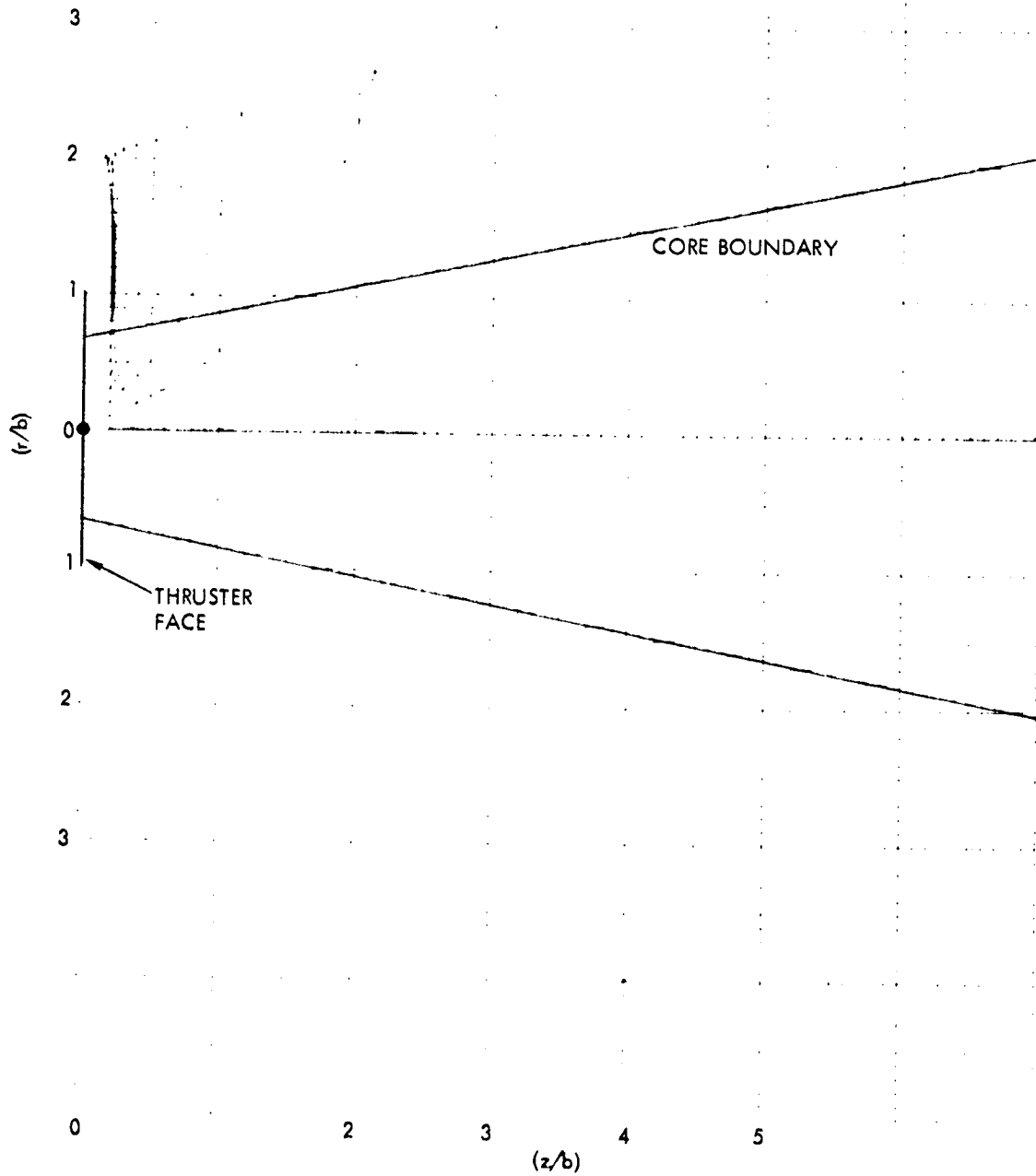


Figure 28. Computed  $Hg^+$  Charge Exchange Ion Trajectories for Engine Released Neutrals at Indicated Source Point and Charge Transfer Point.



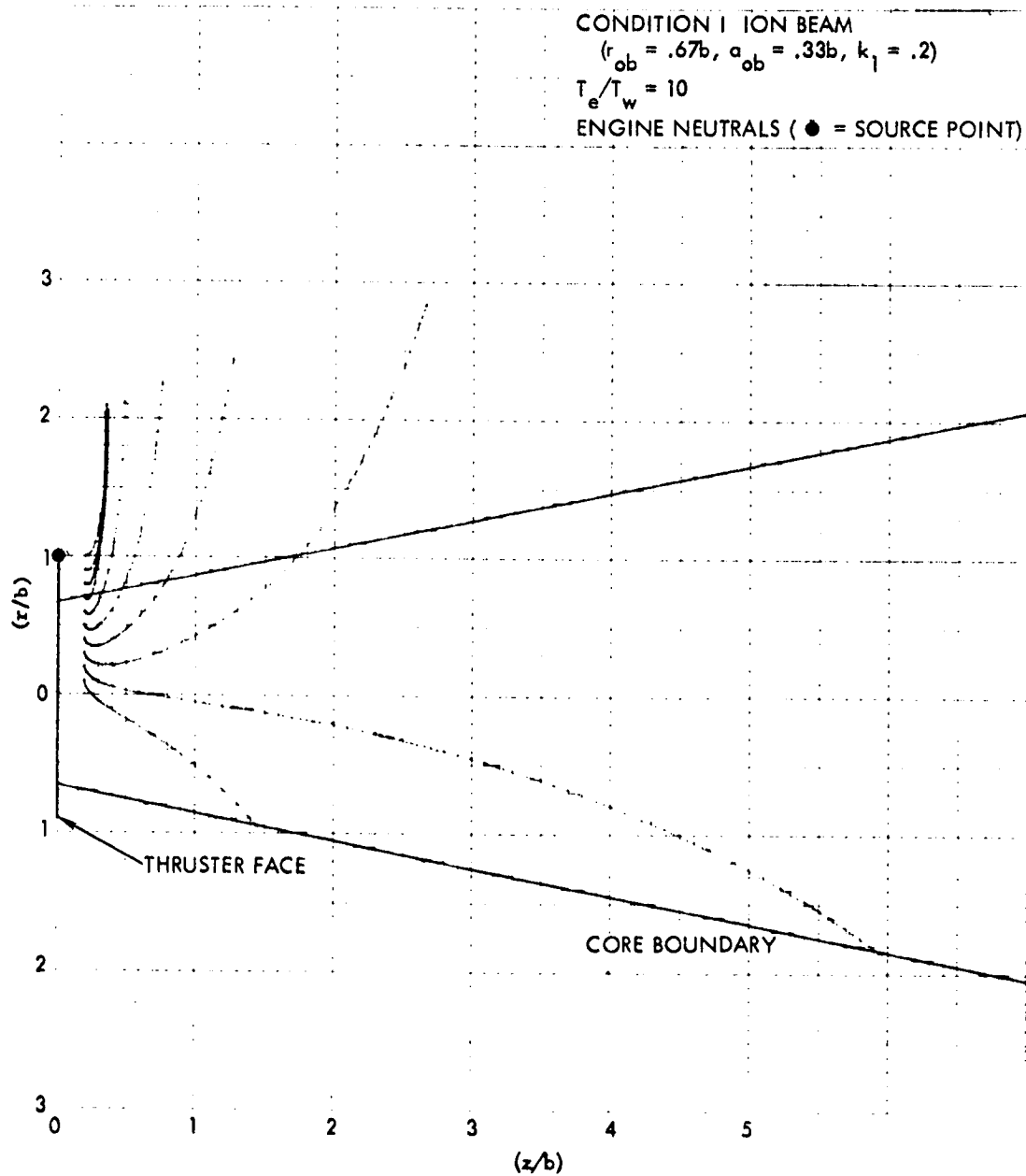


Figure 30. Computed  $Hg^+$  Charge Exchange Ion Trajectories for Engine Released Neutrals at Indicated Source Point and Charge Transfer Point.

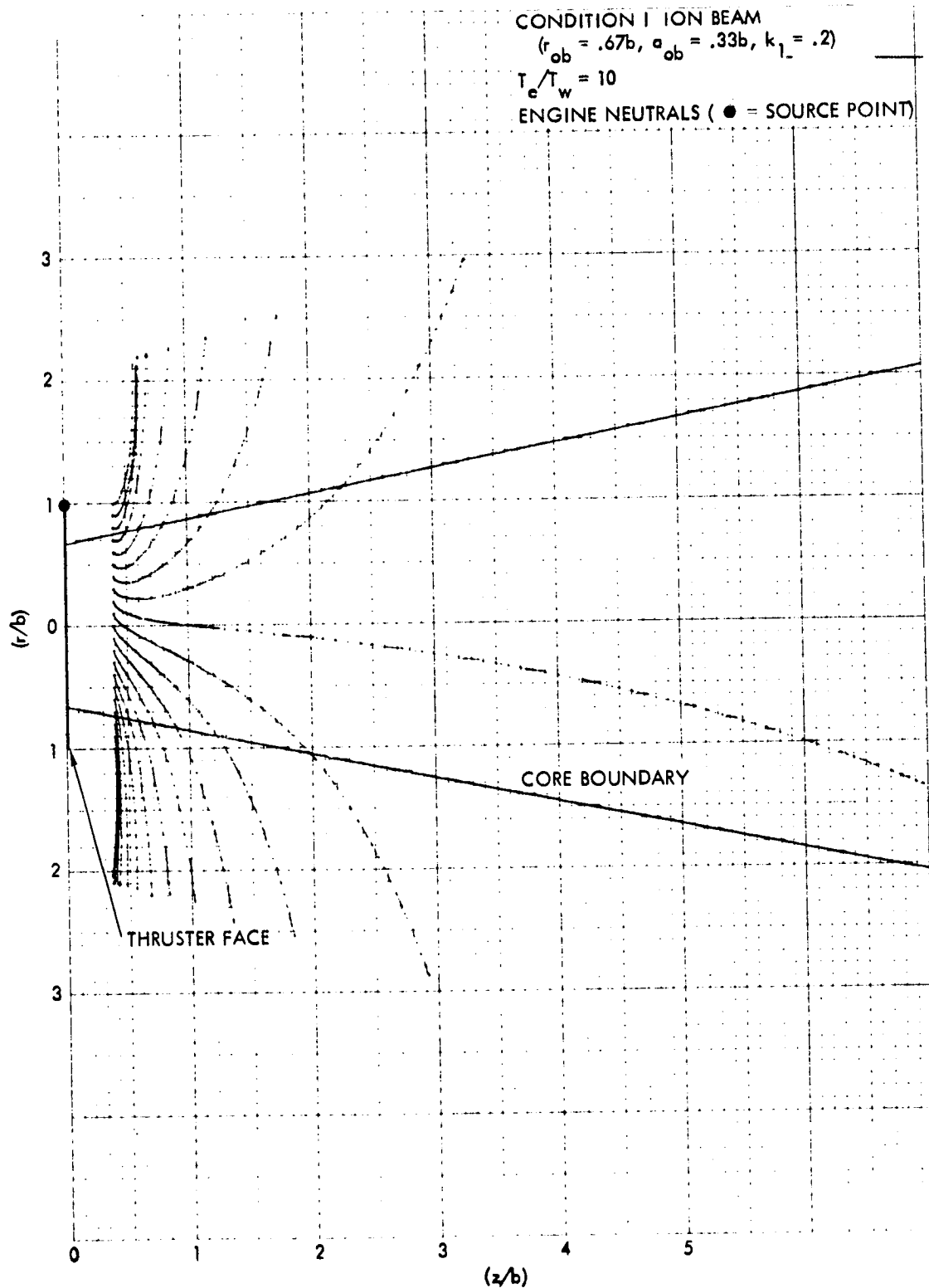


Figure 31. Computed  $Hg^+$  Charge Exchange Ion Trajectories for Engine Released Neutrals at Indicated Source Point and Charge Transfer Point.

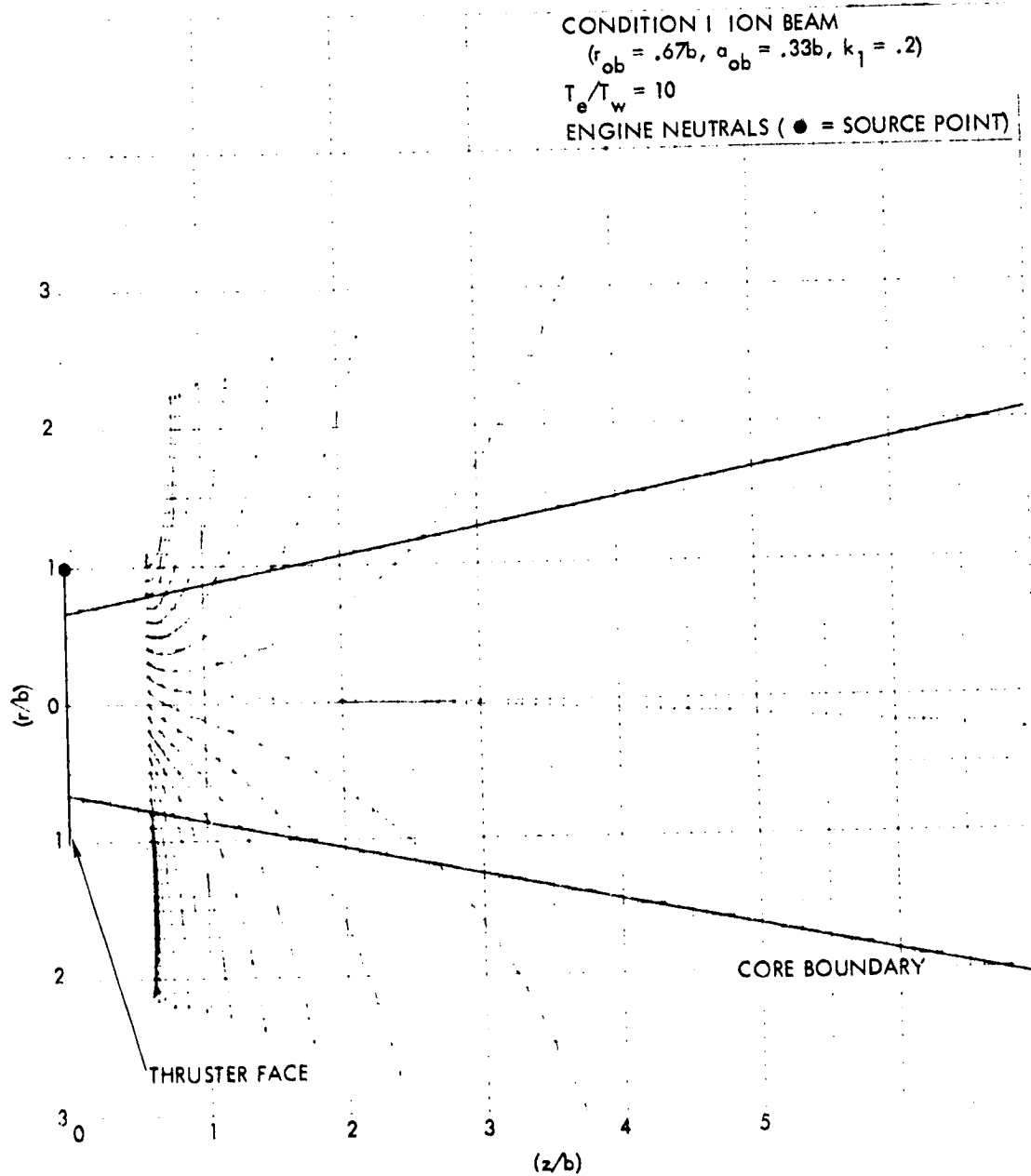


Figure 32. Computed  $Hg^+$  Charge Exchange Ion Trajectories for Engine Released Neutrals at Indicated Source Point and Charge Transfer Point.

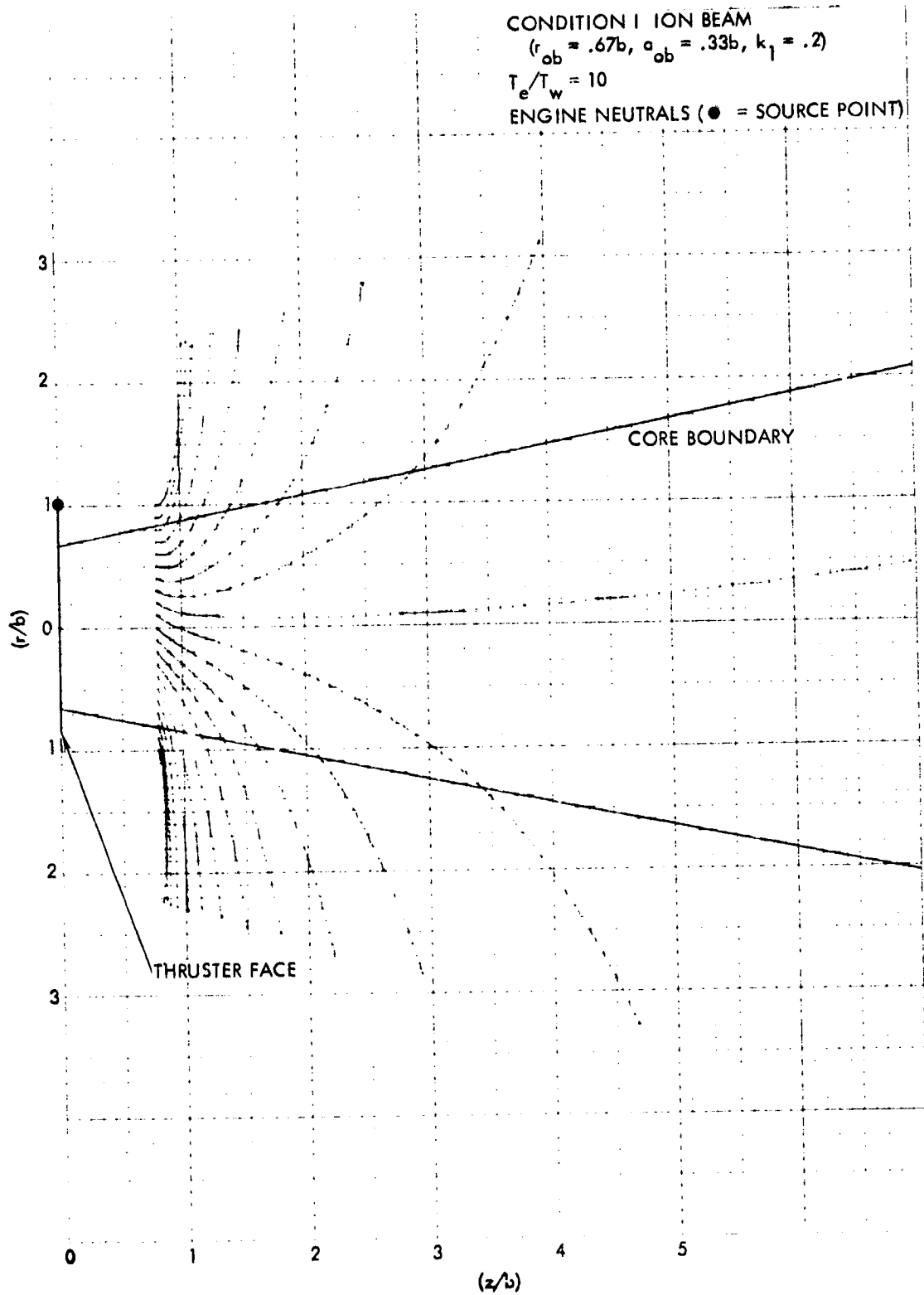


Figure 33. Computed  $Hg^+$  Charge Exchange Ion Trajectories for Engine Released Neutrals at Indicated Source Point and Charge Transfer Point.

CONDITION 1 ION BEAM

$$(r_{ob} = .67b, \alpha_{ob} = .33b, k_1 = .2)$$

$$T_e/T_w = 10$$

ENGINE NEUTRALS (● - SOURCE POINT)

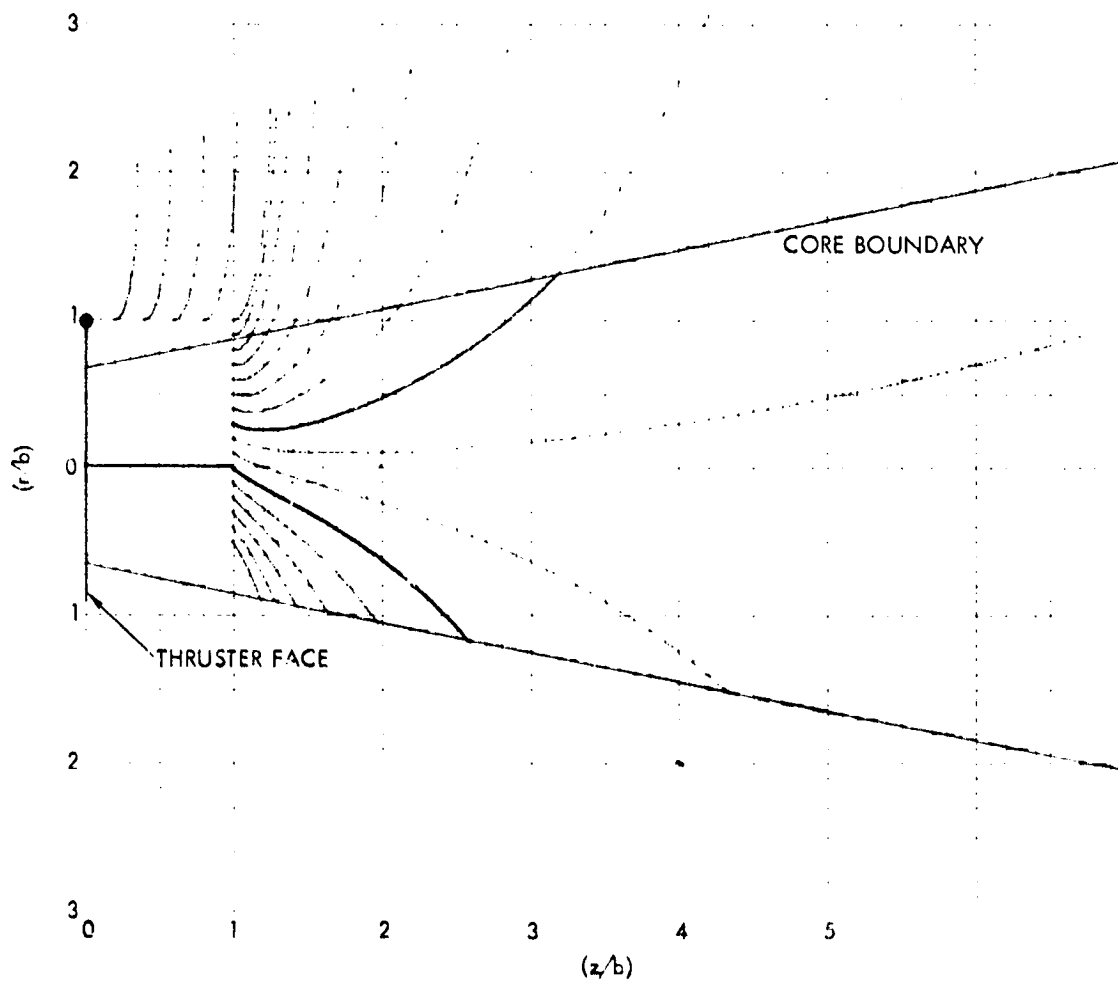


Figure 34. Computed  $Hg^+$  Charge Exchange Ion Trajectories for Engine Released Neutrals at Indicated Source Point and Charge Transfer Point.

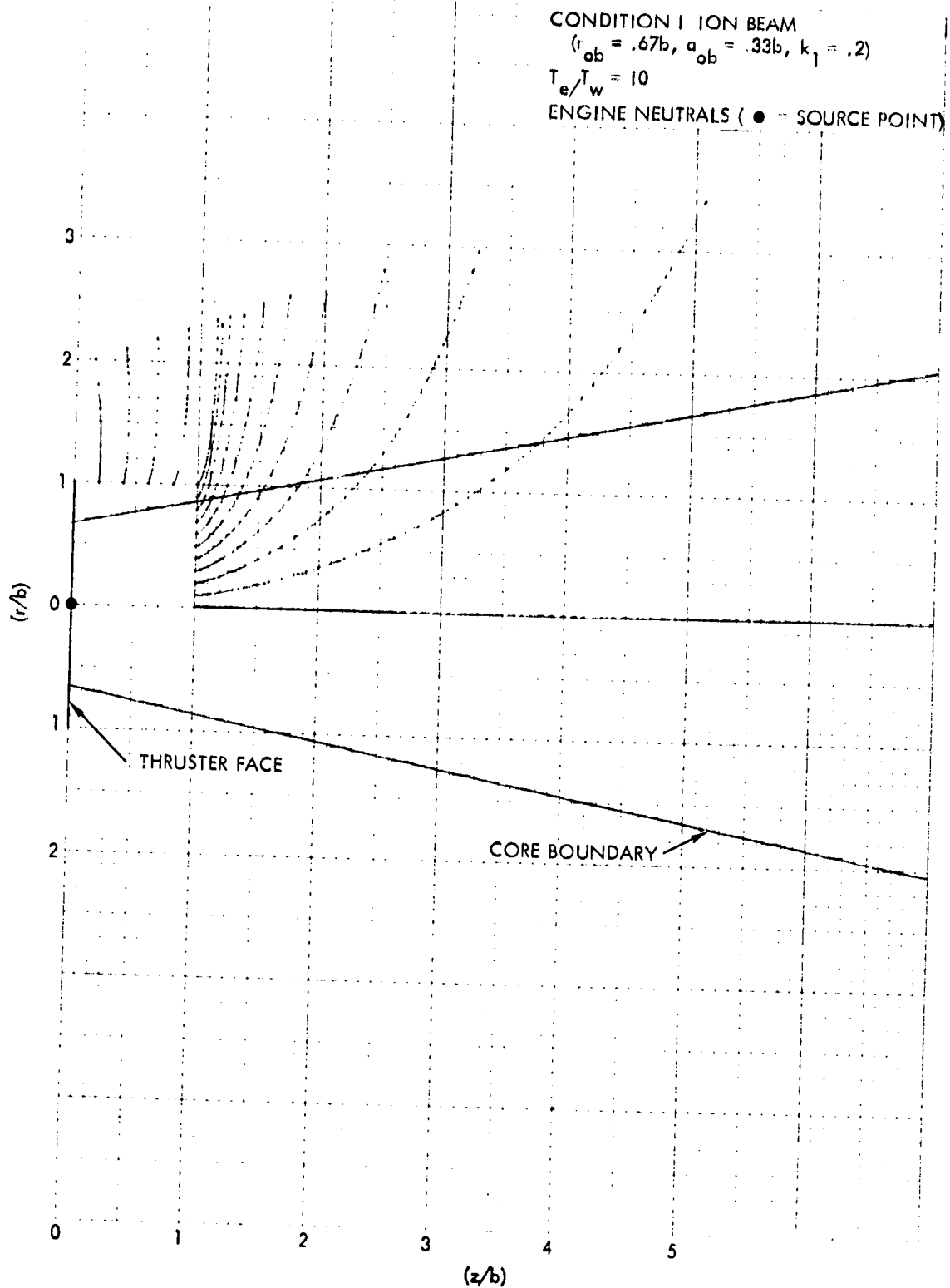


Figure 35. Computed  $Hg^+$  Charge Exchange Ion Trajectories for Engine Released Neutrals at Indicated Source Point and Charge Transfer Point.



Some ions do acquire the backwards hemisphere divergence cone, but the great majority are directed outward at smaller divergence angles. A second observation is that ions formed at  $z$  generally would be perceived by a probe like the 4"  $J_+$  probe at larger  $z$  values. This can be used to explain the general rise in observed probe signal in Region I (see Figure 12) to its plateau levels in Region II.

One additional series of trajectory calculations were carried out for a modified thrust beam shape. In this new beam shape, the divergence constant,  $k_1$ , in Eqs. (10) and (11) was reduced from its value of .2 in the examples above, to .1. This more narrowly diverging beam was expected to possess larger radial fields (compared to the axial fields) than for the more broadly diverging ion beam ( $k_1 = .2$ ). Increased divergence in the electric field angles in the  $k_1 = .1$  beam should, in turn, lead to increased charge exchange ion divergence. This "counter" motion between the thrust ions and charge exchange ion plumes (increasing divergence in one leads to diminished divergence in the other, and vice versa) is expected from general considerations and, from the results in Figures 37 - 41, is confirmed by the calculations. The observed effect is not a major reshaping of the charge exchange ion plume, which is a significant result if alteration of the thruster grid set or electrode voltages leads to an alteration in the thrust ion divergence cone.

### 5.3.2 Facility Effect Charge Exchange Ion Trajectories

#### 5.3.2.1 Thermal Atom/Charge Exchange Ions

The calculations of charge exchange ion trajectories have been carried out for two forms of ambient facility atoms. In this section, thermal atoms ( $T_w \sim 250^\circ\text{K}$ ) will be examined. The value of  $T_e$  has remained at  $5000^\circ\text{K}$  so that the temperature ratio,  $T_e/T_w$ , is 20 for these calculations.

The principal difference for thermal atom/charge exchange ion trajectories from the engine atom case is that, for ambient atoms, all atom directions, prior to the electron transfer, are possible. A backward moving atom, thus, could continue in the backward direction after charge transfer, and would appear as a possible source of the previously observed facility effect ions (see Region I of Figure 12) near  $z = 0$  for the

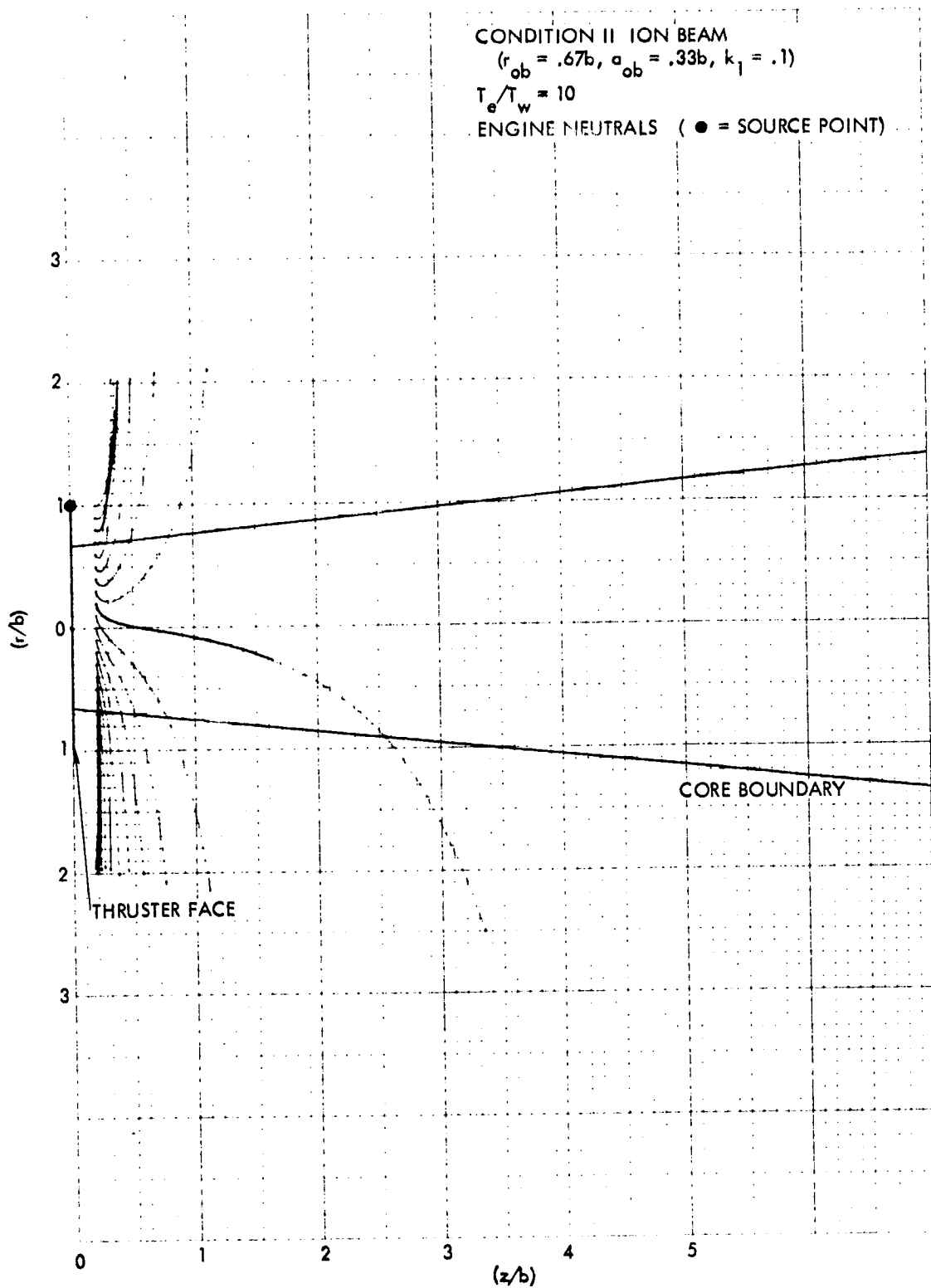


Figure 37. Computed  $Hg^+$  Charge Exchange Ion Trajectories for Engine Released Neutrals at Indicated Source Point and Charge Transfer Point.

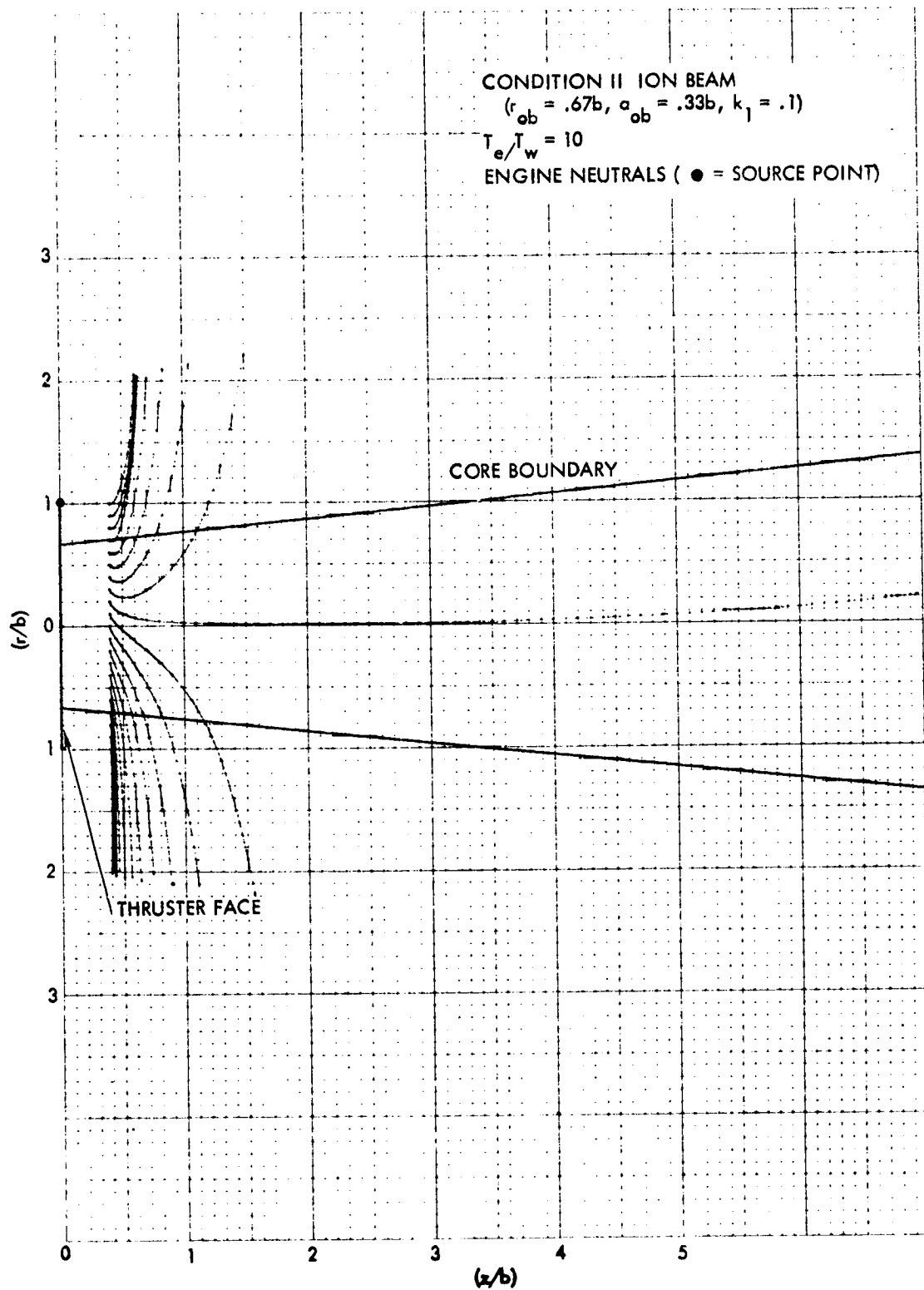


Figure 38. Computed  $Hg^+$  Charge Exchange Ion Trajectories for Engine Released Neutrals at Indicated Source Point and Charge Transfer Point.

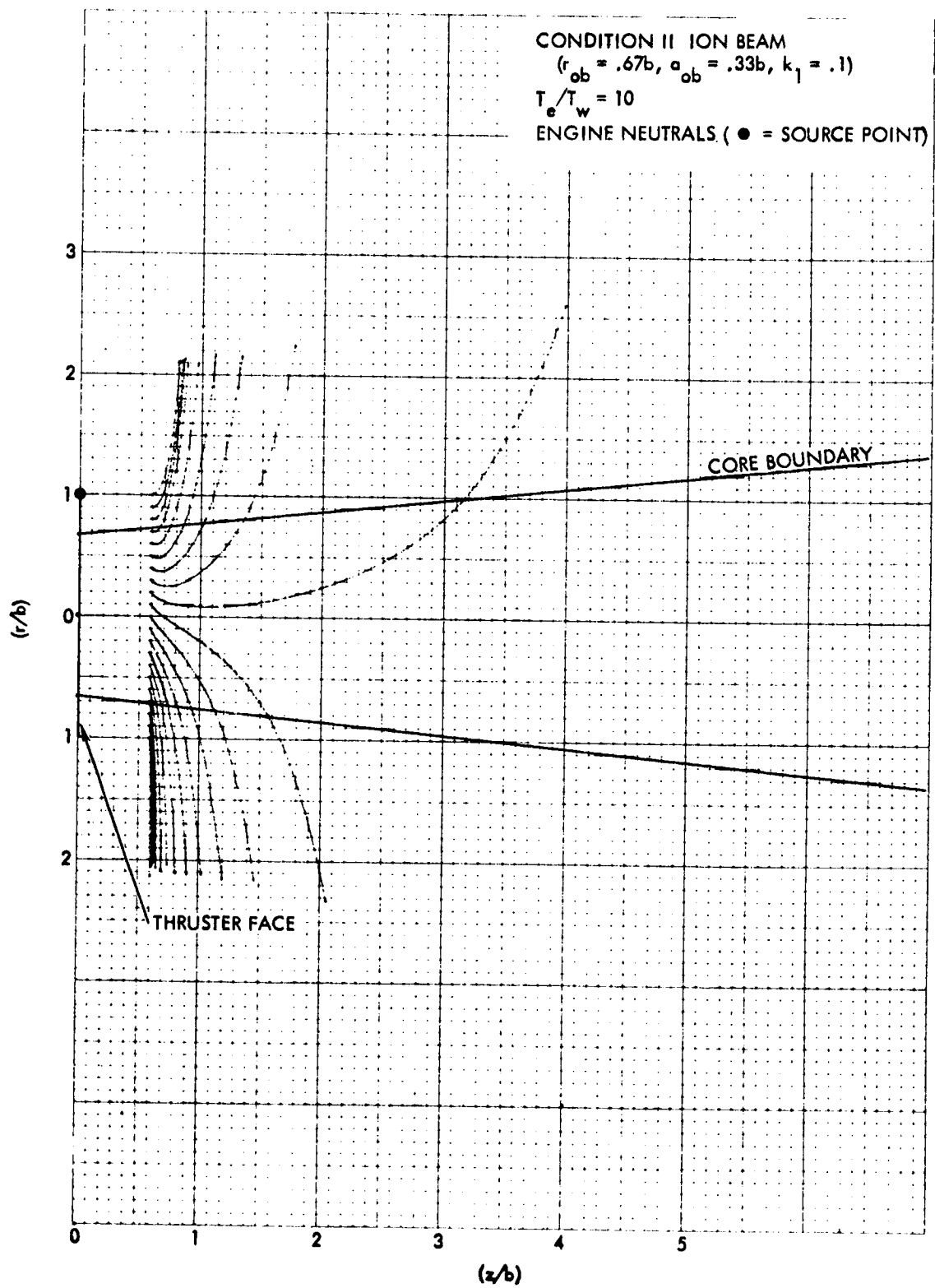


Figure 39. Computed  $Hg^+$  Charge Exchange Ion Trajectories for Engine Released Neutrals at Indicated Source Point and Charge Transfer Point.

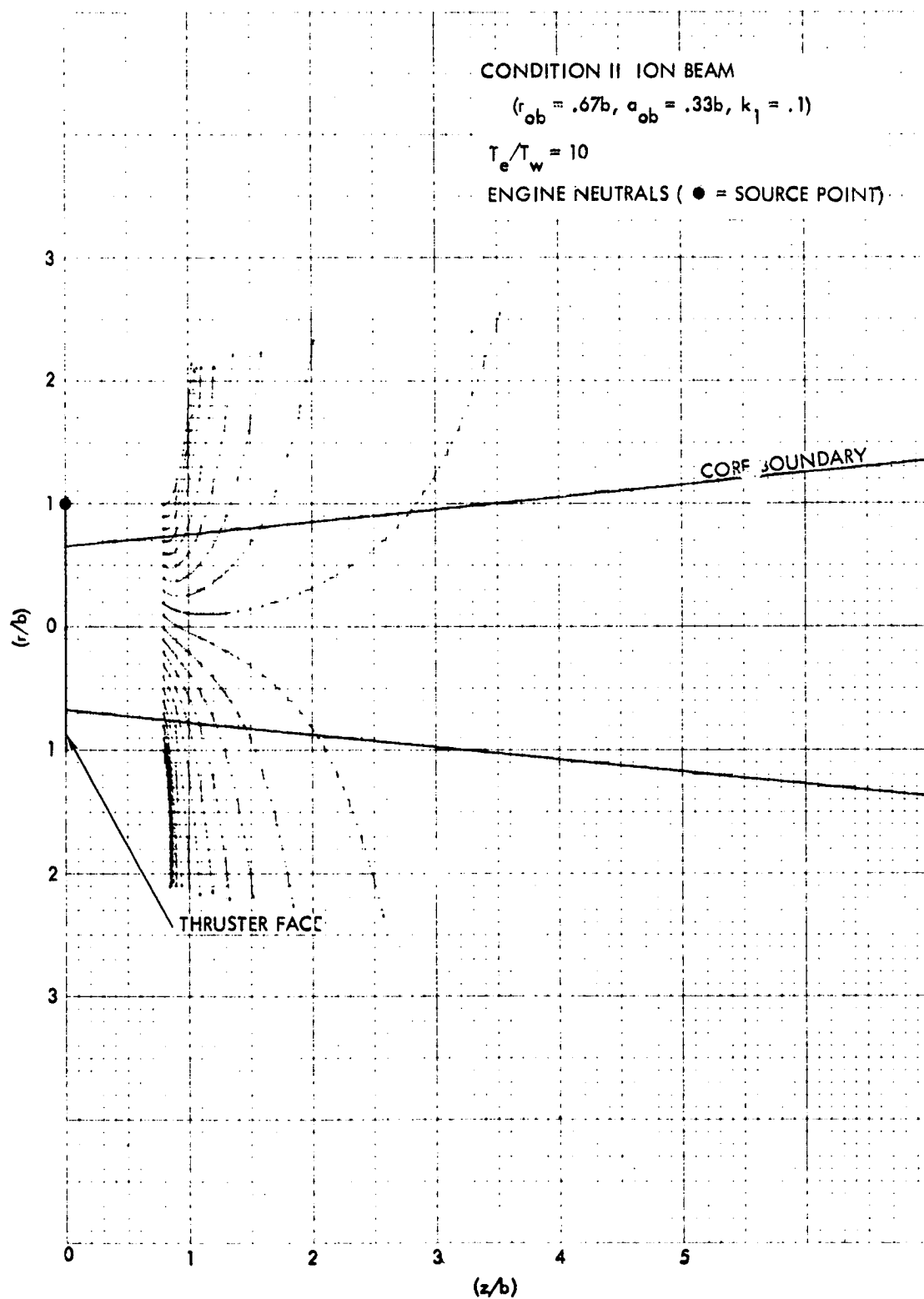


Figure 40. Computed  $Hg^+$  Charge Exchange Ion Trajectories for Engine Released Neutrals at Indicated Source Point and Charge Transfer Point.

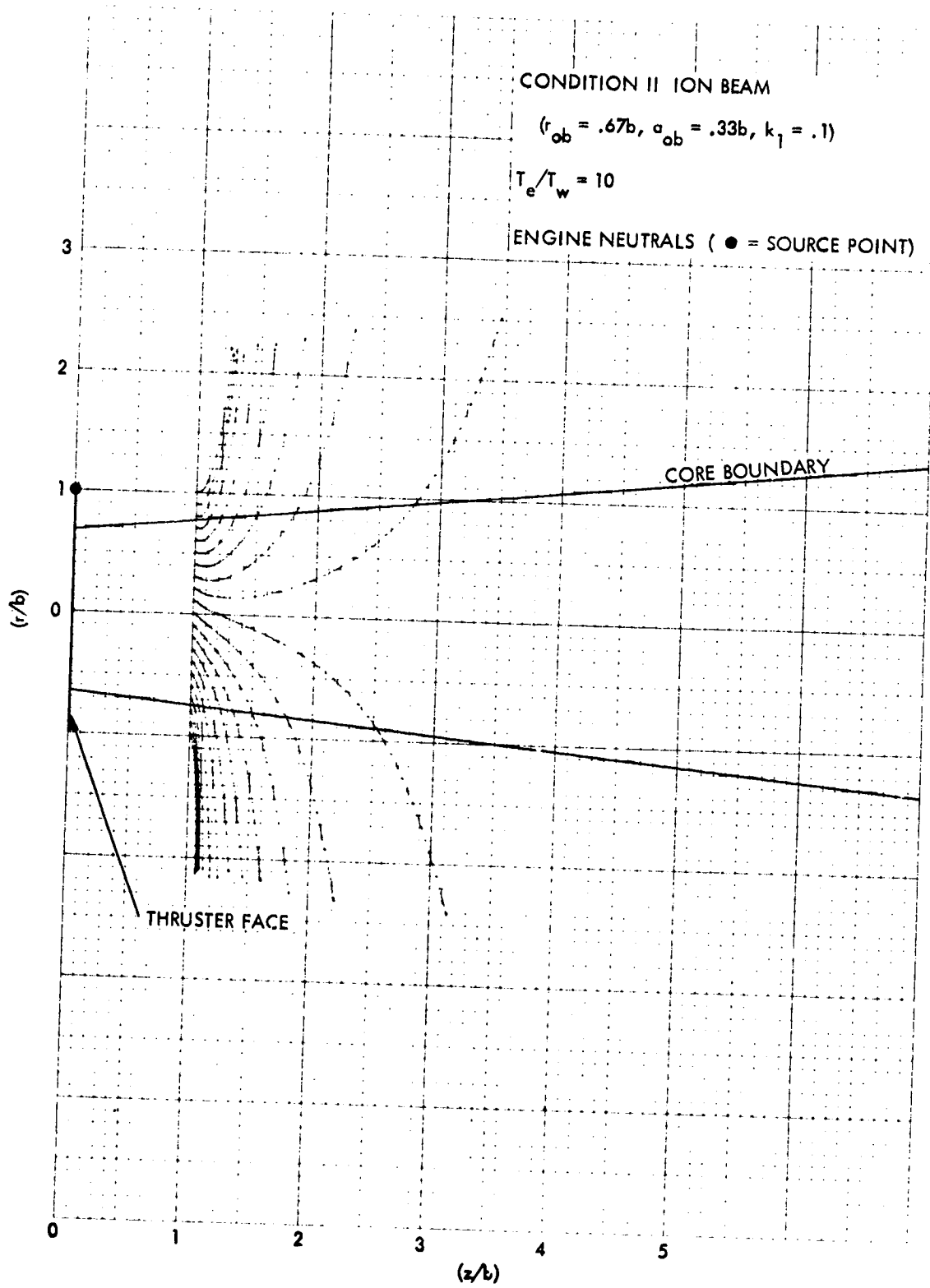


Figure 41. Computed  $Hg^+$  Charge Exchange Ion Trajectories for Engine Released Neutrals at Indicated Source Point and Charge Transfer Point.

4"  $J_+$  probe.

While these back diffusing ions are possible in principle, the calculations have not revealed strong tendencies for such motion for the thermal atom facility effects. Figures 42 and 43 illustrate trajectories for charge transfers occurring at four selected points in the plasma thrust beam. Although some backward ion trajectories are observed, the flow tendencies are more accurately described as being radially outward.

The results of Figures 42 and 43 do not appear to satisfy the observed shape of the charge exchange plume and two principal reasons may be advanced for this failure. A first reason is to note that the backward ions may be the result of charge transfers with more energetic atoms (Section 5.3.2.2). A second possible explanation is that the  $\vec{E}$  fields in these "wing" regions are not accurately described by Eq. (21) and the gradient calculation process. As Section 5.4 will note, the presence of significant levels of charge exchange ions in the dilute outer edges of the thrust ions invalidates plasma density gradient calculations based solely on thrust ions. The  $\vec{E}$  fields in these wing regions could be perturbed, with the perturbation acting to force the direction of  $\vec{E}$  into the backward direction. These factors will be discussed later under charge exchange ion "pile-up" effects.

#### 5.3.2.2 Weakly Energetic Atom/Charge Exchange Ions

Section 3.2 has noted that the ambient atoms also include a weakly energetic component group from the sputtering actions of  $Hg^+$  thrust ions on cryocollectors whose surfaces have resident  $Hg^0$ . The energies of these sputtered atoms could be in the range from fractions of an electron volt up to electron volts, and, because of these larger atom energies, the trajectories of the ions following charge transfer can be continuations of these backward motions. Figure 44 illustrates calculated charge exchange ion trajectories for atoms at 5000°K (which is also  $T_e$ , so that  $T_e/T_w = 1$ ). The calculations clearly illustrate that this increase in atom energy results in more widely dispersed deposition points for those atoms entering into charge transfer reactions. These trajectories may help to explain portions of both the 4"  $J_+$  signal

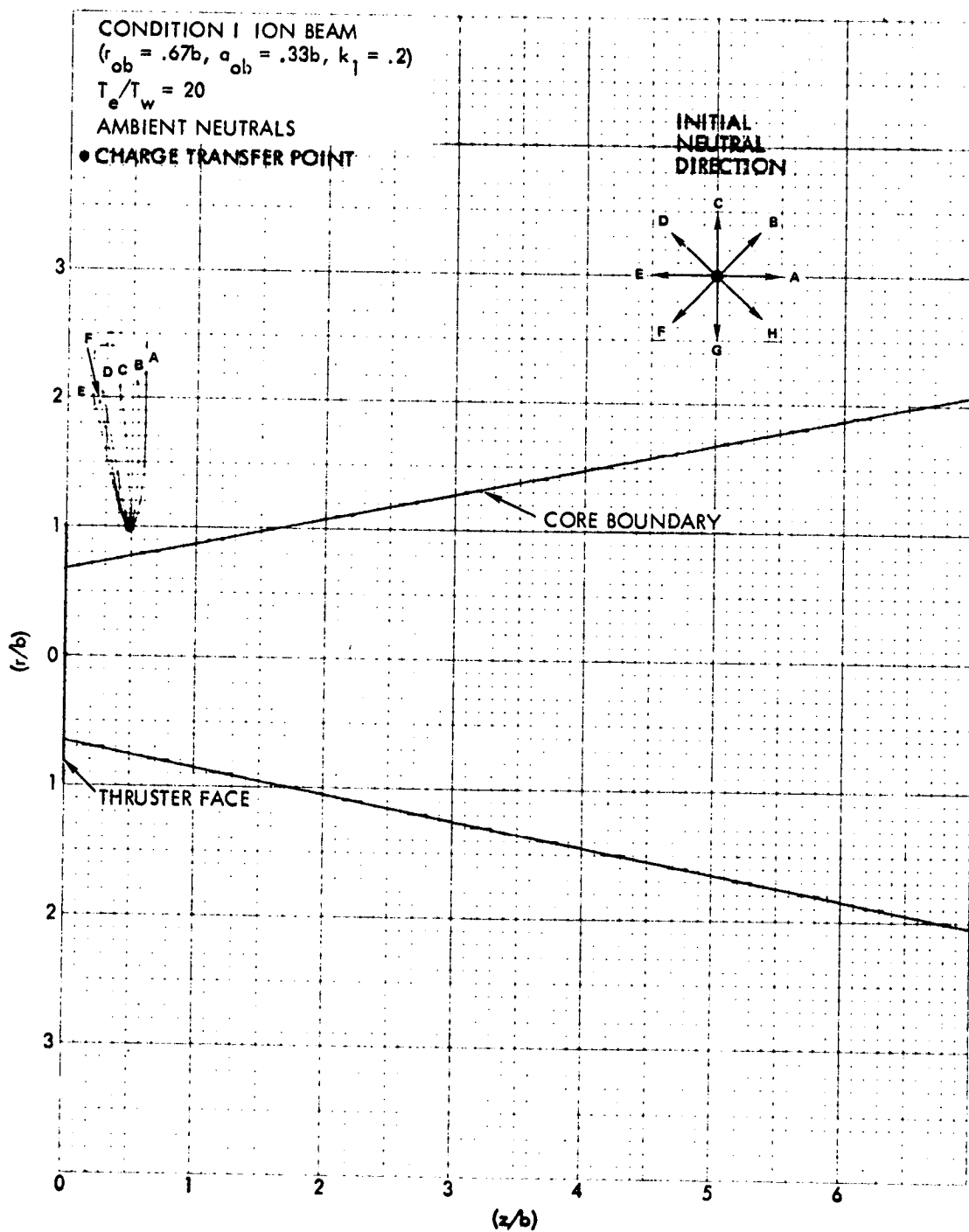


Figure 42. Computed  $Hg^+$  Charge Exchange Ion Trajectories for Ambient Chamber Neutrals at Indicated Charge Transfer Point and Initial Atom Direction.

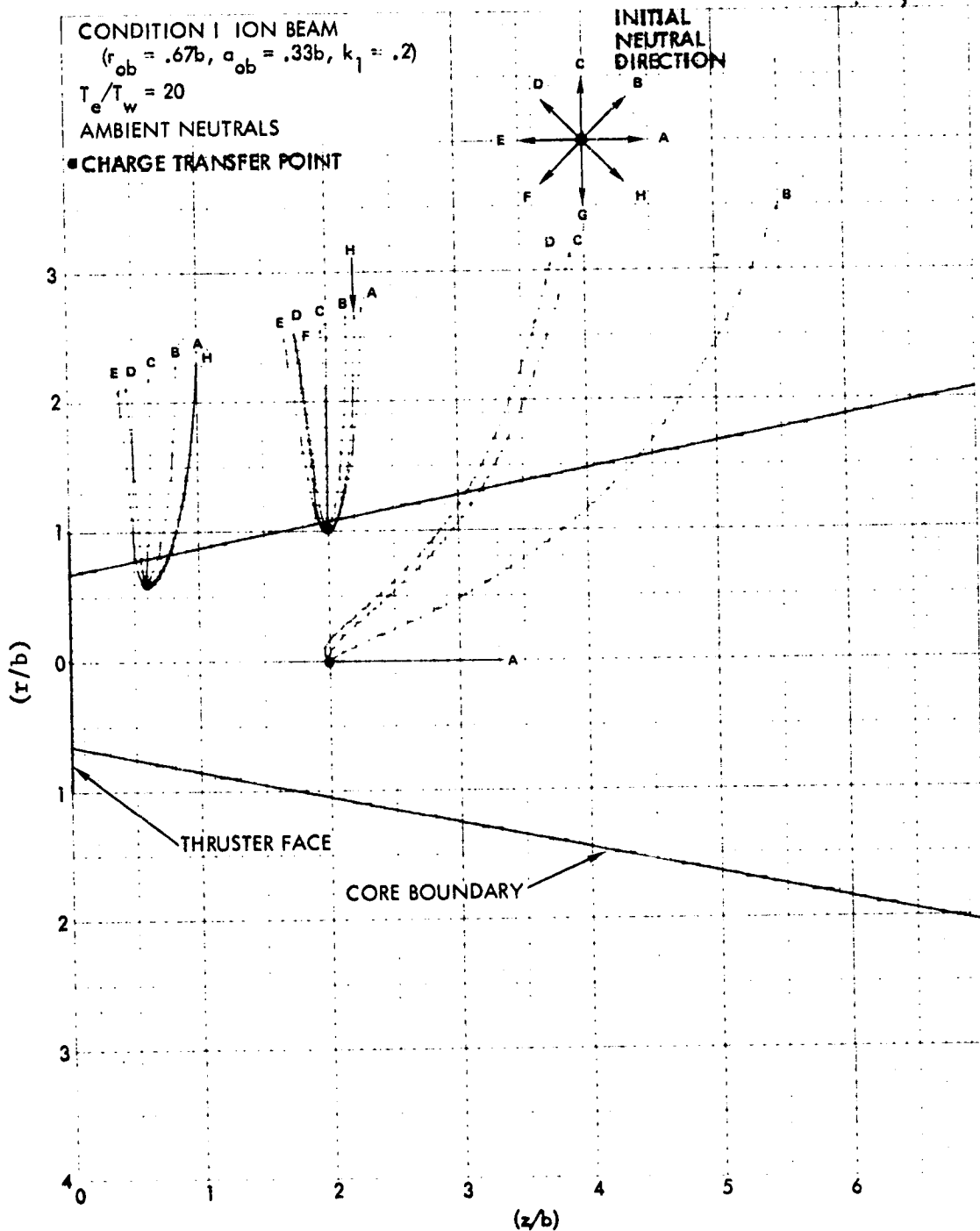


Figure 43. Computed  $Hg^+$  Charge Exchange Ion Trajectories for Ambient Chamber Neutrals at Indicated Charge Transfer Point and Initial Atom Direction.

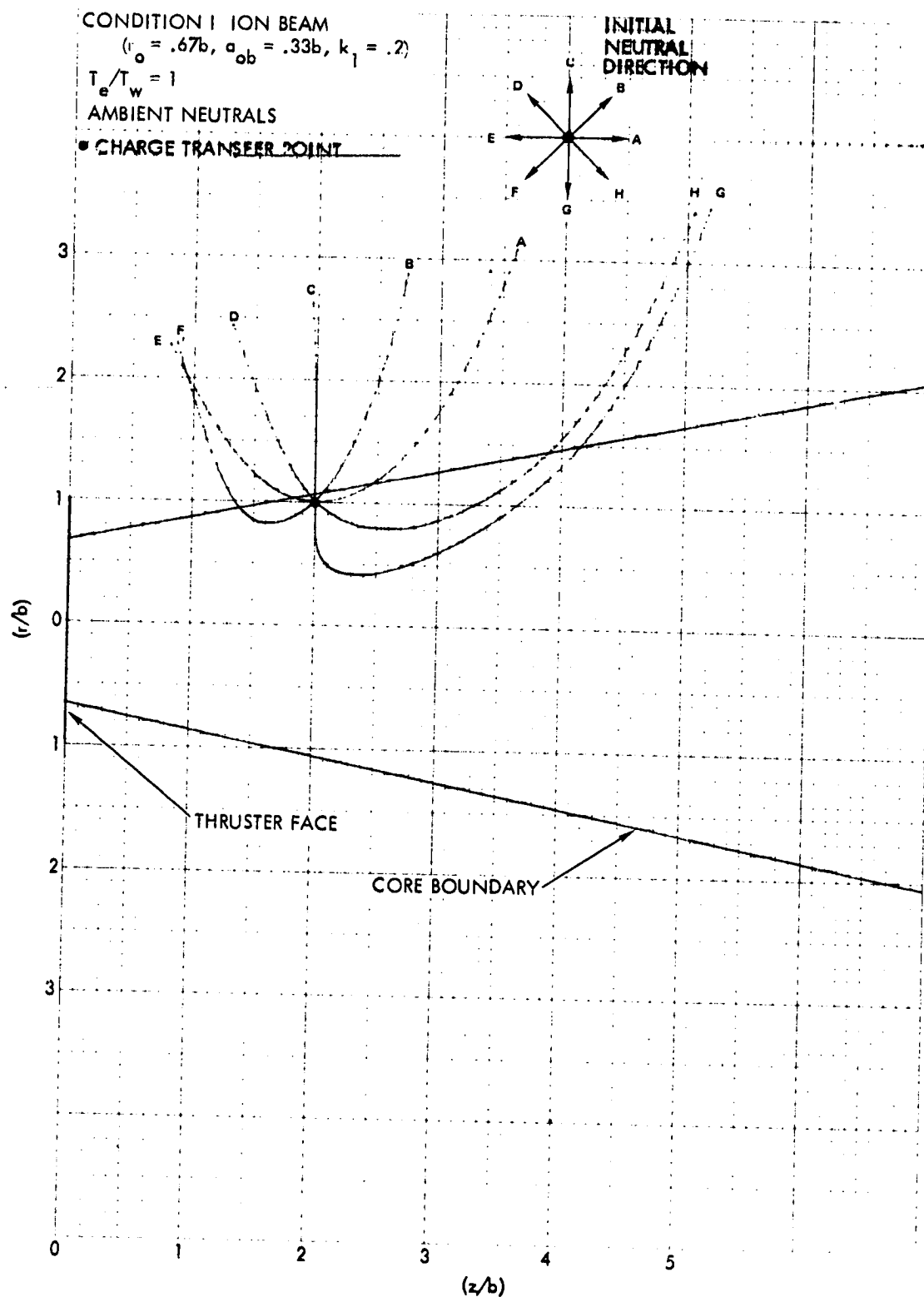


Figure 44. Computed  $Hg^+$  Charge Exchange Ion Trajectories for Ambient Chamber Neutrals at Indicated Charge Transfer Point and Initial Atom Direction.

(near  $z = 0$  for that probe) and the Piggyback  $J_+$  signal (at all  $z$ ). For continued increases in atom energy, the resulting charge exchange ion trajectories will become increasingly more straight line continuations of the earlier atom direction of motion.

### 5.3.3 Comparisons of Observed Group IV Plume Shape to Calculated Trajectories

#### 5.3.3.1 Total Ion Flux as a Function of Axial Distance at Fixed $r = r_p$

Figures 28 through 44 illustrate calculated charge exchange ion trajectories for both genuine charge transfer (with atoms from the thruster) and facility effect transfer (with ambient chamber atoms). Figure 12 illustrates the characteristic plume signal from the 4"  $J_+$  with an approximated "genuine" signal and Figures 14 through 23 illustrate 4"  $J_+$  data for various engine operation conditions. An important question is the internal consistency between these measured and calculated quantities.

The calculations have shown that charge transfer to an  $Hg^0$  escaping from the engine occurs, for the most part, within  $\sim 2b$  ( $b =$  thruster radius) from the engine face, and that the ions so formed will generally encounter the cylinder  $r = r_p$  (on which the 4"  $J_+$  is located) at  $z$  values larger than the  $z$  at which charge transfer occurred. These calculated trajectory features explain the sharp rise in 4"  $J_+$  probe signal for  $z > 0$  and increasing. In many of the 4"  $J_+$  probe signals (Figures 14 - 23), this current reaches maximum levels near  $z \sim 15$  to 20 cm and has a perceptible (though small) decline for further increases in  $z$  to  $\sim 30$  cm. This falloff in probe signal can be attributed to a falloff in genuine  $Hg^+$  formation for increasing  $z$  moving away from the thruster. If the ambient chamber density were zero, it is expected that the observed falloff would be more evident. The facility effect ions are, however, numerous and their presence leads to a continued high level of 4"  $J_+$  probe signal in the range above  $z \sim 20$  cm. An improvement in facility pressure to the range below 1  $\mu$ Torr would, it is felt, clearly reveal the dropoff of ion signals in these downstream regions.

The Piggyback  $J_+$  probe signals (Figures 11 and 24) are not explained by calculated ion trajectories of genuine  $Hg^+$  Group IV or of Group IV from thermal  $Hg^0$  in the test facility. The calculations of

trajectories for  $Hg^+$  formed from weakly energetic ( $\sim eV$  energies) sputtered atoms (see Figure 43) can serve to explain some of the Piggyback signal. Since the currents here are small, however, (fractions of a microampere), other causes must be examined. These other signal sources include low energy  $Hg^+$  trajectory refraction into high angles of divergence by electric fields in the sheath regions between probe surfaces and the charge exchange ion plasma, and a general broadening of the cone of divergence angles of charge exchange ions from "pile-up" effects (Section 5.4.1).

#### 5.3.3.2 Angular Dispersion Pattern of Group IV Ion Flux as a Function of Axial Distance at Fixed $r = r_p$

The angular dispersion patterns of Group IV ions are determined by the  $J_+$  Weasel I and Weasel II probes, which are multicollector retarding potential analyzers, moving at fixed  $r$  ( $\approx 30$  cm) in the axial range from -10 to +30 cm. These probes are illustrated in Figure 8 in Section 2.

Data from the Weasel I and Weasel II probes is given in the Engine Operation Data volume, and will be discussed in this section in qualitative terms. One reason for this reduced emphasis on Weasel probe data has been previously noted, i.e. a concern that the ion flux densities and comparatively long flight paths within the analyzer, combined with the small value of Group IV ion energy, may result in ion trajectory refraction. A second reason for de-emphasis of the Weasel data are signal-to-noise effects in the accumulation of the retarding potential analysis data. As noted earlier in discussions of RPA in the presence of strong hard ion current backgrounds, the presence of secondary electron emission from the collector by energetic ion impact can create the appearance of a "negative" population in the soft ion spectrum. For example, in performing a retarding potential analysis, the retarding potential grid is moved upward from 0 volts to a small positive voltage to prevent the passage of soft ions. Under normal conditions this leads to a diminution of collector current as the soft ion flux is no longer present. If secondary electrons are present, however, the positive motion in potential of the retarding potential grid can cause these electrons (which were previously suppressed) to now leave the collector

surface to be collected at the PP grid. This release of electrons by the collector has the appearance of an increasing positive current signal at the collector, leading to the above mentioned "negative" population of soft ion states.

Spurious signals in the soft ion detection may be expected whenever the ratio of hard ion flux to soft ion flux is about equal to the inverse of the coefficient of secondary electron emission,  $\delta$ . Since  $\delta$  for clean surfaces under energetic  $Hg^+$  impact is generally small, ( $\approx .1$ ), compared to unity, a condition where  $(J_{+hard}/J_{+soft}) > 1/\delta$  requires a significant level of hard ion flux. From the 4"  $J_+$  probe data, such regions are encountered at large  $z$ . For the Weasel  $J_+$  probe this condition is encountered over a wider range in  $z$ . The reason for the difference in ranges of sensitivity is that the 4"  $J_+$  probe has a large solid angle of acceptance, which tends to increase soft ion collection (broadly distributed in direction) over hard ion collection (most of which originates at the thruster face and emerges in a comparatively narrow divergence cone of directions at any one location). The Weasel probes, however, have a small solid angle of acceptance and soft ion current collected at any one collector is reduced considerably from the levels seen in the 4"  $J_+$ . The net result is a significant impact on the quality of the Weasel probe data compared to that of 4"  $J_+$ .

While the Weasel probe data is affected by these considerations, it has been included in the Operation Data Volume and will be reviewed here briefly. Near  $z = 0$ , the soft ion flux is chiefly present at  $\theta = 90^\circ$  and in the two backward channels ( $\theta = 105^\circ$  and  $\theta = 120^\circ$ ). From other discussion and calculations, a major part of the signal at  $z = 0$  is facility generated and might be expected to be directed into the backward hemisphere. For  $z$  in the 10 to 20 cm region (Region II of Figure 12), charge exchange ions appear in all channels, with principal concentration near  $90^\circ$ . The flow, thus, is generally a radial flow.

While some improvements may be made in the Weasel probes, the procedure recommended for future measurements of the dispersion of this soft ion "cloud" is to allow the flow to proceed without perturbation to separation distances which are large compared to the general scale

size of the charge exchange production region. Such conditions can be encountered, in principal, in a large testing chamber with extremely low ambient mercury density. The use of large testing chamber without very low background Hg<sup>0</sup> density is not sufficient, since, as already noted facility generated Hg<sup>+</sup> ions can possess a scale size comparable to the chamber length and there is no possibility of separation from these spurious currents or of probe placement at distances large compared to the ion production volume scale size.

#### 5.4 Limitations and Uncertainties in Group IV Ion Plume Modeling

##### 5.4.1 Validity of Thrust Beam Internal Potential Model

The calculations of charge exchange ion trajectories have assumed the validity of Eq. (21), the plasma beam internal potential formulation, which provides, via the appropriate derivatives, the  $\vec{E}_r$  and  $\vec{E}_z$  functions which govern charge exchange ion motion. There are two presently recognized limitations in this potential formulation.

The first limitation in Eq. (21) appears to be present irrespective of the charge exchange ion build-up and involves the axial potential gradient. The form of Eq. (21), which is an electrostatic modification of the barometric equation, assumes that electrons of temperature  $T_e$  would populate the plasma according to the known ion density distribution,  $\rho_{+,t}(r,z)$ , but without any net diffusion. While the net diffusion of electrons in the radial direction is essentially zero (neglecting here the comparatively small thrust ion radial spreading), electrons must accompany the axial motion of the ions ( $\langle v_e \rangle = v_{+,t}$ ) which calls for a relaxation of the axial electric field predicted from axial derivatives of Eq. (21). This diminution of axial electric field should result in larger divergence angles for the total internal electric field,  $\vec{E} = \vec{E}_r + \vec{E}_z$ , which would result, in turn, for larger divergence angles for charge exchange ion trajectories.

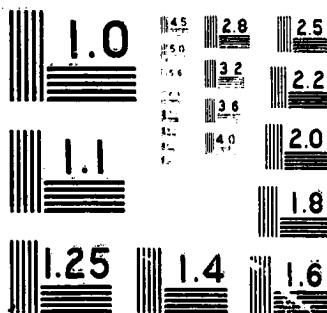
During the measurements program, attempts were made to determine the thrust beam internal potential using the Engine J<sub>+</sub> probe (both casing and collector) as a floating probe. While these floating potential measurements did reveal measurable radial electric fields, potential variations in the axial direction were sufficiently small to avoid



of 2

-25343 UNCLAS

25343 U



MICROCOPY RESOLUTION TEST CHART  
NATIONAL BUREAU OF STANDARDS - 1963

detection, even for comparatively extensive, ( $0 < z < 50$  cm), axial motion of the floating probes. These measurements would appear to confirm the notion of axial potential gradients smaller than predicted from Eq. (21) derivatives. The radial electric field, however, is probably described accurately by the computation program, Eq. (21), and the known thrust ion density distribution.

While the conclusions above are valid in the limit of the thrust ion density as the predominant ion density, another limitation (the second of the two noted earlier) arises from the growth of the charge exchange ion density to that point that the plasma ion density term in Eq. (21) is no longer given from the known thrust ion distribution. Charge exchange ion density growth, or "pile-up", would appear, at first, unlikely, since the currents of these particles are small compared to the thrust ion current. It should be noted, however, that the density of an ion species is describable as a current density divided by the ion flow velocity and that charge exchange ion flow velocities are approximately two orders of magnitude less than thrust ion velocities. Charge exchange ion densities can, thus, become comparable to thrust ion densities, with resulting perturbation to Eq. (21). —

An estimate of conditions under which charge exchange ion density can become comparable to thrust ion density can be derived by considering a cylindrical column of radius  $r$  of thrust ions of constant current density  $J_{+,t}$  moving at  $v_{+,t}$  through a neutral gas density of  $n_n$ . The volume rate of charge exchange ion production

$$\frac{dn_{+cx}}{dt} \left( \frac{\text{coulombs}}{\text{sec cm}^3} \right) = J_{+,t} \sigma_{cx} n_n \quad (6)$$

given in Eq. (6) predicts a total charge exchange production in a cylindrical volume of length,  $d\ell$ , and radius  $r$  of

$$\frac{dN_{+cx}}{dt} = \pi r^2 d\ell (J_{+,t} \sigma_{cx} n_n) \quad (22)$$

These ions, diffusing radially, will remain within the reference volume for a dwell time roughly given by

$$\tau \sim r/v_{+cx} \quad (23)$$

leading to charge exchange ion density given approximately by

$$\rho_{+cx} \sim \left( \frac{J_{+,t} \sigma_{cx} n_n}{v_{+cx}} \right) r \quad (24)$$

This charge exchange ion density will have a value relative to  $\rho_{+,t}$  (the thrust ion density) of

$$\rho_{+cx}/\rho_{+,t} \sim \frac{v_{+,t}}{v_{+cx}} (\sigma_{cx} n_n r) \quad (25)$$

As noted earlier, the velocity ratio  $v_{+,t}/v_{+cx}$  is  $\sim 10^2$ , and  $\rho_{+cx}/\rho_{+,t}$  becomes of order unity for  $\sigma_{cx} n_n r$  of order  $10^{-2}$ . Using  $\sigma_{cx} = 5 \times 10^{-15} \text{ cm}^2$  and  $r$  (for example) = 10 cm leads to a requirement on neutral density of

$$n_n < 2 \times 10^{11} \text{ atoms/cm}^3 \quad (26)$$

for  $\rho_{+cx} < \rho_{+,t}$  for the given choice of radius. The density given above in Eq. (26) corresponds to a chamber pressure of Hg° of  $\sim 6 \mu\text{Torr}$ . Chamber pressure conditions of several  $\mu\text{Torr}$ , thus, can lead to charge exchange production rates sufficient to produce pile-up effects.

The formulation given above is clearly an approximation and a complete and rigorous treatment of pile-up is beyond the scope of this program, since charge exchange ion presence alters the electric fields causing charge exchange ion diffusion, requiring, ultimately, a completely self-consistent iterative calculation of the formation and dispersion of these low energy particles. It is possible, however, to perform a slightly more detailed calculation of these effects. Figure 45 illustrates plasma beam density using Eq. (21) and a parabolic core/exponential wing ion density model, allowing charge exchange formation according to Eq. (6), and radial diffusion only. In the approximation there charge exchange ions move at  $kT_w$ , where  $T_w$  is the wall temperature of the atoms, until that radial position in which  $\rho_{+cx} = \rho_{+,t}$ . Inside this radius the plasma potential is set "flat" (no electric field).

Outside of the radius, the charge exchange ions are assigned velocities which are self-consistent with Eq. (21), and the calculated  $\rho_{+,t} + \rho_{+cx}$ .

The curves in Figure 45 illustrate increasing perturbations to plasma internal density and potential structure for increasing levels of Hg° pressure. Clearly it is desirable to maintain as low as possible an ambient density.

Two final aspects of the calculations here are the multi-dimensionality of the effects, and the possibility that pile-up of these charge exchange ions can cause the "refraction" of charge exchange ion trajectories into the backwards hemisphere (as, for example, appears at the Piggyback  $J_+$  probe). The first aspect noted above is that the effects of charge exchange ion presence become more marked for diminishing thrust ion density. Thrust ion density diminishes in distant axial locations and in the exponential wing regions. Thus, perturbation of the internal potential of the plasma thrust beam is expected for large  $z$ , even on axis, and for large  $r$ , even for small  $z$ . This clearly affects many of the regions treated in the earlier trajectory calculations. Effects here are obviously complicated and no definite estimate can be given to the variation of charge exchange ion trajectories. One possibility, however, is that charge exchange ion build-up, particularly at large  $z$ , causes sufficient elevation of plasma potential at those locations to cause charge exchange ions formed at upstream locations to redirect their flow to higher divergence angles in order to find less thoroughly populated escape routes.

#### 5.4.2 Particle Coordinate Description Limitations

The charge exchange ion trajectory calculations for Figures 28 through 43 were carried out in two dimensions ( $r$  and  $z$ ) only, neglecting azimuthal velocity,  $\dot{\phi}$ , because of the complications which the inclusion of this coordinate would have placed on the trajectory computations. If, at some future date, it is desired to upgrade the analytical model, the inclusion of the  $\dot{\phi}$  term and the modification of the trajectory calculations to three instead of two dimensions is a recommended procedure. The total charge exchange ion plume calculation, then, would consist of a determination of the neutral density and direction distributions at a

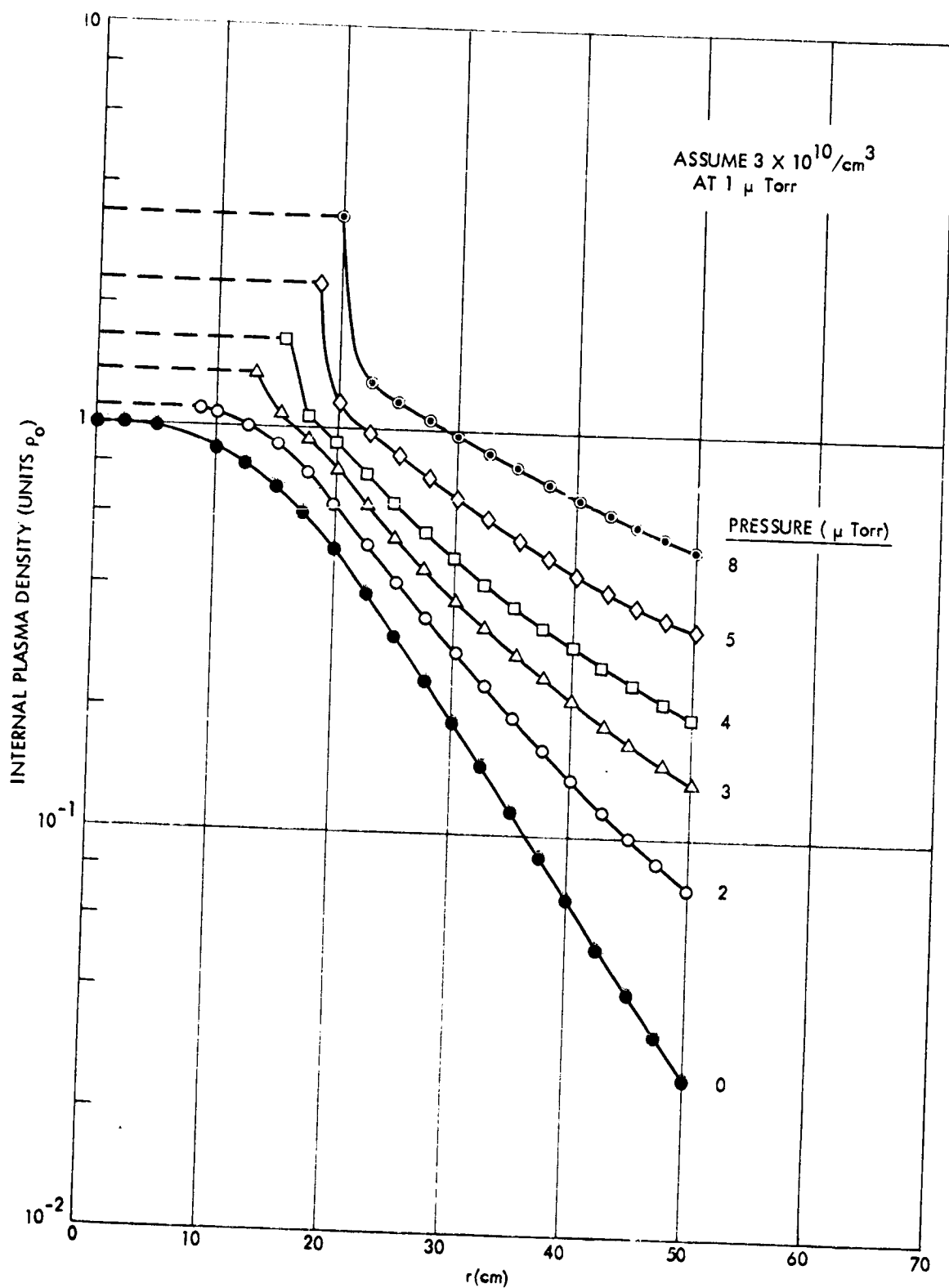


Figure 45. Computed Ion Density Build-up in a Parabolic Core/Exponential Wing Ion Beam from Thrust Ion Charge Transfer to Ambient Hg<sup>0</sup> as a Function of Ambient Pressure.

given  $(r,z)$ , including all possible neutral source points on the thruster face, and the subsequent trajectory calculations. The final charge exchange ion deposition pattern would then require the integral over all possible charge exchange locations  $(r,z)$ . Uncertainties would remain in the calculations from the charge exchange ion presence and its possible perturbation of the potential. In addition, uncertainties in neutral density will be present. These final model elements are discussed in Section 5.4.3, which follows.

#### 5.4.3 Neutral Plume Model Limitations

The charge exchange ion production calculations utilized a neutral plume derived with simplifying assumptions that all neutrals emerge from the thruster, that the neutral emission density is uniform over the thruster face, and that all atoms emerge with a single velocity,  $v_{o,th}$ , determined by the thruster wall temperature. In addition, the angular distribution function for each neutral emission source point has been chosen as either  $\cos \theta$ ,  $\cos^2 \theta$ , or  $\cos^3 \theta$ . An upgrading of the analytical model should include possible non-uniformity of neutral emission over the thruster face, the inclusion of neutrals released at the plasma discharge neutralizer, and the possibility of angular distributions in emission which depart from  $\cos \theta$ ,  $\cos^2 \theta$ , or  $\cos^3 \theta$ . A complete upgrading of the analytical model is, clearly, a non-trivial procedure.

## 6.0 HIGH ENERGY ION FLUX MEASUREMENTS

### 6.1 General Considerations

Measurements of high energy ion fluxes have been obtained from the Engine  $J_+$ , the 1-1/2"  $J_+$ , the Swinging  $J_+$ , and the 4"  $J_+$ . The high energy ion groups of interest here have been previously described in Section 1.0 and are both Groups I and II. In the definition used in this program, Group I ions are formed in the electron bombardment discharge and have been accelerated by the complete potential difference between the bombardment plasma and the thrust beam plasma. Group II ions are the result of charge transfers between  $Hg^+$  and  $Hg^0$  in the accelerator grid-to-screen grid interspace and at potentials positive with respect to the thrust beam plasma.

The Engine  $J_+$  and 1-1/2"  $J_+$  probes provide a measurement of ion flux within the parabolic core/exponential wing regions. Because of cup orientation relative to the axes of rotation by which cup movement is attained, neither the Engine  $J_+$  or the 1-1/2"  $J_+$  probes are effective in measuring high divergence angle ion fluxes. For the large divergence angles the Swinging  $J_+$  and 4"  $J_+$  probes are used. The Swinging  $J_+$  is capable of measurement from the beam axis to  $\sim 90^\circ$  divergence angle. The 4"  $J_+$  has principal regions of effectiveness in the angular divergence range above  $\sim 30^\circ$ .

Determinations of energetic ion flux at high angles is not of major importance in determining thrust efficiency, since the quantity of these particles is small compared to the bulk of the (narrowly diverging) thrust ions. The major concern raised by the energetic, high angle ions is for their possible interception on other system element surfaces or on spacecraft surfaces. In Reference 5 the notion of  $\epsilon \equiv \frac{J_+}{I_{+,t}}$  contours is advanced, and, from allowable surface impact and possible ion thruster throughPut on a primary thrusting mission, location of spacecraft surfaces will generally have to be outside of the  $\epsilon_{+,t} = 10^{-8} \text{ cm}^{-2}$  contours. (Note: For  $10^{26}$  ions released by an ion thruster, deposition on the  $10^{-8} \text{ cm}^{-2}$  contour is  $10^{18}$  ions/cm<sup>2</sup> and can cause an erosion of  $\sim 1000$  Angstroms of surface material). In these measurements it will be seen that satisfaction of surface placement at  $\epsilon < 10^{-8} \text{ cm}^{-2}$  may not

be convenient for all situations, and some procedures to diminish high angle high energy ion flux will probably be desirable. The use of minimum decel will be demonstrated to be an effective method of introducing reductions in the large divergence angle ion flux.

## 6.2 Engine $J_+$ and 1-1/2" $J_+$ Measurements

Measurements of the thrust ion current density at  $z = 4.7, 10.0, 15.0,$  and  $20.0$  cm are given in Figures 46, 47, 48, and 49. The data given there illustrate several commonly observed features in thrust ion density. Near the thruster face ( $z = 4.7$  and  $10.0$  cm) specific ion optical features of the discharge chamber and accelerator grid system are still evident. Because of these fine structure details, density gradients derived from Eq. (10) and Eq. (11) will not be a precise fit to the actual density gradients and  $\vec{E}$  fields from the density gradients and Eq. (21) will differ from the actual plasma beam internal electric fields.

While the modeled density distribution is not a precise fit, it may also be shown to be an adequate representation of the thrust beam. The dots in Figures 46 through 49 illustrate calculated values of Eq. (10) and (11), the parabolic core/exponential wing density model, with  $r_{ob} = 10$  cm,  $a_{ob} = 5$  cm, and  $k_1 = .2$ .

Another measured quantity given in Figures 46 through 49 is the floating potential in the thrust beam plasma, as determined by electrically isolating the Engine  $J_+$  elements (across 10 megohms) and recording the floating voltage of the probe as it is moved through the beam. There are several features of interest in this data. First, the floating potential is essentially the known potential on the neutralizer keeper electrode, indicating good coupling of the neutralizer to the thrust beam. This tight coupling and small injection potential indicate, in turn, a comparatively low value of  $T_e$ , thrust beam neutralizing electron temperature. This is borne out in the data of Figures 46 - 49 by the very weak increments in floating potential as the probe moves from the dense plasma near the axis into the more dilute regions of plasma in the wing regions.

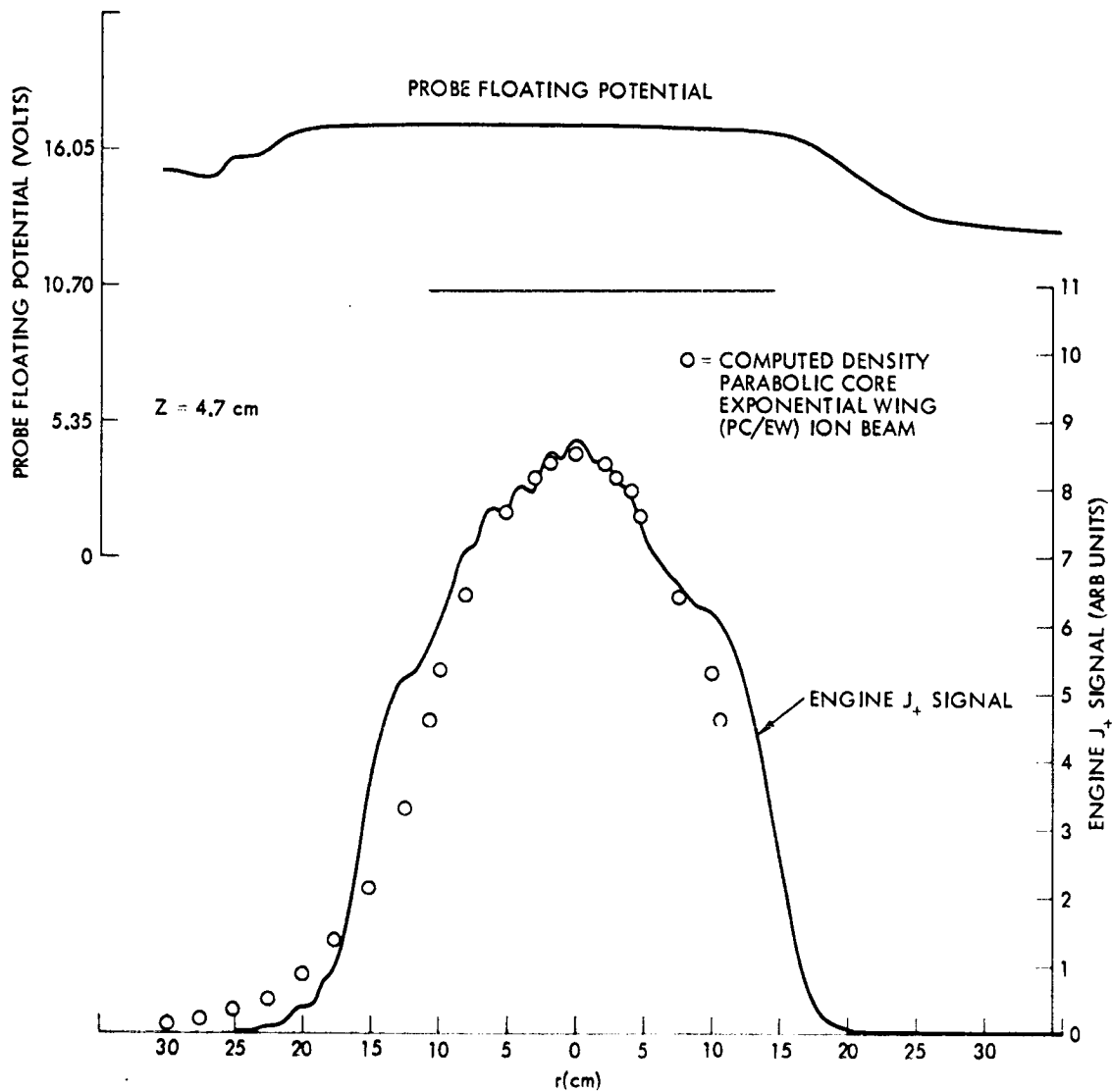


Figure 46. Engine  $J_+$  Current and Floating Potential as a Function of  $r$  at  $z = 4.7$  cm, with Computed Values of Density from Parabolic Core/Exponential Wing Thrust Beam Model.

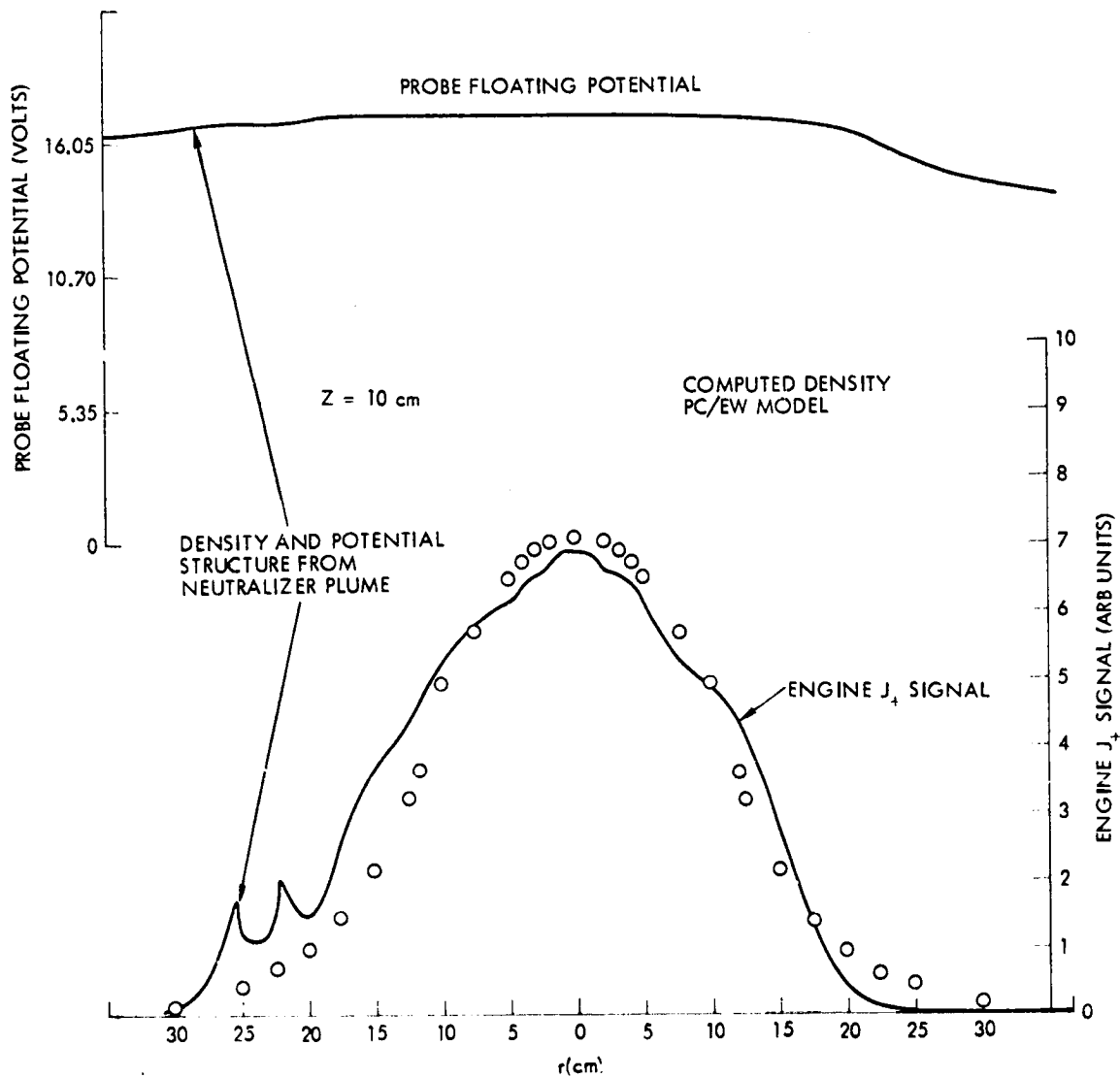


Figure 47. Engine J<sub>+</sub> Current and Floating Potential as a Function of  $r$  at  $z = 10$  cm, with Computed Values of Density from Parabolic Core/Exponential Wing Thrust Beam Model.

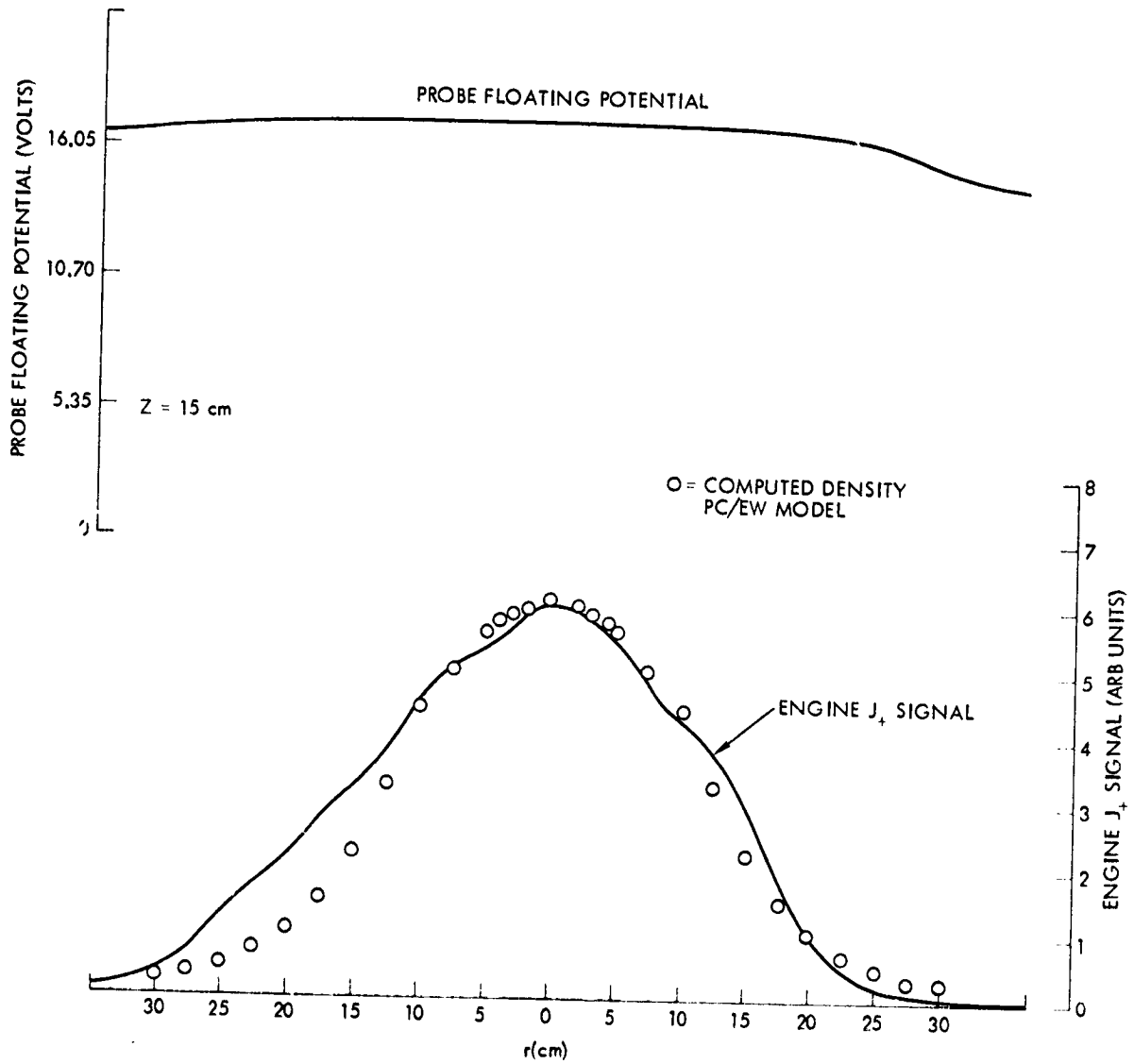


Figure 48. Engine J<sub>+</sub> Current and Floating Potential as a Function of  $r$  at  $z = 15$  cm, with Computed Values of Density from Parabolic Core/Exponential Wing Thrust Beam Model.

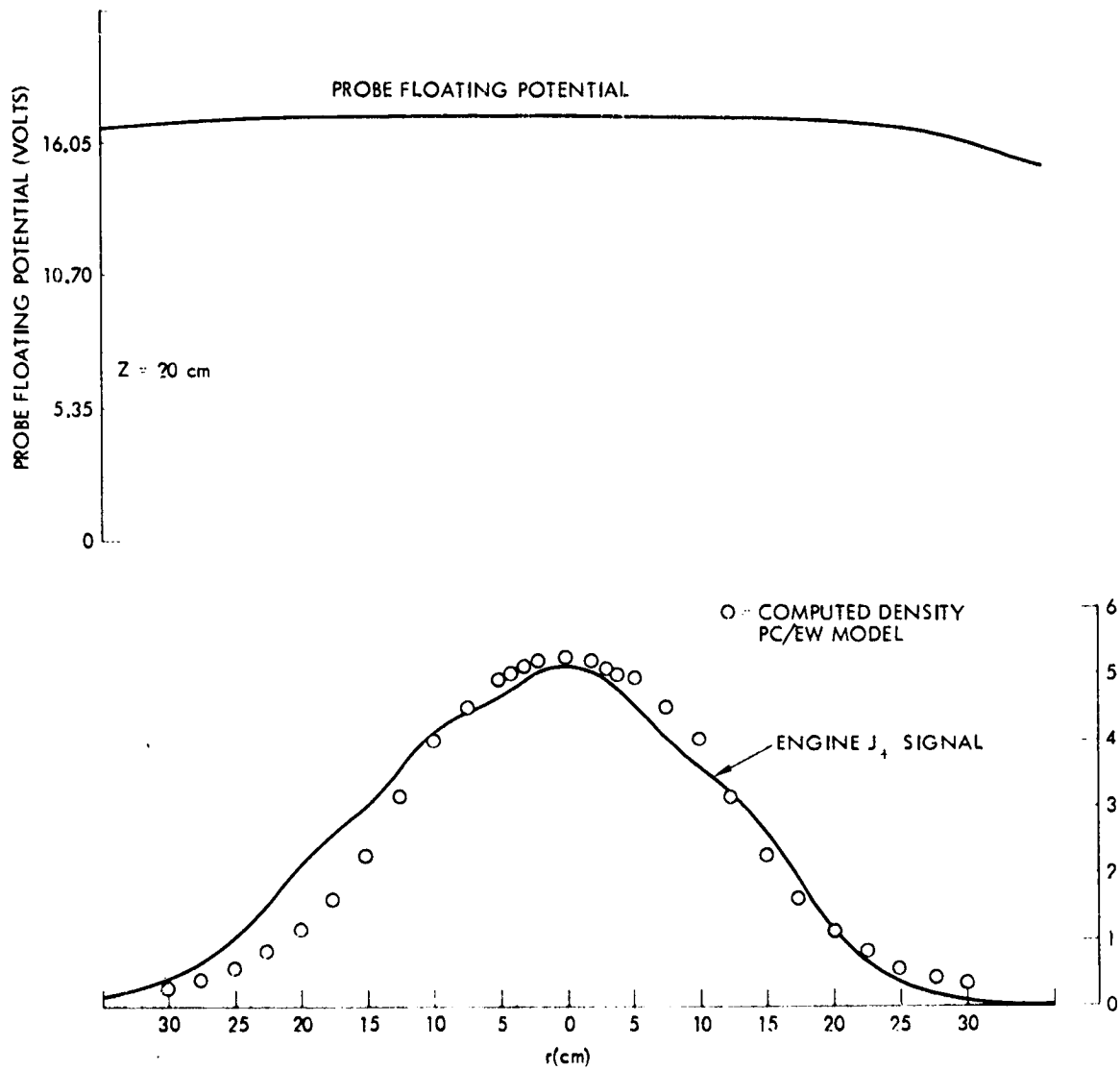


Figure 49. Engine J<sub>1</sub> Current and Floating Potential as a Function of  $r$  at  $z = 20$  cm, with Computed Values of Density from Parabolic Core/Exponential Wing Thrust Beam Model.

A third aspect of interest in the Engine  $J_+$  floating potential is the invariance in floating potential for increases in  $z$ . Section 5.4.1 has noted possible failure of  $\vec{E}_z$  to be described by axial density gradients in Eq. (10) and the potential formulation of Eq. (21). It would appear from the measurements that axial  $\vec{E}$  fields are very weak in this region of the beam, and that the charge exchange ion trajectories calculated from Eq. (10), (11) and (21), have overestimated the axial acceleration of the charge exchange ions.

The measurements of the 1-1/2"  $J_+$  probe are similar to those of Engine  $J_+$ , but allow determinations of  $J_{+,t}$  larger  $z$  values. For brevity, results from this probe have not been included here, but are given in the Engine Operation Data Volume.

### 6.3 High Angle High Energy Ion Measurements

#### 6.3.1 4" $J_+$ Measurements

Figures 14 through 23, in Sections 4.5 through 4.7, have illustrated the 4"  $J_+$  probe signal as a function of  $z$  for all ions, for ions with energies greater than 95 eV, and for ions with energies less than 25 eV, as engine operation conditions (see Table 3) were varied. The discussion in Section 4 concentrated attention on the Group IV ions. Discussion in this section will consider the Group I and Group II ions. For brevity in this report, the figures will not be repeated in this section and reference is made to their earlier presentation.

Figures 14 and 15 illustrate hard ion currents as the engine screen grid potential is varied from 1.5 kV to 0.7 kV. The increase in the decel-accel for Engine Condition 18 (Table 3) clearly causes an increase in the high angle energetic ion flux. At  $z = 5$  cm ( $\theta \sim 80^\circ$ ), for example, the cup current increases from 4.5  $\mu$ amperes to 24  $\mu$ amperes, as screen voltage lowers from 1.5 kV to .7 kV, increasing the decel-accel ratio from 1.33 to 1.71. (Note that decel-accel ratio,  $\Gamma$ , is defined here as  $(V_s + |V_g|)/V_s$  and approaches unity as  $V_g \rightarrow 0$ ).

A second quantity of interest in the data of Figure 14 is the magnitude of high angle high energy currents near  $\theta \sim 90^\circ$ . Since cup area is  $\sim 100$  cm<sup>2</sup>, the 1  $\mu$ ampere of hard ions observed at  $z \sim 0$ , correspond

to a current density of  $\sim 10^{-8}$  amperes per square centimeters, and to  $\epsilon_+ (= J_+/I_{+,t})$  of  $\sim 10^{-8} \text{ cm}^{-2}$ . From previous discussion it has been noted that maximum allowable  $\epsilon$  for hard ions, to avoid surface damage, is  $\sim 10^{-8} \text{ cm}^{-2}$  and, thus, that safe surface placement for this present engine could not be in the forward hemisphere. It will be seen that this condition can be improved by reductions in accelerator grid potential to "minimum" deceleration levels.

Figures 16 and 17 illustrate hard ion currents as a function of  $z$  for a nominal 2 ampere thrust beam, 1.1 kV o. screen potential, and  $-.55$  and  $-.3$  kV as accelerator grid potential. Clearly, the reduction of the decel-accel ratio has caused a reduction in high angle energetic ion flux. This is demonstrated again in Figures 18, 19, and 20, for a nominal 1 ampere ion thrust beam, 1.1 kV screen potential, and accelerator grid potentials of  $-.1$  kV,  $-.5$  kV, and  $-.7$  kV. At  $z = 10$  cm ( $\theta \sim 70^\circ$ ), the hard ion current density increases from  $1 \times 10^{-7}$  amperes/cm<sup>2</sup>, to  $7 \times 10^{-7}$  amperes/cm<sup>2</sup>, to  $13 \times 10^{-7}$  amperes/cm<sup>2</sup> as decel-accel ratio increases from 1.09 to 1.45 to 1.64.

Figures 21 and 22 illustrate hard ion currents as a function of  $z$  as bombardment discharge potential varies from 43 volts to 34 volts (for fixed total discharge power). There is no apparent variation of significance in the high angle energetic ion flux as this engine parameter, varied, and, on reasonable grounds, none was expected.

A final measurement of high angle energetic ions by the 4"  $J_+$  as thruster conditions varied is in Figure 23, where neutralizer flow was altered to cause a variation in keeper potential. No significant shift in hard ion current was observed, and none was expected.

### 6.3.2 Swinging $J_+$ Measurements

The Swinging  $J_+$  probe allows measurement of ion currents at divergence angles up to  $90^\circ$ . Because of the mounting of the probe and the method of probe motion, the axis of this Faraday cup intersects the thruster face at  $r = z = 0$  for all  $\theta$ .

Examples of Swinging  $J_+$  total ion current (both hard and soft ions) are given in Figures 50 and 51 for thrust ion beams of 1.5 and

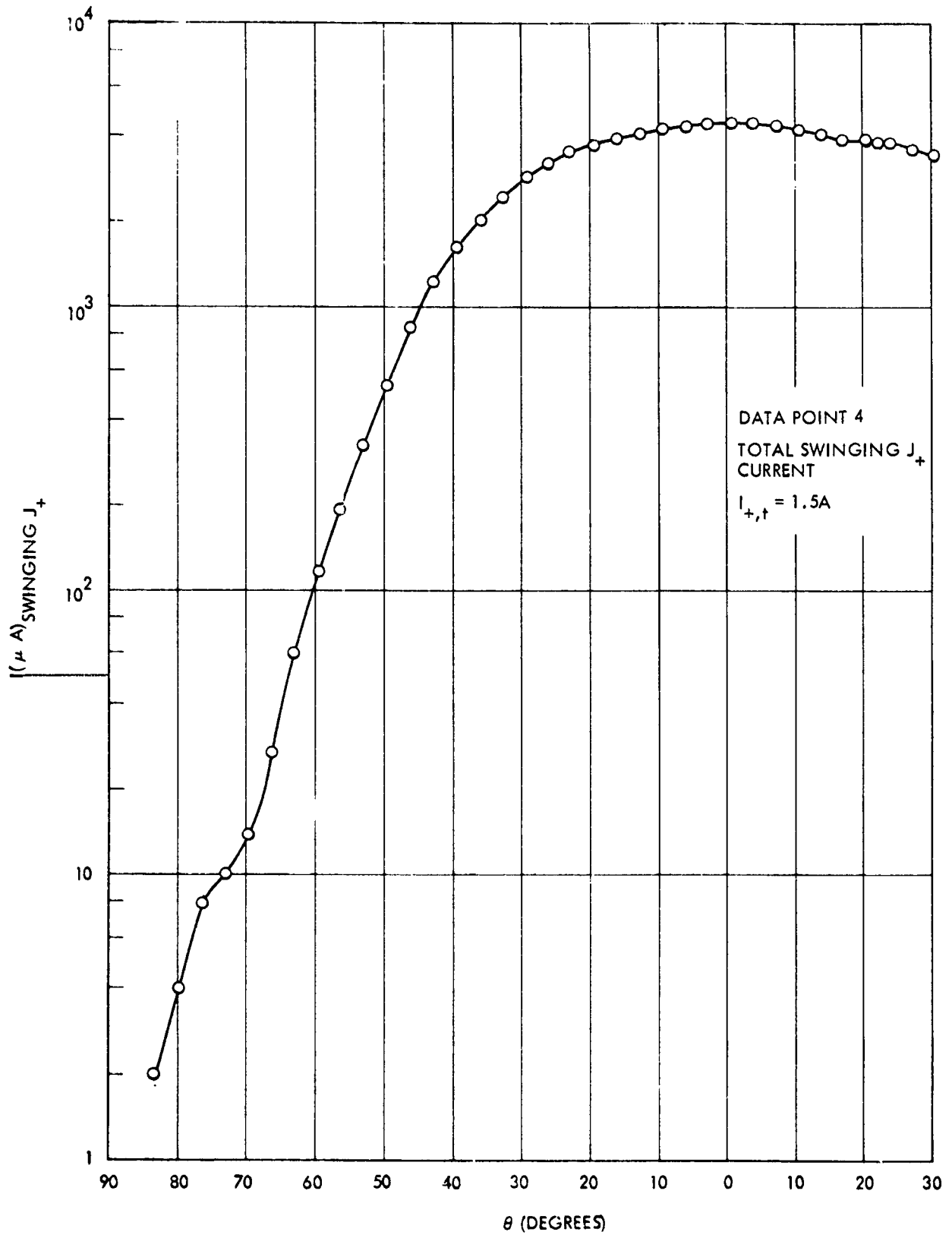


Figure 50. Swinging  $J_+$  Total Ion Current as a Function of  $\theta$  for Engine Operation Data Point 4.

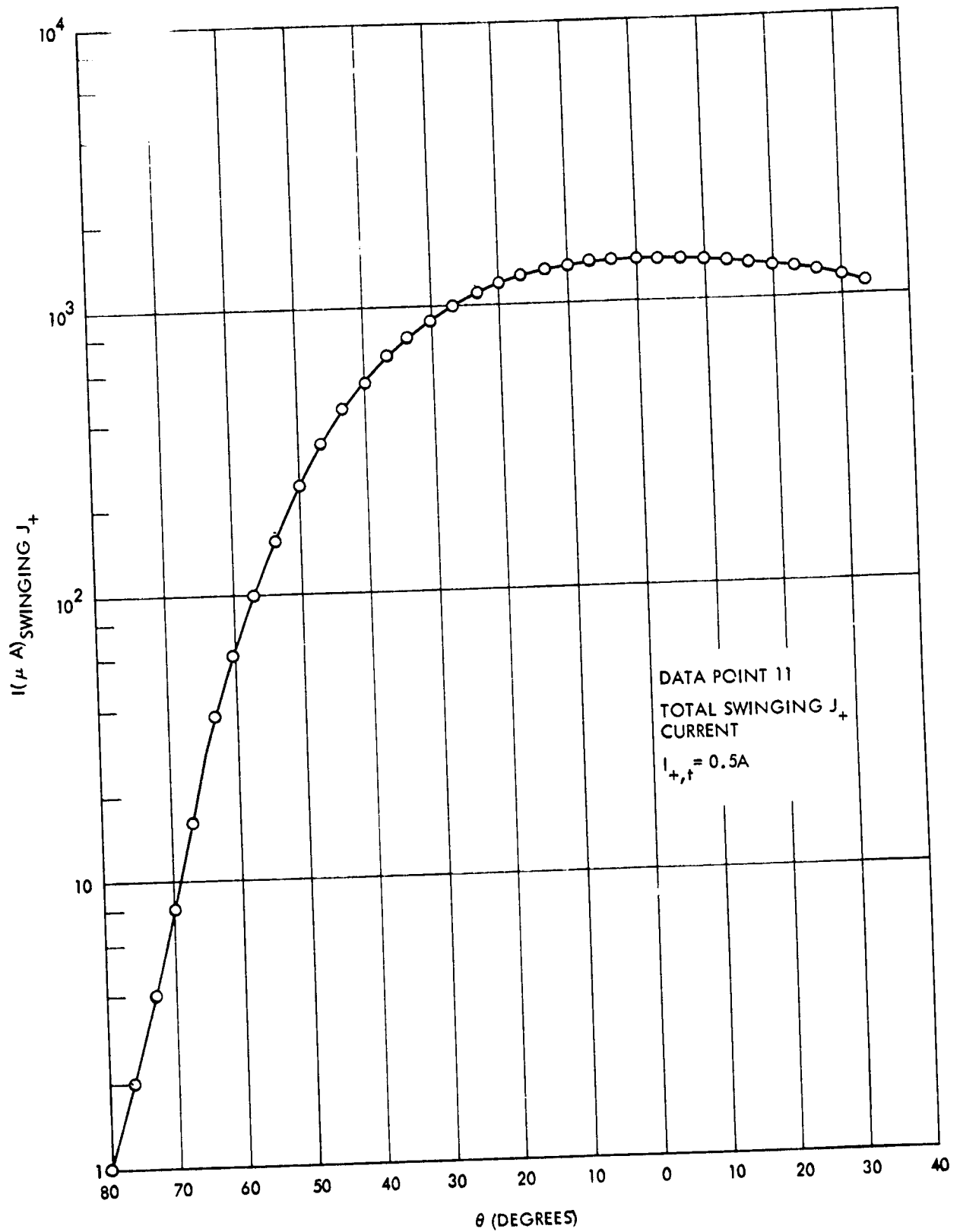


Figure 51. Swinging  $J_+$  Total Ion Current as a Function of  $\theta$  for Engine Operation Data Point 11.

0.5 amperes. (Additional data curves from this probe are in the Engine Operation Data). Outside of a central, and comparatively uniform, region from  $\theta = 0^\circ$  to  $\theta \sim 30^\circ$ , ion flux falls off as  $\sim \exp(-K\theta)$ . Two aspects of this data should be noted. The first of these is that the probe mounting arm length has been set at a comparatively short value so that the probe may be rotated to  $\theta = 90^\circ$  without collision with testing chamber walls. Because of this short arm length, the finite width of the plasma thrust beam appears as an additional angular spread. The true thrust ion divergence is, thus, less than that indicated by the  $\theta = 0^\circ$  to  $\theta = 30^\circ$  figure above. A second important aspect to the probe data is that total ion current signals are largely dominated by low energy charge exchange ions at large divergence angles. The value of K, thus, in the  $\exp\{-K\theta\}$  formulation given above is not readily apparent from total ion current measurements, and retarding potential analyses of the probe currents are required to determine the hard ion current component. These retarding potential analyses will suffer signal-to-noise problems because the hard ion currents are minute and occur in the presence of large quantities of lower energy ions.

Figures 52 and 53 illustrate the total ion current and low energy and high energy components as a function of  $\theta$  for a nominal 2.0 ampere ion thrust beam. The total current and soft ion current are given in Figure 52, while Figure 53 illustrates the hard ion component. The illustrated case is Engine Operation Condition 19, (see Table 3), a minimum decel condition (accelerator grid potential of  $-0.3$  kV), which has been shown (by the 4"  $J_+$  probe data) to reduce the high angle high energy ion flux. Two final examples of Swinging  $J_+$  probe data are given in Figures 54 and 55. Shown there are the hard ion currents as a function of  $\theta$  for 1.0 ampere ion thrust beams. Figure 54 is a minimum decel condition (Engine Point 22) while Figure 55 illustrates a nominal ( $V_g = -0.5$  kV) decel condition. A comparison of the curves demonstrates that the minimum decel condition has resulted in a reduction of hard ions at high angles.

#### 6.4 Testing Chamber Ambient Pressure Effects

Section 4.2 and Figures 9, 10, and 11 have discussed and illustrated ambient pressure effects as they tend to alter the measurements

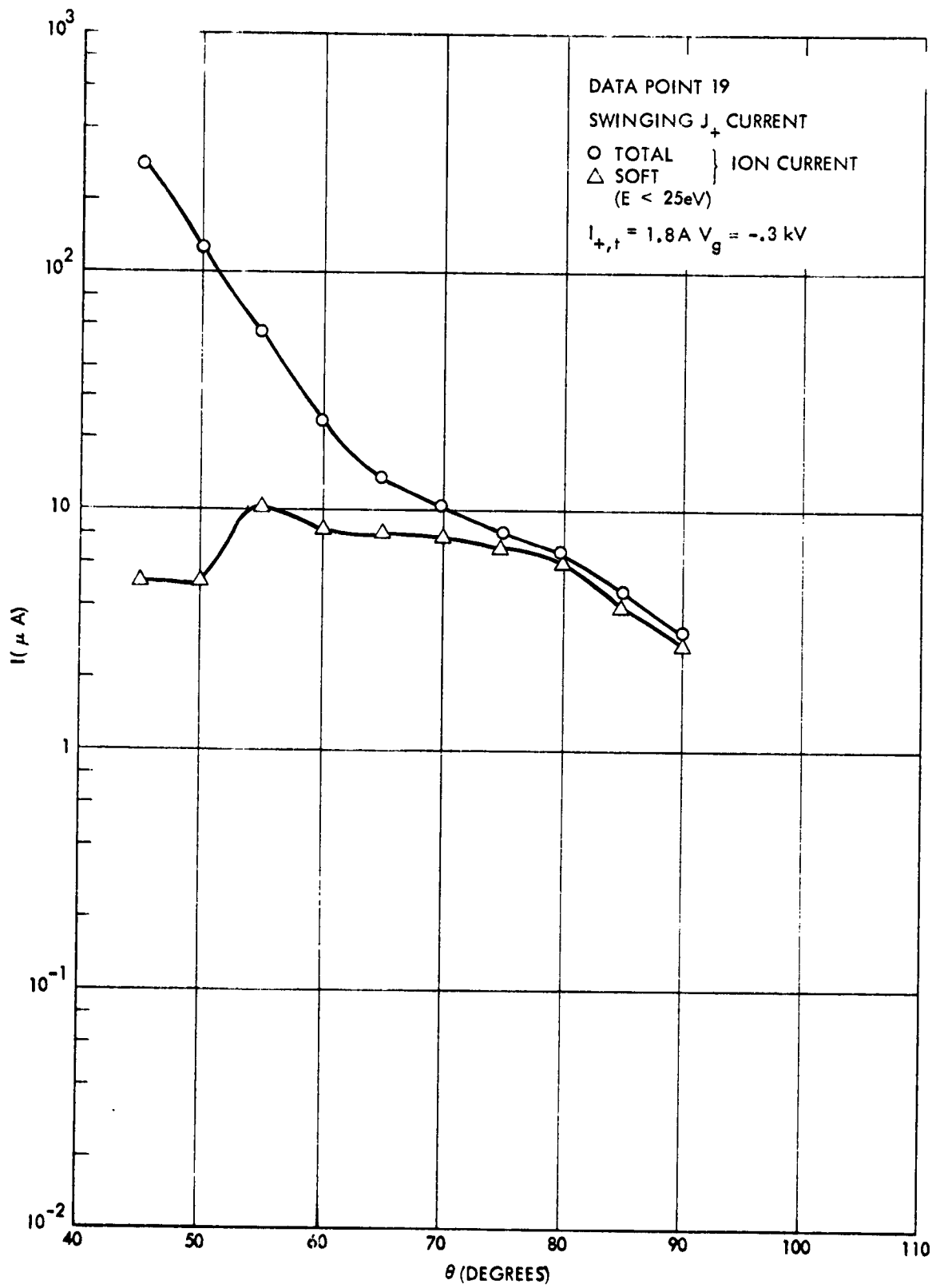


Figure 52. Swinging  $J_+$  Total Ion Current and Soft Ion Component as a Function of  $\theta$  for Engine Operation Data Point 19 (Minimum Decel Condition).

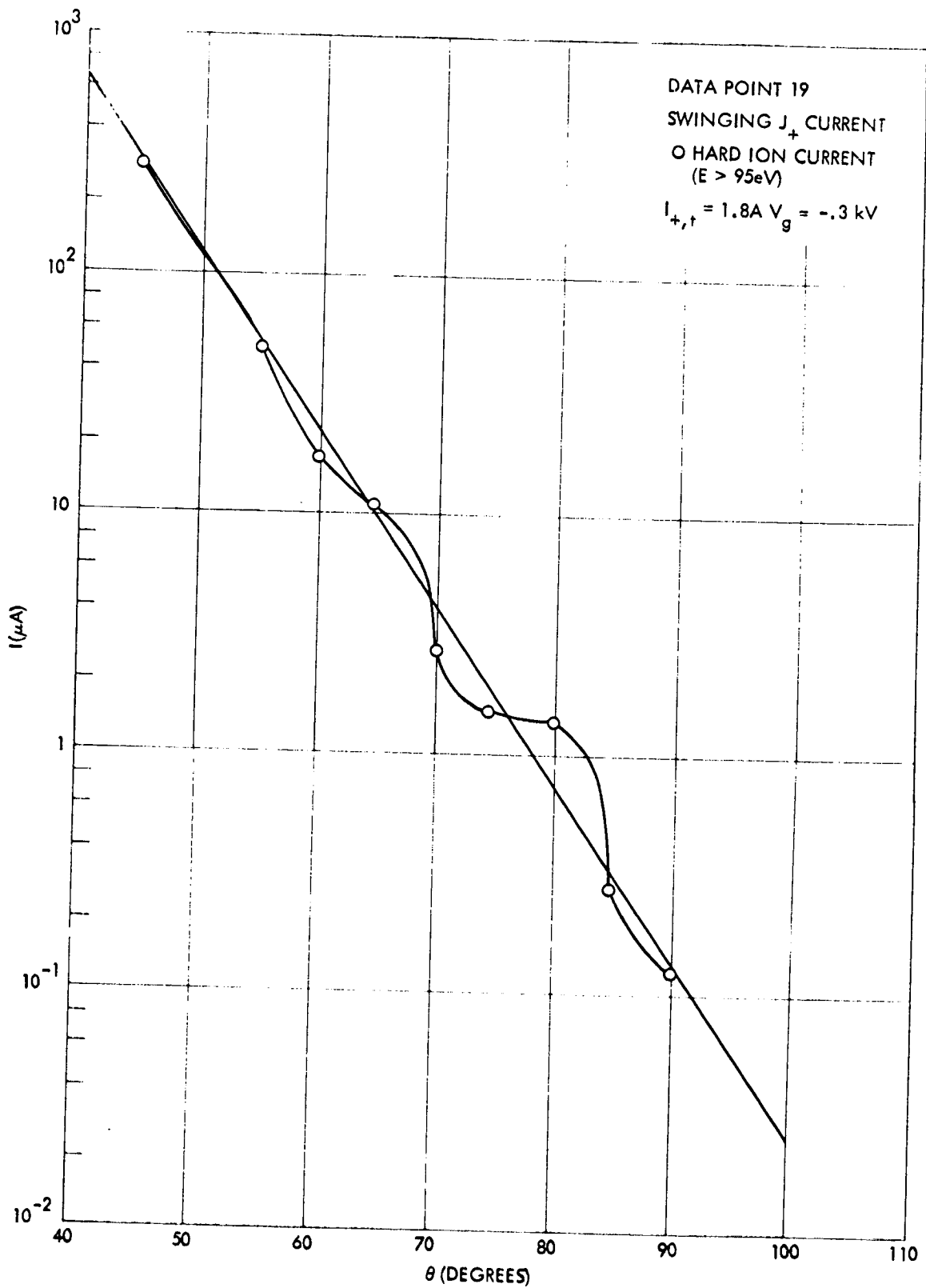


Figure 53. Swinging  $J_+$  Hard Ion Current as a Function of  $\theta$  for Engine Operation Data Point 19 (Minimum Decel Condition).

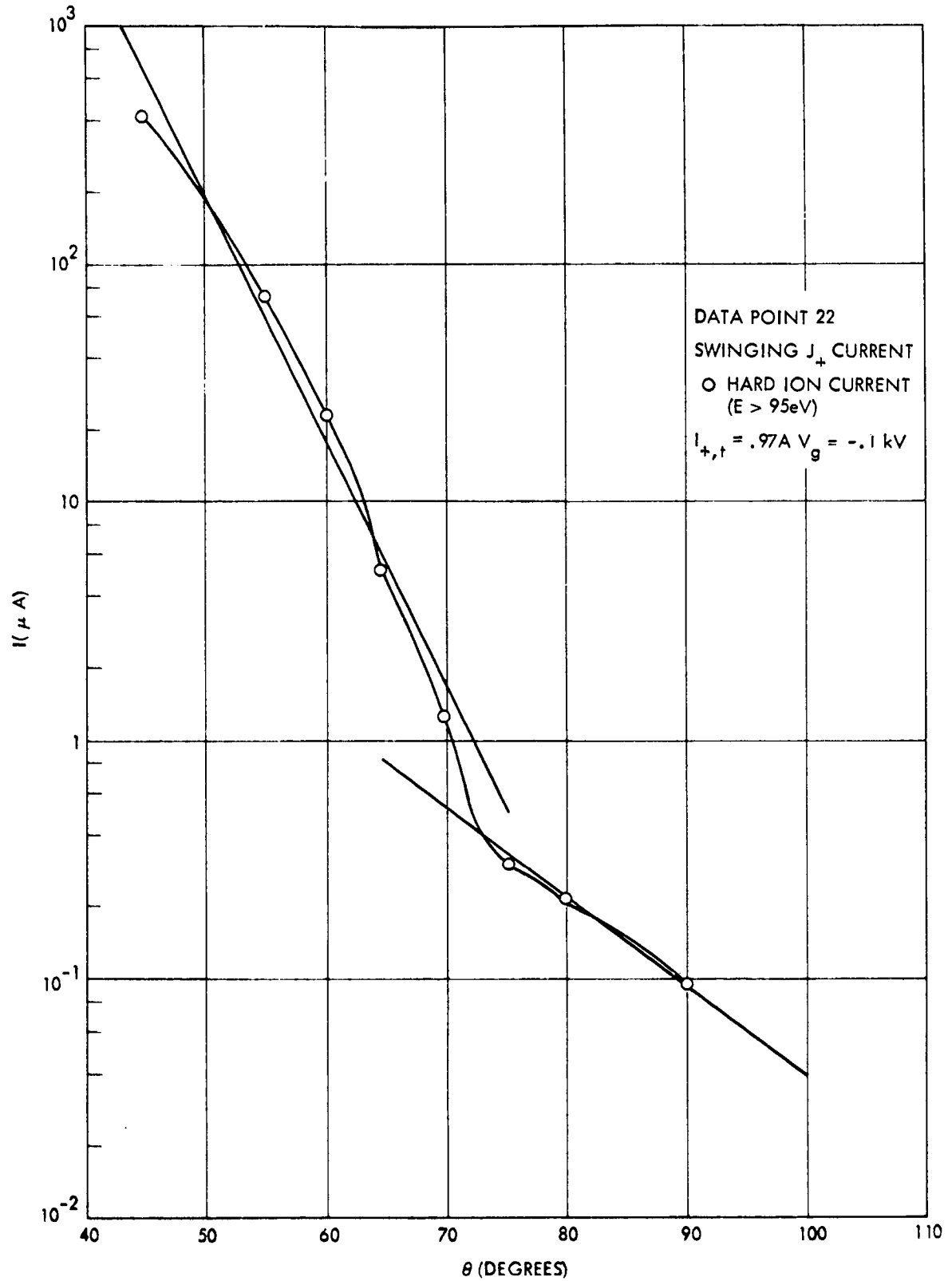


Figure 54. Swinging  $J_+$  Hard Ion Current as a Function of  $\theta$  for Engine Operation Data Point 22 (Minimum Decel Condition).

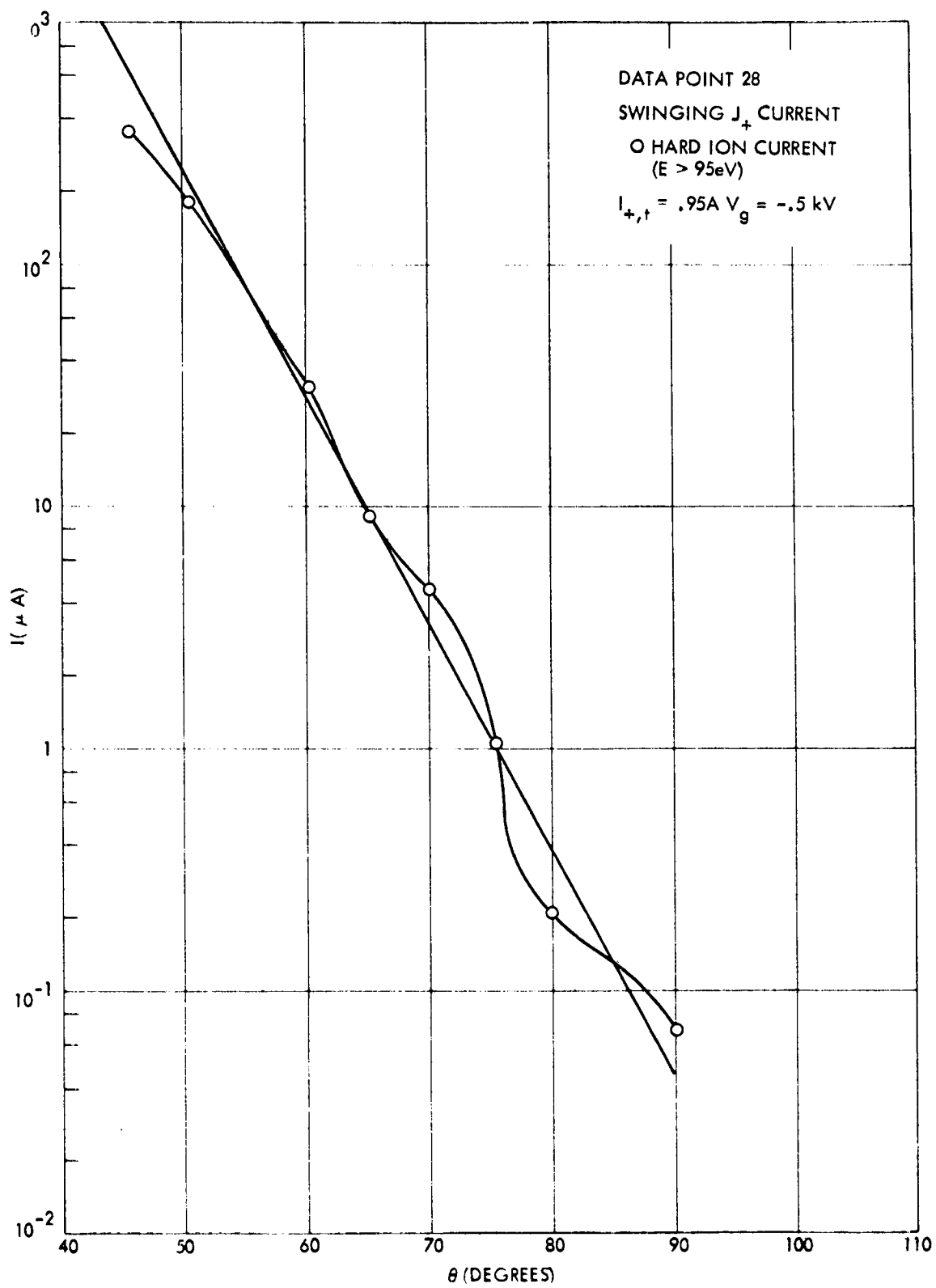


Figure 55. Swinging  $J_+$  Hard Ion Current as a Function of  $\theta$  for Engine Operation Data Point 28 (Nominal Decel Condition).

of low energy ions. The presence of the testing chamber gas also causes alterations in high energy ion flux at high divergence angles. Figure 56 illustrates these pressure effects for high angle hard ions. While these effects are generally not large, it is possible that some of the remaining signals near  $\theta \sim 90^\circ$  (see, for example Figures 53 and 54) are the results of ambient gas which diffuses with the screen grid-to-accelerator grid interspace and causes a "pressure effect" Group II ion signal. These effects will be discussed further in Section 7.

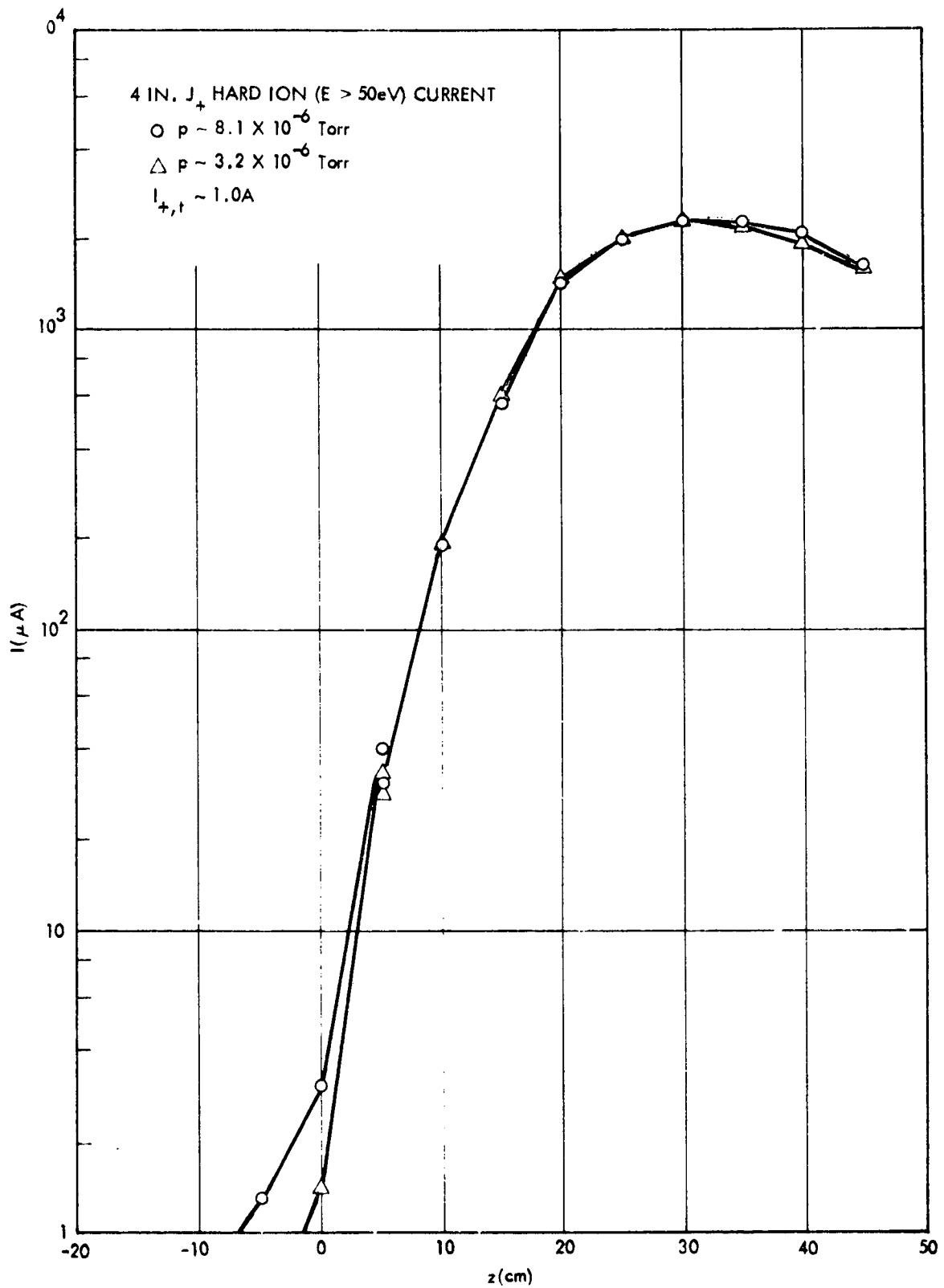


Figure 56. Energetic Ion Current in the 4"  $J_+$  Probe as a Function of Axial Distance,  $z$ , for Two Testing Chamber Conditions for a 1.0 Ampere Thrust Beam.

## 7.0 HIGH ENERGY HIGH ANGLE ION FLUX MODELING

### 7.1 General Considerations

Analyses and modeling of high energy ion flux will not be concerned with small divergence angle ions. The calculation of ion trajectories for the bulk of the Group I ions has received extensive treatment elsewhere and will not be discussed further here. The specific concern of this section is the hard ion flux for divergence angles above  $45^\circ$ , since it is these high divergence particles that create the greater part of thruster/spacecraft integration problems.

Because of the low levels of hard ion signal currents at high angles and because of the comparatively high fluxes of Group IV ions in these regimes, the retarding potential analyses cannot be carried out over the entire range of possible ion energies. Instead, the "hard" ion current is defined as those ions possessing in excess of 100 eV and the calculations of hard ion flux deposition patterns will be based upon ion flux measurements made at  $\sim 100$  volts retardation. Even though the retardation voltage in the measurements has been set at a level which is small compared to screen grid potential, it is felt that the ions still present in the cup for this retardation setting possess energies, in general, significantly above 100 eV.

### 7.2 Hard Ion High Angle Flux as a Function of Accel-Decel

Section 6.3 has discussed the variation of the hard ion flux at high angles as screen grid potential and accelerator grid potential varied. (See figures in Section 6.3 and also 4.5). The effects are clearly evident, particularly for minimum decel conditions.

It will be advanced here that the bulk of the hard ions seen at high angles are Group II ions, have resulted from a charge transfer in the screen grid-to-accelerator grid interspace, and have probably been subjected to comparatively high decel-accel (that is, their energy as they pass through the accelerator grid plane is significantly above the final energy the ions possess as they move into the neutralized thrust beam region).

To examine the comparative regions of accel-decel ratio in the interspace between screen and accelerator grids, as a function of accelerator and screen grid potentials, the first assumptions are that potential in this region is described by space charge limited flow ( $\vec{E} = 0$  at  $x = 0$ , the screen grid location) and that the planar Child-Langmuir relation holds. The use of  $x$  as the distance variable here, instead of the  $z$  notation used for axial distance in the parabolic core exponential wing model (Eqs. (10) and (11)), is for convenience in the sign of the variable and to avoid confusion over the previously chosen zero ( $z = 0$  at the accelerator grid). For  $x = 0$  at the screen grid,  $x = x_0$  at the accelerator grid, and planar space charge limited ion flow in the intervening space, potential is given by

$$V(x) = V_s - (V_s + V_g) \left(\frac{x}{x_0}\right)^{4/3} \quad (26)$$

where  $V_s$  is screen grid potential and  $V_g$  is the magnitude of the accelerator grid potential. Using the definition of decel-accel ratio as a function of  $x$  as

$$\Gamma_a(x) = \frac{V(x) + V_g}{V(x)} \quad (27)$$

leads to

$$\Gamma_a(x) = \frac{1 - \left(\frac{x}{x_0}\right)^{4/3}}{\frac{V_s}{V_s + V_g} - \left(\frac{x}{x_0}\right)^{4/3}} \quad (28)$$

For  $x = 0$ , Eq. (28) reduces to the conventional form of decel-accel ratio (i.e.  $(V_s + V_g)/V_s$ ). The value of  $x$  for which  $\Gamma_a(x) \rightarrow \infty$  is denoted as  $x_{crit}$  where

$$x_{crit} = x_0 \left(\frac{V_s}{V_s + V_g}\right)^{3/4} \quad (29)$$

For  $0 < x < x_{crit}$ , charge transfer produces a Group II ion, capable of escape into the thrust beam. For  $x > x_{crit}$ , escape is energetically forbidden, the ion is designated as "Group III", and is collected at the accelerator grid.

Using Eq. (26),  $V_s = 1.1$  kV and  $V_g = .1, .5, \text{ and } .7$  kV, the decel-accel ratio has been computed as a function of  $x$  and is illustrated in Figure 57. It is apparent from these curves that the decel-accel ratio of Group II ions formed in Case 1 (minimum decel condition) is significantly less than for Cases 2 and 3. For example, at  $x = .5x_0$ ,  $\Gamma = 1.160, 2.075, \text{ and } 2.815$  for Cases 1, 2, and 3. Group II ions formed at  $x = .5x_0$  would be expected, thus, to emerge into the thrust beam with successively larger cones of divergence for each of the cases above. This does not mean that all Group II ions created at a given  $x$  in a given  $(V_s, V_g)$  case emerge with a single divergence angle.

For an actual thruster, the Group II formation at  $x$  in the interval  $dx$ , takes place in a cylindrical volume whose radius is determined by the radius of the thrust ion beamlet at that point of its passage between the screen and accelerator grid. Denoting the outer radius of this beamlet as  $\omega(x)$ , and noting that the Group II ions formed in the cylindrical volume element  $\pi\omega^2 dx$  will be formed at a rate

$$\frac{dn_{+cxII}}{dt} = [J_{+,t}(x)\sigma_{cx}n_{ne}(x)]\pi\omega^2 dx \quad (30)$$

where  $J_{+,t}(x)$  is thrust ion current density at  $x$  (and is probably non-uniform within the radius  $\omega(x)$ ), and  $n_{ne}(x)$  is  $Hg^0$  neutral density at  $x$  from neutrals escaping from the thruster. Using nominal values of  $x_0, F_0, v_{o,th}, \sigma_{cx}, \omega^2$ , and  $J_{+,t}$  leads to a total charge exchange formation rate of Group II ions of from  $10^{-3}$  to a few times  $10^{-4}$  of  $I_{+,t}$ . The total formation of Group II ions for a 1 ampere thrust beam would range thus from a few hundred microamperes to approximately 1 milliampere. Of that total production, those ions formed on the axis of the beamlet will probably emerge without significant divergence. Group II ions formed at the edge of the beamlet, and for which there is a significant departure of  $\Gamma_a(x)$  from unity will be deflected through large angles in the resulting passage through the accelerator grid and into the thrust beam. It is clearly apparent that regions of significant decel-accel are more prevalent in Cases 2 and 3 than in Case 1 and that some of the Group II formed at these  $x$  values will emerge at high angles.

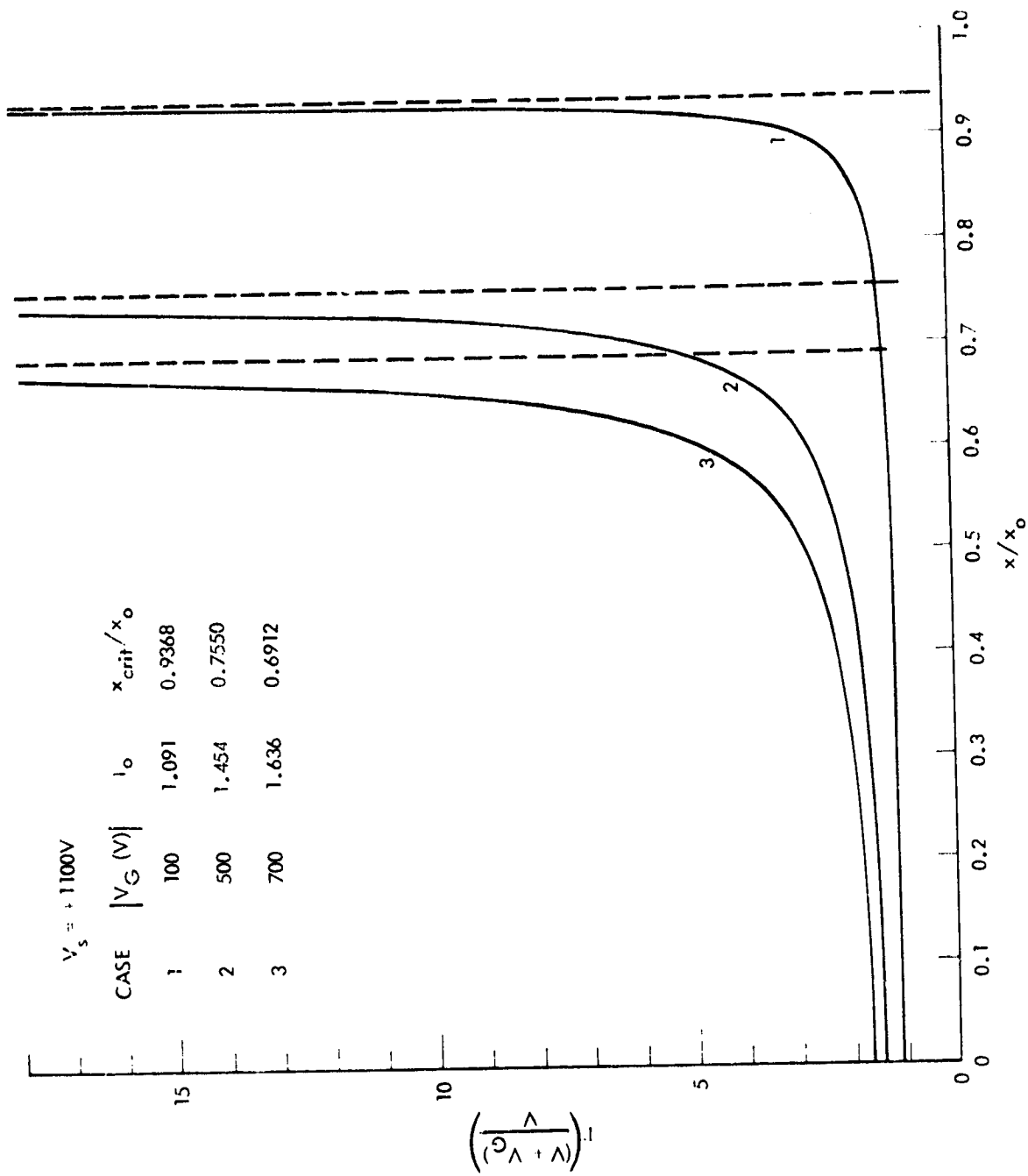


Figure 57. Computed Decel-Accel Ratio as a Function of Distance  $x$  for Screen Grid to Accelerator Grid Spacing of  $x_0$  and for Selected Values of Screen and Accelerator Grid Potentials.

The treatment above is acknowledged to be only an approximate one. To improve this description would require the use of the computer generated potentials in the regions from the screen grid on into the thrust beam, taking into account thrust ion space charge density and a complete description of screen and acceleration grid geometry. In addition, more accurately modeled  $n_{ne}$  is required, including, perhaps, some inclusion of backstreaming neutrals from the testing chamber. Even with these modeled elements complete, the calculation of Group II trajectories still appears as difficult and possibly inaccurate because of the comparatively reduced ion energy and the consequent severe perturbations on the trajectory by all of the electric field patterns present in the screen to accelerator grid interspace and in the sheath region from the accelerator grid to the thrust beam plasma. A reliance upon experimental measurements rather than analyses would appear as the most promising approach.

A final aspect of the Group II calculations to be discussed here is the final energy of the Group II ions which have encountered significant decel-accel effects and which, presumably, are the Group II ions seen at high divergence angles. If it is considered that  $\Gamma_a > 2$  leads to significant divergence, then the maximum Group II ion energy (for high divergence angle) in Case 1 is only 100 eV, while in Cases 2 and 3 it would be 500 eV and 700 eV. Since the ion sputtering ratio is a rapidly rising function of ion energy in this energy regime, the sputtering damage per Group II ion at high angles will also rise rapidly in moving from the conditions of Case 1 to the conditions of Case 3. There are, thus, multiple benefits which are obtained through the use of a minimum decel. Going to minimum decel diminishes the interval  $\Delta x$  in  $x_0$  for which the higher  $\Gamma$  values are obtained, and, even within those now diminished intervals, has lowered values of the average of  $\Gamma_a$ ,  $\langle \Gamma_a \rangle$ . Finally, those Group II ions which do encounter a  $\Gamma_a$  sufficiently high to cause severe divergence, emerge into the thrust beam with energies of only  $(\Gamma_a - 1)^{-1} |v_g|$ .

### 7.3 Calculated Deposition Contours for Hard Ions

To assess the possible damage to spacecraft surfaces under hard

ion deposition, it has been found convenient to employ  $\epsilon$  contours, where the units of  $\epsilon$  are in  $\text{cm}^{-2}$  and denotes the flux of a given particle specie (in amperes/ $\text{cm}^2$ ) divided by the thrust beam current. Using the  $\epsilon_+$  notation, the total hard ion deposition per square centimeter during a thrust mission in which a total of  $N_{+,t}$  thrust ions are released is  $\epsilon_+ N_{+,t}$ . Earlier discussion of allowable deposition have noted that safe spacecraft surface placement will generally require  $\epsilon < 10^{-8} \text{cm}^{-2}$ .

To evaluate the  $\epsilon_+$  contours for hard ions, the Swinging  $J_+$  probe data on hard ion flux is used to determine the angular distribution function. For convenience in the calculations, it will be assumed that all hard ions emerge from  $r = z = 0$ . This "point source" approximation will be generally valid for most of the relevant regions in  $r$  and  $z$  for spacecraft surface placement.

Since the Swinging  $J_+$  arm length is only several times the engine radius, distributed source effects will be present. The use of the Swinging  $J_+$  flux data and the assumption of point source emission from the thruster will result in conservative, upper bound, estimates of the  $\epsilon$  contour placement.

Examples of  $\epsilon_+$  contours for hard ions are given in Figures 58, 59, 60, 61, and 62. Figures 58 and 59 are Engine Operation Conditions 2 and 19 and are 2 ampere thrust beams under nominal and minimum decel conditions. While the use of minimum decel makes surface placement somewhat easier by causing a given  $\epsilon$  contour to move inward toward the thrust axis, it should be noted that surface placement outside of the  $10^{-8} \text{cm}^{-2}$  contour clearly causes surface placement either at high divergence angles near the thruster or at comparatively large axial and radial separation distances. Figures 60, 61, and 62 illustrate the  $\epsilon_+$  contours for a beam of 1 ampere under accelerator grid voltage conditions of .1, .5, and .7 kV. Again, the inward motion of the  $\epsilon_+$  contours for minimum decel conditions is observed and is desirable, but, again, surface placement outside the  $10^{-8}$  contours requires large angular or spatial separation.

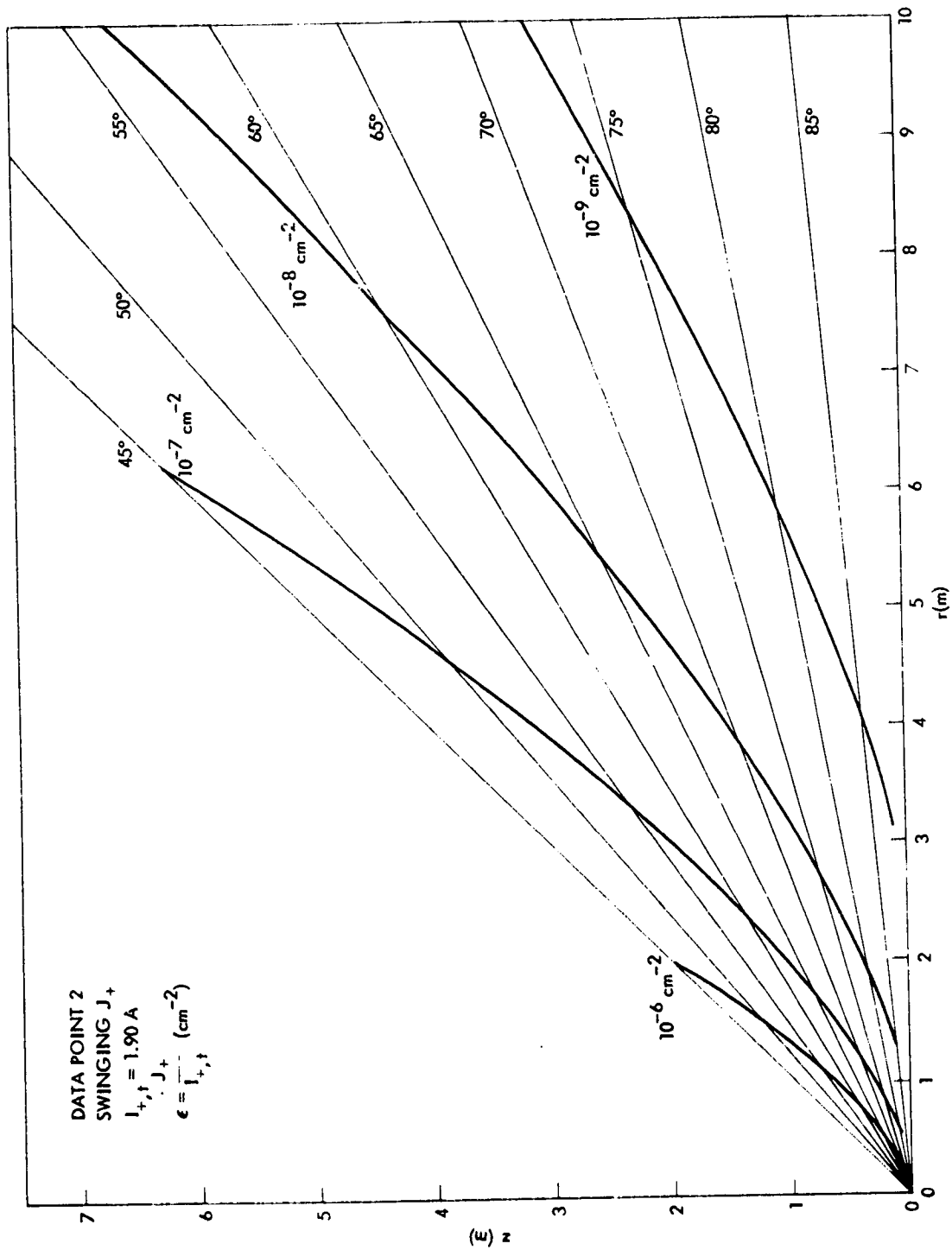


Figure 58. Computed Hard Ion Deposition Contours for  $r$ ,  $z$ , and  $\theta$  from Swinging  $J_+$  Data on Engine Operation Data Point 2 (Nominal Decel).

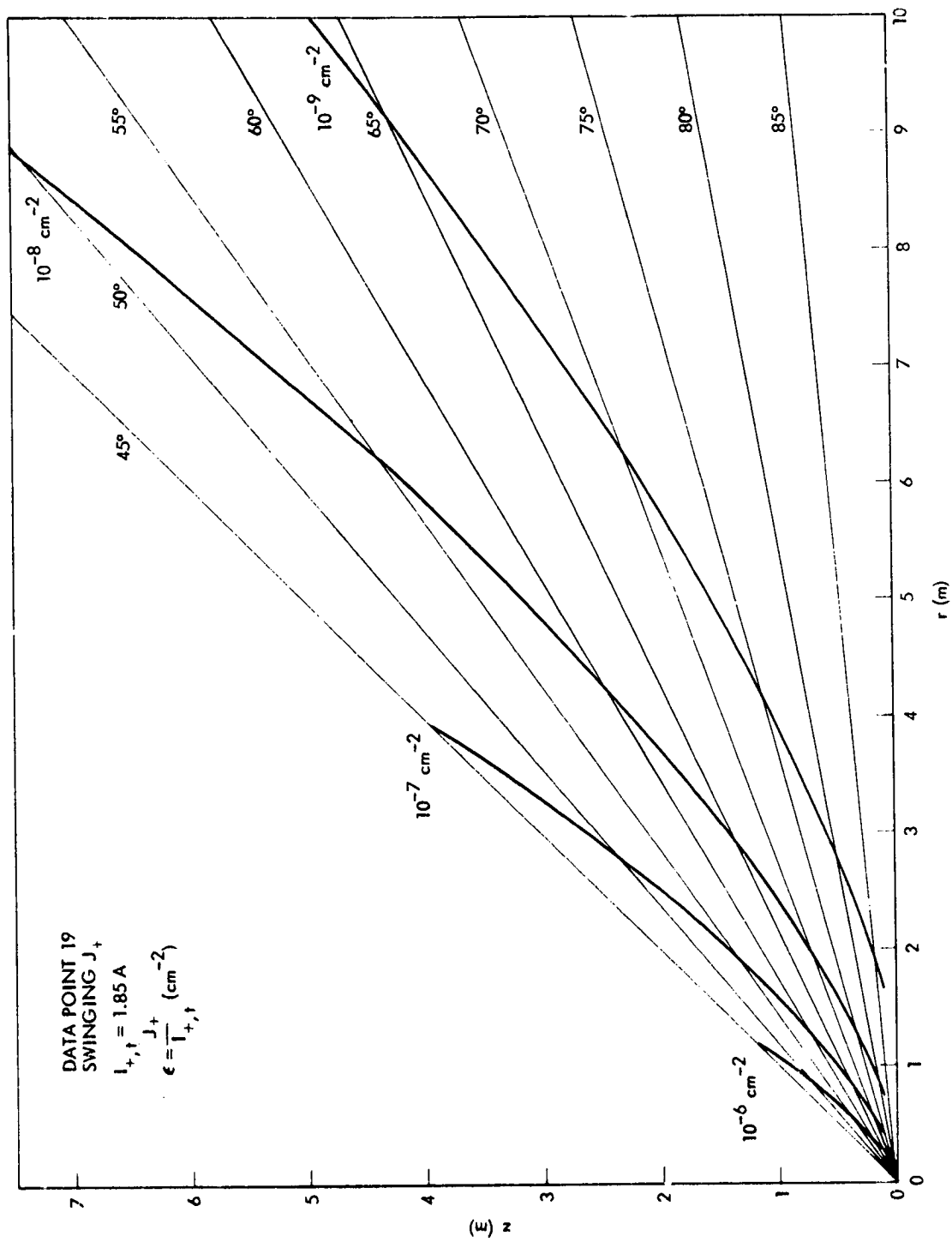


Figure 59. Computed Hard Ion Deposition Contours for  $r$ ,  $z$ , and  $\theta$  from Swinging  $J_+$  Data on Engine Operation Data Point 19 (Minimum Decel).

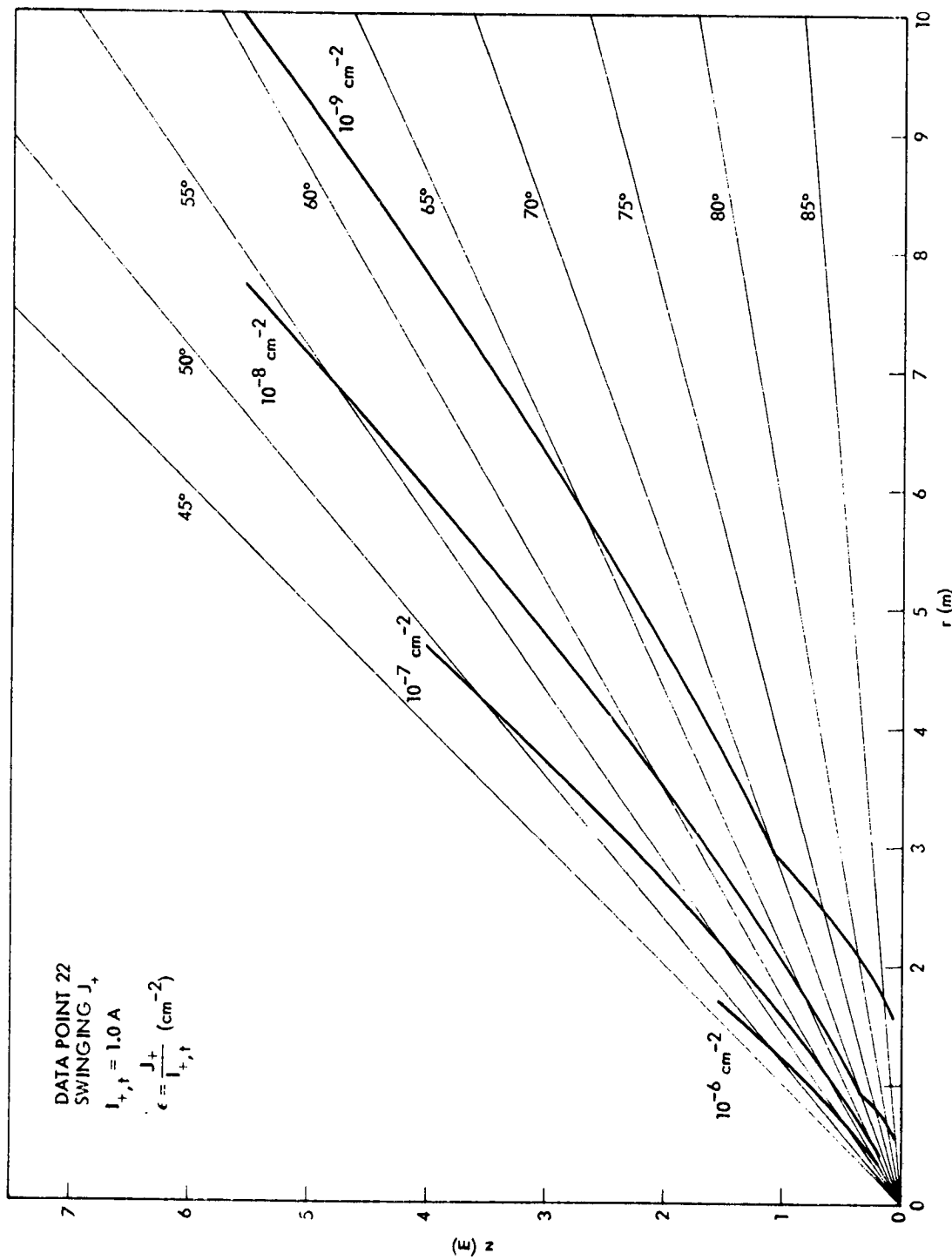


Figure 60. Computed Hard Ion Deposition Contours for  $r$ ,  $z$ , and  $\theta$  from Swinging  $J_+$  Data on Engine Operation Data Point 22 (Minimum Decel).

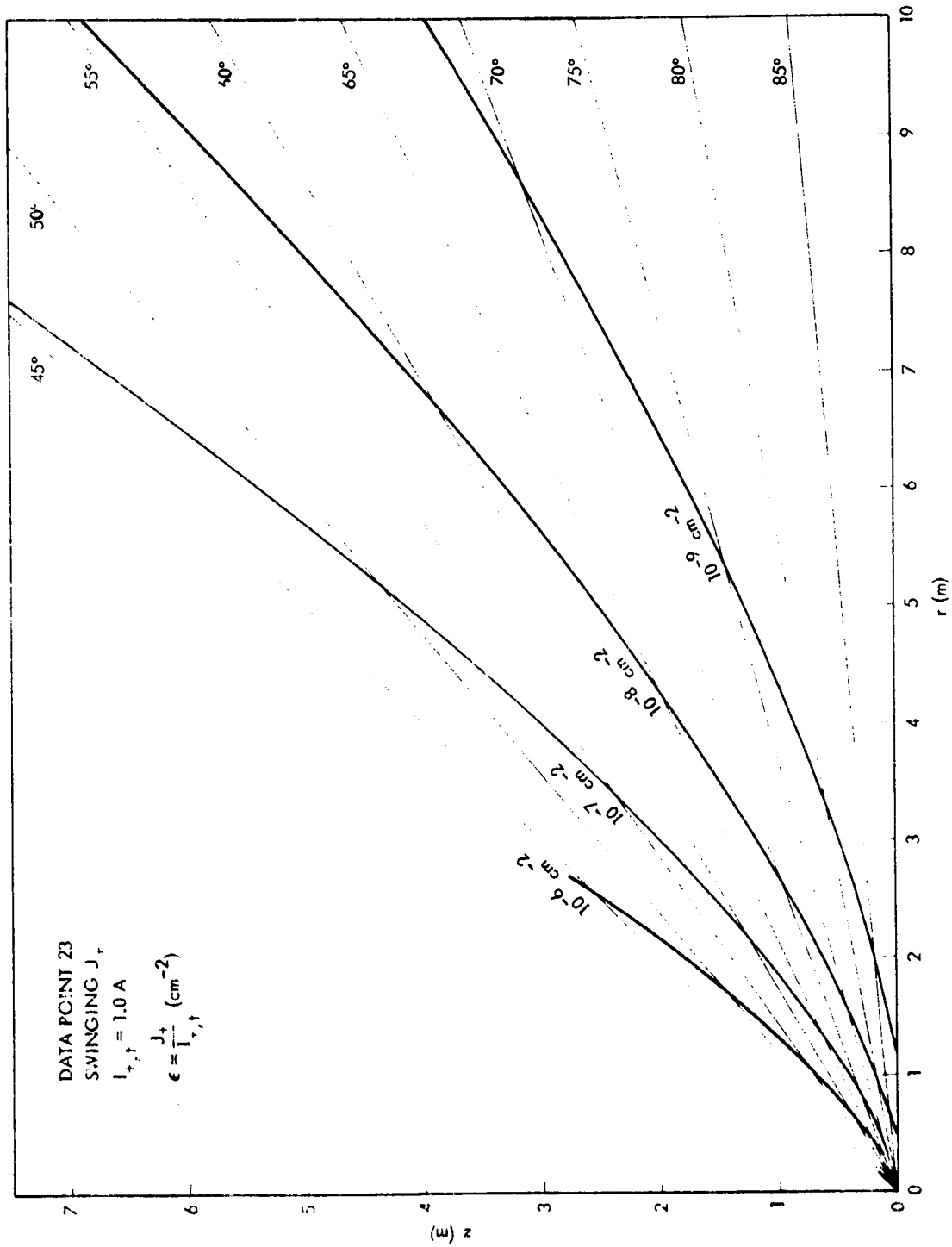


Figure 61. Computed Hard Ion Deposition Contours for  $r$ ,  $z$ , and  $\theta$  from Swinging  $J_+$  Data on Engine Operation Data Point 23 (Nominal Decel).

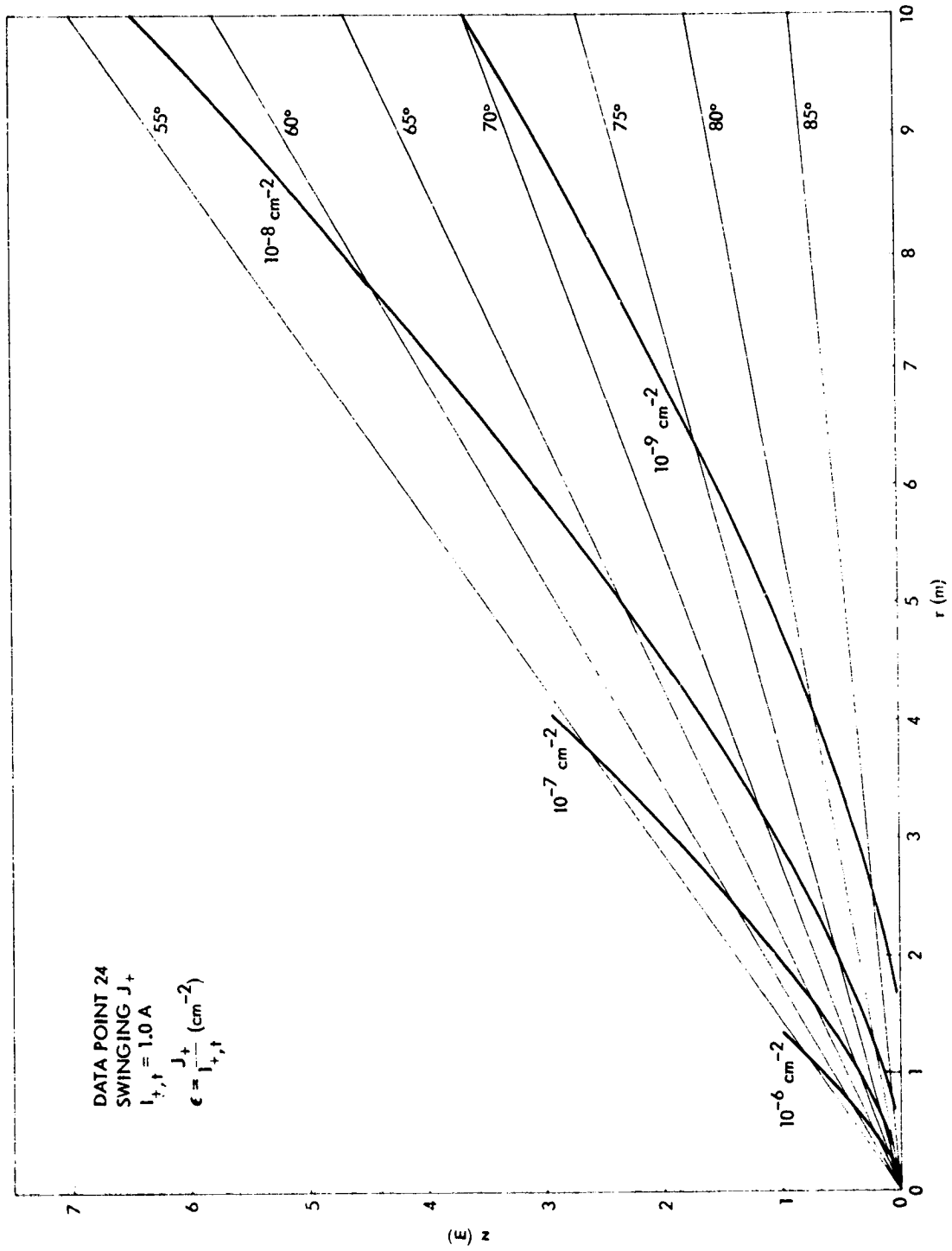


Figure 62. Computed Hard Ion Deposition Contours for  $r$ ,  $z$ , and  $\theta$  from Swinging  $J_+$  Data on Engine Operation Data Point 24 (Increased Decel).

## 8.0 EVALUATION OF THRUSTER IN FLIGHT DIAGNOSIS FROM HIGH ANGLE ION MEASUREMENTS

### 8.1 General Considerations

This section will discuss the use of an ion flux measuring probe as an in-flight diagnosis of thruster operation. Several assumptions will be made. The first of these is that the total information on thruster performance includes measurements of all relevant ion engine voltages and currents, plus the outputs of any temperature measuring sensors. The ion flux determinations, then, are a complement to a second, and extensive, series of "terminal" measurements. A second assumption here will be that the probe is stationary in position. This assumption is introduced to simplify the discussion and to focus attention on diagnostics that are of minimum cost. It has been demonstrated in the success of the SERT II engine test flight that in-flight measurements of the ion beam flux can be carried out with movable Faraday cups and emissive, potential measuring, probes. The principal question remaining, then, is whether meaningful diagnosis can be accomplished with probes of reduced complexity, which leads to the assumed condition of a fixed probe position.

The assumption of a fixed probe position leads immediately to considerations of the erosion of probe surfaces under thrust ion interception. From the discussion of previous sections, it has been advocated that the placement of surfaces should be outside of the  $\epsilon_+ = 10^{-8} \text{ cm}^{-2}$  contour for energetic ions which leads to a requirement for either high angular placement or large radial or small axial separation of the probe surfaces from the  $r = z = 0$  point (at the thruster face center). This advocacy of location outside the  $10^{-8} \text{ cm}^{-2}$  for energetic ions may be overly conservative, since the high angle ions are probably Group II rather than Group I, and, because of reduced energy in Group II compared to the thrust ions, will have lowered values of ion sputtering.

A final aspect to be treated in these general considerations is the focus of the probe diagnosis. Although the probe to be advocated for spacecraft use will possess the capability for several different measurements, the principal interest in the diagnosis will be for Group IV ions, from which engine performance in propellant utilization will be

deduced. The secondary target for the probe diagnosis will be to determine the effectiveness of beam neutralization, and the tertiary goal will be to determine the high angle hard ion flux. This final measurement may be of use in evaluating the in-flight wear-in of the thruster grids. Conclusions as to wear-in effects and hard ion count are only tentative, since the present measurements program has not been directed toward long term alterations in the shapes and magnitudes of the several species of ion plumes from the thruster.

## 8.2 Probe Placement

Probe placement is principally determined by the location of the peak in the genuine Group IV ion flux. From Figure 12 and Figures 14 through 23 (and for a probe similar to the 4"  $J_+$ , see Section 8.3, which follows), the optimum location in  $z$  (for  $r \sim 28$  cm) is in the range from  $\sim 10$  cm to  $\sim 20$  cm. For probe location outside this range, increasing problems will be encountered between laboratory and in-flight results since the regimes of  $z < 10$  cm and  $z > 20$  cm are increasingly dominated by facility effect Group IV ions. Another reason for probe placement in this "plateau" region is that this region, because of its "flatness" (small variations in probe current for variations in  $z$  location) will probably not be subject to probe misinterpretation because of minor changes in the shape of the Group IV ion plume. For locations of the probe near  $z = 10$  cm or for  $z < 10$  cm, the rapid drop-off in probe signal for motion in  $z$  toward  $z = 0$ , leads to a condition of increased sensitivity to plume shape changes as contrasted to the desired measurements of plume magnitude.

A major concern in probe placement is the extent of the energetic ion flux. The erosion of probe surfaces (and possible secondary mass transport and deposition effects) clearly weighs against probe placement at  $z > 20$  cm. It is also not desirable for the Group IV determination to be carried out in the presence of comparatively large Group I and II ion fluxes. An acceptable condition can be equal levels of energetic and soft ion fluxes (these can be accurately separated by retarding potential analyses). These equal levels of hard and soft ions are encountered near  $z = 10$  cm for nominal accel-decel conditions, and near

$z = 20$  cm for minimum decel conditions. The use of a given accel-decel ratio may depend upon many different thruster and mission considerations, and it does not appear advisable to allow plume diagnosis requirements to be the "driver" in this area. Plume diagnosis requirements should be considered in the selection of an accel-decel condition, and, in a self-consistent manner, probe placement will depend upon the selected accel-decel condition. Depending upon many factors which may see some future alteration, it would presently appear that probe placement should be in the range  $10 \text{ cm} < z < 20 \text{ cm}$  (for  $r \approx 28 \text{ cm}$ ). Section 8.3, which follows, will consider probe orientation at the selected location, and probe configurations and capabilities.

### 8.3 Probe Configuration

Section 8.1 has taken the position that the principal focus of the probe measurements will be upon the magnitude of the charge exchange ion flux, from which (using Eq. (18) and appropriate calibration constants) can determine propellant utilization (essentially term  $F_0$  in Eq. (18)). For these Group IV flux determinations to be as insensitive as possible to other effects, such as small alterations in plume shape or in charge exchange ion trajectory, it is essential that the probe be a "total flux" measuring probe, that is, that the probe construction and orientation be such as to have a large solid angle for charge exchange ion trajectory acceptance. For this reason it is recommended that the probe have a configuration similar to the 4"  $J_+$  probe, with the orientation of the surface normal of the collector such that it passes through the  $r = z = 0$  point at the center of the thruster face.

Since both hard and soft ions will be directed into the cup and since determinations of both ion species are of interest, the probe should be a multi-gridded probe (at least two grids are required) capable of carrying out a retarding potential analysis of the incoming ion flux. This requires an electronics package capable of applying a varying (positive) bias on the retarding potential grid from 0 volts to, at least, +100 volts. The outer grid must be negatively biased to prevent drainage of electrons from the plasma plume to the inner, retarding potential, grid. A third grid may also be useful as a means of

suppressing secondary electrons and photoelectrons from the collector surface. This third grid, between the retarding potential grid and the collector surface, would be biased negatively with respect to spacecraft ground. The collector surface would be, essentially, at spacecraft ground potential.

A final useful output of the probe (in addition to soft and hard ion fluxes) is plasma thrust beam potential. For a probe of the size recommended, and for the expected flux magnitudes, the probe can be used effectively for floating potential measurements with only moderate values of isolation impedance. The floating potential measurements would be used, in turn, to determine in-flight effectiveness of the thrust beam neutralizer. In the floating potential mode of operation, all probe components (case, outer grid, RPA grid, inner grid, and collector) are connected together and are electrically isolated from spacecraft ground by an isolation resistance of at least 10 megohms.

Table 5 presents recommended probe configuration, size, and placement.

Table 5. Configuration Details, Size, and Placement of Ion Thruster Plume Diagnosis Probe.

Probe Location	$10 \text{ cm} \leq z \leq 20 \text{ cm}$ $r \leq 30 \text{ cm}$
Probe Orientation	Collector surface normal passes through $r = z = 0$
Collector Area	$50 - 100 \text{ cm}^2$
Grids	3
Outer Grid Potential	-10 to -20 volts (fixed)
Retarding Grid Potential	0 to +100 volts (variable in steps)
Suppressor Grid Potential	-10 volts (fixed)
Collector Measurement Impedance	$10^3 \text{ } \Omega$ to $10^8 \text{ } \Omega$ (variable in decade steps)
Configuration for Floating Potential Determinations	All probe elements (connected together and isolated from spacecraft ground by at least $10^7 \text{ } \Omega$ )

#### 8.4 Multiple Thruster (Cluster) Effects

The measurements program carried out in the 5' x 11' facility has determined the plume characteristics of only a single ion engine. From Section 5.4, it should be expected that the presence of a thruster and its charge exchange plasma plume can be affected by the presence of a second thruster, and accompanying plasma plume. The extent and particular characteristics of these pile-up effects on the Group IV ion trajectories are not known at present and should be an element in future beam diagnostics programs. Because of facility effect ion production, and because the operation of multiple thrusters will create additional pumping problems for the test facility, these "cluster" effect measurements should be carried out in the largest and highest pumping speed facilities possible.

## 9.0 SUMMARY AND RECOMMENDATIONS

The ion flux from a 30 cm ion thruster has been examined for Group I, Group II, and Group IV ion species. The presence of the testing facility boundaries has no significant effect on Group I and Group II ions. The Group IV ion measurements, however, are subject to influence by facility effects. By reducing chamber pressure into the range below 4  $\mu$ Torr, the principal features of the charge exchange ion plume may be determined. Facility effects are still present at these chamber pressures, however, and even further reductions in chamber pressure are recommended. Depending upon point of observation, direction of observation, or range of ion energy, measurements may be influenced by the ambient  $Hg^0$  density, even for the highest pumping speeds and the lowest possible chamber pressures. Variation of facility pressure and correlation of facility pressure with observed plume fluxes can be used as an aid to identifying possible facility effects. This method is not precise, however, unless an accurate in situ determination of all partial pressure contributions is made at the given test facility total pressure.

The  $Hg^+$  charge exchange ion plume has been investigated under a series of engine operation conditions. For thrusters with discharge conditions set for efficient ionization, the Group IV flux scales as the thrust ion current,  $I_{+,t}$ . These results necessarily imply an improvement in propellant utilization as thrust ion current is increased. Since propellant utilization efficiency varies as thrust ion current varies, these experiments determine the results of an explicit variation in  $I_{+,t}$  and an implicit variation in propellant utilization. The charge exchange production rate was also examined as an explicit function of propellant utilization by holding  $I_{+,t}$  fixed and varying the emission current in the bombardment discharge (which varies propellant utilization). Charge exchange ion flux increased for diminished propellant utilization, as expected from the charge exchange ion production model. The experiments, however, did not examine deliberately "spoiled" utilization conditions (defined here as a significant lowering of propellant utilization away from the values obtained for normal engine operation at a given thrust ion current). Since a major possible use of Group IV measurements in space should be to in-flight monitoring of propellant utilization, it is recommended

that additional Group IV measurements be made under bombardment discharge conditions leading to deliberately "spoiled" utilization efficiency.

The charge exchange ion plume shape has not exhibited any major variations as screen grid potentials and accelerator grid potentials move through relevant ranges. Changes in discharge bombardment voltage (for constant discharge power) have not revealed variations in Group IV plume shape. Both shape and magnitude of the Group IV plume were invariant to alterations in neutralizer heater condition (within the range of variation utilized).

The results above appear to confirm analytical models of charge exchange ion production and deposition. In the computed charge exchange ion trajectories, the governing situation is the shape of the major portion of Group I ions. If this modeled beam expands, the Group IV plume appears to have a counter motion, while a narrowing Group I beam leads to an expanded Group IV plume.

The total deposition pattern of these Group IV ions has not been computed. Such computations are possible, but will require additional specification of model parameters if results are to be precise.

The Group I and Group II ions have been examined in the divergence angle range from  $0^\circ$  to  $90^\circ$ . The cutoff in Group II abundance near  $90^\circ$  is more abrupt for reduced deceleration, and several important reductions in hard ion deposition effects can be obtained through the use of a minimum decel condition. These factors should be included with other engine operation data in the ultimate choice of thruster operation parameters.

The recommended properties for an in-flight diagnostic probe have been given (Table 5) and include retarding potential analysis capability, electrical floating capability (for measurements of potential in the neutralized thrust beam), and a broad range of acceptance angles for ion trajectories. The location of this probe should be at high angles ( $\sim 60^\circ$  to  $\sim 80^\circ$ ), with emphasis on Group IV  $\text{Hg}^+$  measurements, but with a capability, also, for Group II identification.

The measurements of beam efflux have taken place over only a limited period of thruster operation so that there is, as yet, no firm evidence for the plume shapes and magnitudes for ultimate, "run-in" conditions. It is recommended that some of the long duration thruster test runs have these diagnostic tests performed during the total period of beam release. It is also recommended that plume measurements for single thrusters and groups of thrusters be carried out in the largest size and highest pumping speed chambers available to more clearly define the cluster effects and to permit determinations, over broader regions of parameter space, of the genuine engine effluxes.

#### 10.0 ACKNOWLEDGEMENTS

The ion thruster used in these measurements was supplied by NASA/Lewis Research Center. Discussions of thruster operation, of the results from the plume measurements, and of possible plume behavior were held with the NASA Program Manager, V. K. Rawlin, and with R. C. Finke and D. C. Byers of NASA/LeRC. The operation of the ion thruster at TRW was under the direction of E. C. Ashwell, who also fabricated and installed the diagnostic probe array. Data analysis was carried out by T. Sato. The ion trajectory computer program was developed by D. K. Hoffmaster. R. K. Cole examined the modeled and observed thrust ion plumes for agreement.

## REFERENCES

1. "Solar Electric Propulsion/Instrument/Subsystem Interaction Study", J. M. Sellen, Jr., R. K. Cole, R. F. Kemp, D. F. Hall, and H. Shelton, Final Report NAS 2-6940, TRW 22878-6007-RU-000, 30 March 1973.
2. "Measurement of Ion Thruster Exhaust Characteristics and Interaction with Simulated ATS-F Spacecraft", R. Worlock, G. Trump, J. M. Sellen, Jr., and R. F. Kemp, Presented at the AIAA 10th Electric Propulsion Conference, Lake Tahoe, Nevada, October 31 - November 2, 1973, AIAA Preprint 73-1101.
3. "Charged Particle Measurements on a 30-CM Diameter Mercury Ion Engine Thrust Beam", J. M. Sellen, Jr., G. K. Komatsu, D. K. Hoffmaster, and R. F. Kemp, TRW 25781-6001-RU-00, 1 April 1974.
4. "Ion Thruster Study", Final Report, Contract 953836, NAS 7-100, TRW 26203-6002-RU-00, May 20, 1975. See also: "Charge Exchange Ion Formation and Motion in Mercury Ion Engine Thrust Beams", G. K. Komatsu, R. K. Cole, D. K. Hoffmaster, and J. M. Sellen, Jr., Presented at the AIAA 11th Electric Propulsion Conference, New Orleans, La., March 19-21, 1975, AIAA Preprint 75-428.
5. "Material Deposition Processes for North-South Stationkeeping Ion Thrusters on Three Axis Stabilized Spacecraft", J. M. Sellen, Jr., R. K. Cole, and G. K. Komatsu, Presented at the JANNAF Propulsion Conference, Anaheim, California, 30 September - 2 October, 1975.
6. "Measurement of Beam Divergence of 30-CM Dished Grids", R. L. Danilowicz, V. K. Rawlin, B. A. Banks, and E. G. Wintucky, Presented at the AIAA 10th Electric Propulsion Conference, Lake Tahoe, Nevada, October 31 - November 2, 1973, AIAA Preprint 73-1051.
7. "Performance of 30-CM Ion Thrusters with Dished Accelerator Grids", Vincent K. Rawlin, Presented at the AIAA 10th Electric Propulsion Conference, Lake Tahoe, Nevada, October 31 - November 2, 1973, AIAA Preprint 73-1053.
8. "The Distribution of Neutral Atoms and Charge Exchange Ions Downstream of an Ion Thruster", J. F. Staggs, W. P. Gula, and W. R. Kerslake, NASA TM X-52259. Also, Journal of Spacecraft and Rockets 5, 159-164, February, 1968.
9. "Ion Thruster Propellant Utilization", Harold R. Kaufman, Journal of Spacecraft and Rockets, 7, 511-517, July, 1972.
10. "The Generation and Diagnosis of Synthesized Plasma Streams", J. M. Sellen, Jr., W. Bernstein, and R. F. Kemp, Review of Scientific Instruments, 36, 316-322 (1965).